# A Search for Generation-1 Leptoquarks in Proton-Antiproton Collisions at $\sqrt{s} = 1.8$ TeV at the Collider Detector at Fermilab

A Dissertation

Presented to

The Faculty of the Graduate School of Arts and Sciences

Brandeis University

Department of Physics

In Partial Fulfillment
of the Requirements for the Degree of
Doctor of Philosophy

by
Steven M. Moulding
February, 1993

This dissertation, directed and approved by the candidate's Committee, has been accepted and approved by the Graduate Faculty of Brandeis University in partial fulfillment of the requirements for the Degree of

DOCTOR OF PHILOSOPHY

Dean, Arts and Sciences

Dissertation Committee:

Craig A. Blocker

Craig Blocker, Chairman

Laurence F. Abbott

Laurence Abbott

Bruce M. Foxman

Bruce Foxman (Chemistry)

# ABSTRACT

## A Search for Generation-1 Leptoquarks in Proton-Antiproton Collisions at $\sqrt{s} = 1.8$ TeV at the Collider Detector at Fermilab

(A Dissertation Presented to the Faculty of the Graduate School of Arts and Sciences of Brandeis University, Waltham, Massachussetts)

by Steven M. Moulding

This thesis presents two complementary analyses describing a search for pair-produced generation-1 leptoquarks. In the $e^+e^-$+dijet channel our observations are consistent with expectations for background processes. Based on this we find $M_{LQ} > 113$ GeV at 95%CL assuming $BR(LQ \rightarrow e + u) = 100\%$. For $BR = 50\%$ we exclude $M_{LQ} < 82$ GeV. No limits can be set in this channel if $BR < 30\%$. Our 95% upper limit on the production cross section ranges from $\sigma \cdot BR^2 < 55$pb at $M_{LQ} = 45$ GeV to 4.0pb at $M_{LQ} = 125$ GeV. The $e^{\pm}\nu_e$+dijet channel is sensitive to smaller $BR(LQ \rightarrow e + u)$. The background is expected to be far more severe and is separated from the signal using a statistical relative likelihood method. We find no evidence for leptoquark production in this channel and exclude $BR > 9\%$ for $M_{LQ} = 45$GeV. The highest mass limit attainable is for $BR = 50\%$ when we find $M_{LQ} > 72$ GeV at the 95% CL.



# Acknowledgements

During the five years I spent as a graduate student I met, and was influenced by, for better or worse, many people.

The constant throughout this time, and to who my greatest love and thanks go, has been my wife Anna Lef. She has been forced to put up with many things, not the least of which was my three year absence while I worked at CDF. Boston is a long drive from Chicago ! She has endured with patience my madcap inclinations to rockclimb, ski, build and sleep in igloos, and work on particle physics. Now she can finally say she's married to a doctor. A year from now, I'll be able to say the same.

To Anna's parents Isaac and Nadia my thanks for your love and support to both of us. Also thanks to our special friends, Ellie Klebanov and Lev Ludin.

I'd like to thank all my climbing friends, especially those who shared a precarious ledge or cramped tent with me on some foolish venture. Particularly I'd like to thank Mark Taylor for taking me up some incredible climbs over the last few years in New Hampshire, New York, and Joshua Tree. My life will never be the same. Other climbing friends I'd like to acknowledge include Ben Lawson, Bob Mattingly, Pavel Cenkl, Mitch Cohen and Jon Segal, and Alan and Sharon Brunelle.

To the Physics Department at Brandeis, and in particular the High Energy group, I want to express my sincere thanks for admitting me to graduate school and for their financial support. I would like to thank my advisor Craig Blocker for taking me on as a student, giving me the freedom to work independently, and for reading and correcting the hundreds of draft pages of this thesis. This was, for me, the perfect advisor-student relationship.

The person who most influenced me as a young graduate student and to who I owe

untold thanks is Phil Kesten. Phil is a truly wonderful guy; I wish there more like him. He taught me, with infinite patience, all I know about the mind-boggling CDF software, tried (unsuccessfully) to teach me how to juggle, competed with me for the most money found on the floor in a semester, advised me on my wake-up call service, and together we raced through deserted dorms at the end of the school year looking for abandoned piles of pennies. Phil helped me start an investment club with Steve, Larry and Les, and screamed as loudly as I did as our money rode the roller-coaster. For this, and more, thanks!

The people I met at Fermilab, and who I would like to acknowledge, are as follows: Firstly I'd like to thank Peter Todd Hurst, Brian Winer, and Paul Derwent. As well as being great guys, they answered my endless questions about many aspects of CDF analyses. They were always the people to who I'd first turn when confused. I'd also like to thank the following people for their interest in my analysis: Melissa Franklin, Milciades Contreras, Mike Gold, Rob Harris, Alberto Etchegoyen, Teruki Kamon, Steve Kuhlmann, Rick Vidal, Naor Wainer and Jose Benlloch. Also thanks to Dan Amidei for inviting me to Ann Arbor to give a seminar. It was quite a day ! Special thanks go to my analysis 'godparents' Pekka Sinervo and Slawek Tkaczyk. Also thanks to the exotic-group conveners Jay Hauser and John Yoh. Finally to Jim Freeman for suggesting what turned out to be a fascinating thesis topic.

Of the friends I made, I'd like to thank Tom Baumann, John Cunningham, Colin Jessop, Lou Keeble, Jaco Konigsberg, Bob Mattingly and the rest of the Gas Calorimetry 'bad-dogs' for their company and solidarity during the test-beam. To my friend Jaco I owe special thanks for all I now know about calorimeters, for advice on life and physics, and for that glorious day of skiing the Black Diamonds in Aspen. Also thanks to anyone and everyone who played soccer during those warm summer evenings. Other people I can't forget are Vic (fool) Scarpine, Les (hosed) Nakae, Chris Boswell and Steve Vejcik. Thanks to Carol Anway-Wiese for donuts, lunches, and the best chocolate cheese cake anywhere. On matters culinary, it was Peter Hurst who first induced me to make a 'run for the border'.



Taco Bell became part of my CDF graduate-student life. Nor would I have survived without El Tacqueria in West Chicago, endless coffee in B0, and Frank's Finer Foods.

CDF would not be CDF without Steve and DeeDee Hahn. I can't imagine what it would be like if they left. I'd like to thank them, and their inimitable kids Kylie and Chad, for all for the times they invited me into their house for Passover Seder, Latkes during Hanukkah, and to dinner in general.

A special thanks also goes to Carol Picciolo at CDF and Joan Thorne at Brandeis for their unending secretarial help and assistance. Life would have been a lot more difficult without them.

I want to thank Dino Goulianos and the rest of the group at Rockefeller University in New York for their hospitality and kindness in giving me an office and terminal where I could write my thesis. This meant I could be with my wife in the evenings, instead of with a phone. I also want to thank them for their confidence in taking me on as a post-doc.

My final thanks go to my family back in England, particularly to my Mother and Father: June and Leslie Moulding. In getting this far I owe them everything. To my younger siblings Heather, Dawn, Miles, Kay, and Gemma, I miss you!

*This thesis is dedicated to my parents for bringing me into a wonderful world, and to my wife Anna who waited to share it with me.*

## Table of Contents

# List of Tables

# List of Figures

# Chapter 1

## The Standard Model: An Overview

This thesis describes a search for one of a new class of exotic particles called leptoquarks. In order to understand why we think leptoquarks might exist, it is first necessary to review our current understanding of elementary particle physics as described by the 'Standard Model' (SM). In doing so we can identify some of the shortcomings in our model and thereby motivate the introduction of new particles, such as leptoquarks, as a means of resolving these deficiencies.

The Standard Model of elementary particles and their interactions has been enormously successful in describing many features of physics in the sub-nuclear world. Of the four fundamental forces currently known, the Standard Model describes three of them (strong, weak, and electromagnetic) and leaves out only gravity. Our current picture of electromagnetism at the quantum level emerged in the 1940's and 1950's from the work of Feynman [1], Schwinger [2], Tomonaga [3], and others, and became known as the theory of Quantum Electrodynamics (QED). Seminal papers on the foundations and development of QED which, including the above references, have been collected by Schwinger and can be found in [4]. More recently two of the three forces have been successfully unified into a single 'electroweak' force (Section 1.3). The current theory of the strong interaction is known as Quantum Chromodynamics (QCD) and will be described in Section 1.4.

### 1.1 Gauge Symmetry: Cornerstone of the Standard Model

The starting point of the Standard Model is the description of the known elementary particles in terms of quantum fields, the dynamics of which are governed



by a Lagrangian field density $\mathcal{L}$. If we denote by $\psi$ the field for an elementary particle of mass $m$, then the free particle Lagrangian density can be written as

$$\mathcal{L}_{\text{FREE}} = \mathcal{L}(\psi, m)$$

The dynamics of the whole spectrum of known elementary particles $\psi_i$ ($i = 1, \ldots, N$) in the absence of any interactions, can then be described as a sum of such densities

$$\mathcal{L}_{\text{FREE}}(SM) = \sum_{i=1}^{N} \mathcal{L}(\psi_i, m_i)$$

It is through the requirement that this Lagrangian be invariant under various symmetry transformations that interactions between elementary particles arise. This 'gauge symmetry' principle when applied using SU(3), SU(2), and U(1) symmetry groups leads to the description of the strong, weak, and electromagnetic forces respectively. As such, local gauge invariance can be considered as *the* cornerstone on which the Standard Model is built.

As an example of the gauge symmetry principle, we briefly examine its application to the electromagnetic interaction, since of all the fundamental forces this one is the simplest to consider. Though the Standard Model contains several charged particles, we will consider, for simplicity, a model containing just one elementary fermion: the electron.

The electron is a spin-1/2 particle described by a field $\psi_e$ and having a mass $m_e$. The free Lagrangian density for the electron can be written as

$$\mathcal{L} = \overline{\psi}_e(i\partial\!\!\!/ - m_e)\psi_e$$

By requiring that the equations of motion derived from this Lagrangian be invariant under an arbitrary phase transformation of the electron field

$$\psi(x) \longrightarrow \psi'(x) = e^{-iq\theta}\psi(x)$$

we are led, via Noether's theorem, to a conserved current. This turns out to be precisely the electromagnetic current for an electron

$$j^\mu = q\overline{\psi}_e\gamma^\mu\psi_e$$

provided we identify q with the electromagnetic charge of the electron.

A much more powerful requirement is that of being able to make an arbitrary phase transformation at any space-time point we choose without affecting the electron dynamics:

$$\psi(x) \longrightarrow \psi'(x) = e^{-iq\theta(x)}\psi(x)$$

Invariance of $\mathcal{L}$ under this *local* U(1) phase transformation leads not only to the conserved electromagnetic current but also necessitates the introduction of a new vector field $A^\mu$. This new field must itself transform under the phase transformation to leave the Lagrangian invariant

$$A^\mu \longrightarrow A'^\mu = A^\mu + \partial^\mu\theta(x).$$

The locally invariant Lagrangian now has the form

$$\mathcal{L} = \mathcal{L}_{\text{FREE}} + \mathcal{L}_{\text{INT}} = \overline{\psi}_e(i\partial\!\!\!/ - m_e)\psi_e - j_\mu A^\mu$$

We find that local gauge invariance forces upon us the interaction of the electron with a massless vector field, and therefore gives us a model for the electron-photon interaction. By adding a free field term for the photon we finally arrive at the QED Lagrangian

$$\mathcal{L}_{\text{QED}} = \overline{\psi}_e(i\partial\!\!\!/ - m_e)\psi_e - j_\mu A^\mu - 1/4F_{\mu\nu}F^{\mu\nu}$$

where

$$F_{\mu\nu} = \partial_\mu A_\nu - \partial_\nu A_\mu$$

This Lagrangian is invariant under any local U(1) phase transformation we wish to make, and by application of the Euler-Lagrange equations yields Maxwell's equations.

Given this success it is natural to ask whether the same principles can be applied to yield descriptions of the weak and strong forces. The answer is yes, however the situation is more complex.

Although an effective theory of the weak interaction had been around since Fermi proposed his model for $\beta$-decay in 1934 [5], a full description based on local



gauge invariance came only after unification of the weak and electromagnetic forces, and the application of the Higgs mechanism in the 1960's. The unified electroweak interaction is based on the symmetry group $SU(2) \otimes U(1)$ and will be discussed further in Section 1.3.

In 1954, Yang & Mills proposed a gauge theory based on $SU(2)$ to be applied to two equal-mass spin-1/2 fields. This was intended to be a model for the proton-neutron system and would attempt to describe the strong force with its observed isospin invariance. However, since the triplet of massless vector bosons associated with the $SU(2)$ gauge symmetry are not observed in nature, the Yang-Mills theory could not be a viable model of the strong interaction.

More than a decade after its proposal the Yang-Mills model was successfully revived in the context of electroweak interactions. Later still, the same ideas were applied to the colored quark model and the resulting gauge theory based on the SU(3) symmetry group evolved into what we know today as Quantum Chromodynamics (QCD) (Section 1.4). Combining QCD and the electroweak force, we obtain a description of strong, weak, and electromagnetic interactions based on a Lagrangian invariant under local $SU(3) \otimes SU(2) \otimes U(1)$ transformations.

Having described the ideas of local gauge invariance and illustrated them using the electrodynamics of the electron, we now turn to the introduction of the other elementary particles. This will be followed by a short discussion of the main features of the electroweak and strong forces.

## 1.2 The Elementary Particles

Within the Standard Model, elementary particles are divided into the quarks and leptons (elementary constituents of matter), and the gauge bosons which mediate their strong, weak, and electromagnetic interactions. As described earlier, the starting point of the Standard Model is to write down a Lagrangian containing the free particle fields for the quarks and leptons. We can add as many free field terms to this Lagrangian as there are elementary particles to be included of the model. In other words the Standard Model neither predicts, nor constrains, the

number of quarks and leptons, and to date there are six of each. Both quarks and leptons are grouped into three families of two particles each, as shown in the following table:

| | Leptons | Mass | Charge | Quarks | Mass | Charge |
|---|---|---|---|---|---|---|
| Generation 1 | e | 0.511 MeV | -1 | up | $\sim$ 350 MeV | +2/3 |
| | $\nu_e$ | $<$ 17 eV | 0 | down | $\sim$ 350 MeV | -1/3 |
| Generation 2 | $\mu$ | 106 MeV | -1 | charm | 1.5 GeV | +2/3 |
| | $\nu_\mu$ | $<$ 0.27 keV | 0 | strange | $\sim$ 500 MeV | -1/3 |
| Generation 3 | $\tau$ | 1.784 GeV | -1 | top | $>$ 91 GeV | +2/3 |
| | $\nu_\tau$ | $<$ 35MeV | 0 | bottom | 4.7 GeV | -1/3 |

Table 1.1: Elementary Fermions in the Standard Model.

The top quark has yet to be discovered, though there are good reasons for believing in its existence. At present we know that in the simplest form of the Standard Model the top mass must be greater than 91 GeV at 95% CL [6]. Should its mass be less than 150 GeV or so, it is likely that it will be discovered in the data taken during the current (1992-93) collider run at Fermilab.

There is also no direct evidence at the present time for the existence of the tau-neutrino, $\nu_\tau$, though upper limits on its mass have been set at $m_{\nu_\tau} < 35$ MeV based on an analysis of the decay $\tau^- \longrightarrow 2\pi^+ 3\pi^- \nu_\tau$ [7, 8].

Discovery of both the top quark and the $\tau$-neutrino would complete the spectrum of elementary fermions within the Standard Model. We note, however, that the theory does *not* predict the number of elementary particle families, and we therefore leave open the possibility of adding fourth and even higher generations as needed, or until we obtain such a prediction.

All of the quarks and leptons are spin-1/2 fermions and except for (possibly) the neutrinos, all are massive. The Standard Model does not predict the mass spectrum of the quarks and leptons. Fermion masses arise from initially massless fields via the Higgs mechanism (Section 1.3) though in an ad hoc way.

The gauge bosons are the spin-1 mediators of forces between the quarks, and also between the leptons. Their name is derived from the fact that they come into existence via the imposition of gauge symmetries on the fermion free particle



Lagrangian, as discussed in the previous section.

The strong force, based on SU(3), has 8 massless mediators called gluons which couple to colored particles including quarks but *not* leptons. In $SU(2) \otimes U(1)$ electroweak theory, there are 3 massive mediators $W^\pm, Z^0$ which couple to all of the elementary fermions, and the massless photon which couples to charged quarks and leptons. We summarize the main properties of the 12 gauge bosons in the following table

| Gauge Boson | Spin | EM Charge | Mass (GeV) | Force |
|---|---|---|---|---|
| Gluons (8) | 1 | 0 | 0 | Strong |
| Photon | 1 | 0 | 0 | EM |
| $W^\pm$ | 1 | $\pm$1 | 79.91 | Electroweak |
| $Z^0$ | 1 | 0 | 91.15 | Electroweak |

Table 1.2: Gauge Bosons in the Standard Model.

## 1.3 Electroweak Interactions

We now give a brief description of the main features of the electroweak interaction within the Standard Model, and an outline of its historical development.

In 1934 Fermi proposed a model for the nuclear $\beta$-decay $n \rightarrow p + e^- + \overline{\nu}_e$ based on a four-fermion interaction of the nucleons and leptons [5] and illustrated in Figure 1.1. In analogy with the electromagnetic current $j^\mu = q\overline{\psi}_e \gamma^\mu \psi_e$, Fermi proposed weak vector currents for the nucleons and leptons

$$N_\mu = \overline{\psi}_p \gamma_\mu \psi_n \text{ and } L_\mu = \overline{\psi}_e \gamma_\mu \psi_\nu$$

thus making his model a $V \times V$ contact interaction (by $V$ we mean a vector current). The corresponding weak interaction Lagrangian is then

$$\mathcal{L}_{WEAK} = -G_F(\overline{\psi}_p \gamma_\mu \psi_n)(\overline{\psi}_e \gamma^\mu \psi_\nu) \equiv -G_F N_\mu L^\mu$$

where $G_F$ is the Fermi coupling constant. This model proved very successful in describing $\beta$-decay and other 'low-energy' weak interactions. However, some modifications were needed.

In 1956 Lee & Yang had, as a way of solving the famous $\tau - \theta$ problem, proposed that weak interactions violate parity conservation. This was achieved in the Fermi model by considering weak currents to be not just simple vectors, but rather some mixture of vector- and axial-vector currents [10]. Experiments favored a $(V-A)\times(V-A)$ form for the current-current interaction, described by the parity violating Lagrangian

$$\mathcal{L}_{\text{WEAK}} = -G_F(\overline{\psi}_p\gamma_\mu(1-\gamma_5)\psi_n)(\overline{\psi}_e\gamma^\mu(1-\gamma_5)\psi_\nu).$$

In 1957 direct experimental confirmation of parity non-conservation in weak interactions was obtained [11].

The observed parity violation effects lead to the realization that only left-handed fermion doublets participate in weak interactions, right-handed fermions being weak-$SU(2)$ singlets. Thus the electron and neutrino appear in the model as

$$L \equiv (e_L, \nu_L)$$

where $e_L = (1-\gamma_5)\psi_e$ and $\nu_L = (1-\gamma_5)\psi_\nu$. To remind us of this left-handedness, the symmetry group of weak interactions is labeled $SU(2)_L$.

The second modification of Fermi's theory came with the realization that the contact interaction is really only an effective low energy approximation. The weak V-A currents interact via the exchange of massive vector gauge bosons. The first to propose such a model was Klein [12] who in 1938 suggested that the weak current-current interaction was mediated by charged gauge bosons $W^+, W^-$ analogous to the photon in electromagnetism. Noting the similarity between the weak and electromagnetic mediators, Schwinger put forward a theory in 1957 [13] in which the $W^+, W^-$, and photon appeared as a triplet of gauge fields, thus attempting electroweak unification. This program was completed by Glashow (1961) [14], Weinberg (1967) [15], and Salam (1968) [16], among others.

The Glashow model is based on an $SU(2)_L \otimes U(1)$ gauge symmetry and introduced a new neutral weak gauge boson to mediate neutral current interactions. Weak neutral currents were required experimentally to account for the $\Delta I = 1/2$ non-leptonic decays of strange particles. However, Glashow had no explanation



for why the weak gauge bosons were so heavy, and the large masses required had to be inserted into the model by hand. In 1964, Higgs introduced the idea of the spontaneous symmetry breaking [9]. When applied to the electroweak Lagrangian by Weinberg in 1967, and independently by Salam in 1968, the gauge bosons acquired mass. Moreover, the masses of the $W^\pm$ and $Z^0$ were *predictable* in terms of measurable quantities:

$$M_W^2 = \pi\alpha/\sqrt{2}G_F \sin^2\theta_W$$

and

$$M_Z^2 = M_W^2/\cos^2\theta_W.$$

Here $\alpha$ is the EM coupling constant, and $G_F$ the Fermi coupling. With the weak mixing angle measured to be $\theta_W \simeq 0.22$, this gives the predictions $M_W \simeq 79.5$ GeV and $M_Z \simeq 90.0$ GeV. These predictions were spectacularly confirmed in 1983 with the discovery of both W and Z at CERN [17, 18]. However, the method of endowing the weak bosons with mass comes at the expense of introducing a neutral scalar field $\phi^0$, known as the Higgs field. The corresponding Higgs particle is itself massive, though the model has no prediction for its mass; certain arguments suggest that $M_H <\sim 1$ TeV. To date there is no evidence for the Higgs, and its discovery remains today one of the most sought after goals in particle physics. Recent results from LEP place the limit $M_{H^0} > 52GeV$ at 95% CL [19]. Non-minimal Standard Models contain charged Higgs particles. Other theories beyond the Standard Model do away with the Higgs particle completely. In our discussion of physics beyond the Standard Model in Chapter 2, we briefly mention alternative methods of symmetry breaking without the need for the introduction of the Higgs scalar.

Returning to Fermi's contact interaction, we know today that nucleons are actually composite objects, containing quarks and gluons. The spin-1/2 quarks participate in electroweak interactions. This leads to our current picture of $\beta$-decay (Figure 1.2), to which Fermi's current-current interaction (Figure 1.1) is clearly just an effective approximation.

The couplings of the electroweak bosons to fermions (both quarks and leptons) have been studied extensively. In proton-antiproton collisions, both W's and Z's can be produced by quark-antiquark annihilation, and we will see later that W,Z decay can sometimes fake our leptoquark signal. At the LEP $e^+e^-$ collider, operating at $\sqrt{s} = M_Z$, millions of $Z^0$ events have been observed allowing precision tests of part of the electroweak sector in the Standard Model. To leading order, W's cannot be produced singly at current $e^+e^-$ energies, though LEP plans to operate at $\sqrt{s} = 2M_W$ in the future. The best studies of the W currently come from CDF where, amongst other W-quantities, the mass has been measured and found to be $M_W = 79.91 \pm 0.39$ GeV [20]. The untested parts of electroweak model include interactions involving more than one gauge boson at the same vertex, and the entire Higgs sector. Although the photon has no self coupling, the weak gauge bosons do. The non-abelian nature of the weak-interaction symmetry group SU(2) leads to mediators which themselves carry a conserved weak-charge and so have self couplings. We might therefore expect vertices such as $Z^0W^+W^-$, $\gamma W^+W^-$, $W^+W^-W^+W^-$, etc. Such interactions have not been seen to date, though again LEP will be able to study the $\gamma W^+W^-$ vertex once they attain $\sqrt{s} \geq 2M_W$.

We summarize this section on electroweak interactions by saying that the model appears to be in very good shape in terms of describing observed phenomena. No observation is yet in disagreement with the electroweak Standard Model. Certain areas remain untested, in particular the multi-linear gauge boson couplings and the discovery of the Higgs boson. We can only look to the future to address these areas, or in the absence of the Higgs, to an alternate mechanism for electroweak symmetry breaking.

### 1.4 QCD

Quantum Chromodynamics is the current candidate for a gauge theory of the strong interaction and, as its name implies, QCD deals with interactions between colored particles. The color quantum number arose as a way of dealing with



several serious deficiencies in the simple quark model. Firstly the existence of the $\Omega^-$ baryon seemed to violate the Pauli exclusion principle if made up of 3 spin-1/2 objects; its wavefunction was completely symmetric under quark interchange. The addition of an extra quantum number (color), with three possible values, to each quark removes both their indistinguishability and the associated violation of the exclusion principle. Another motivation for color was the experimental lack of observation of free quarks. By introducing color and the axiom that all particle states appear as color singlets, this problem too is removed. Finally, observed rates of $e^+e^- \rightarrow$hadrons are a factor of 3 higher than the naive parton model suggests. By summing over 3 quark colors in our calculations we obtain good agreement between theory and experiment.

The starting point for QCD, then, is a Lagrangian in which each flavor of quark appears as a fundamental color triplet $Q \equiv (q_r, q_g, q_b)$, and on which we impose an SU(3) symmetry. The symmetry is exact since, for a given quark flavor, the three color states are mass-degenerate and are in every other way indistinguishable.

Although based on the larger SU(3) symmetry group, nevertheless QCD is somewhat simpler to formulate than SU(2)⊗U(1) electroweak gauge theory since for QCD there is no spontaneous symmetry breaking mechanism involved. However, simplicity of formulation does not always imply simplicity of extracting meaningful predictions. As we shall see in this section, the QCD coupling constant $\alpha_s$ is small at high energy scales. At lower energies $\alpha_s$ becomes large, making it extremely difficult in many instances to apply the usual perturbative methods when studying the strong interaction. For example, QCD predictions for the masses of bound states of light quarks, such as the $\pi$-meson, have so far proved impossible to obtain by analytic techniques. In this non-perturbative regime we are forced to rely on other approaches such as lattice gauge theory, and usually on intensive computer simulation. At higher energy scales, the story is much better. At current $\bar{p}p$-collider energies, $\alpha_s$ becomes small enough that perturbative estimates of many quantities can be made. Leading order QCD predictions for two-jet production rates and angular distributions, for example, have been shown to be in good agreement with experimental data [21, 22].

As we mentioned in Section 1.1, QCD is an example of a Yang-Mills theory where we apply local gauge invariance to a non-abelian symmetry group, in this case color-SU(3). There are eight gauge fields (gluons) associated with the eight generators of color-SU(3) and in the absence of any spontaneous symmetry breaking these fields remain massless. The form of the QCD Lagrangian is then as follows

$$\mathcal{L}_{\rm QCD} = \overline{Q}(i\partial\!\!\!/ - m_q)Q + \overline{Q}(g_c\gamma_\mu A^\mu)Q - \frac{1}{2}{\rm Tr}G_{\mu\nu}G^{\mu\nu}$$

where $g_c$ is the color field coupling strength, $A_\mu$ has an implicit sum over the eight gauge fields weighted by the SU(3) generators $\lambda^i$

$$A_\mu = \sum_{i=1}^{8} \lambda^i A^i_\mu,$$

and

$$G_{\mu\nu} = \partial_\mu A_\nu - \partial_\nu A_\mu - ig_c\left[A_\mu, A_\nu\right]$$

Since SU(3) is non-abelian the gluons themselves carry color. This means that self couplings arise between the gluons, similar to the $W - Z - \gamma$ vertices we encountered in electroweak SU(2)⊗U(1). These self interactions must be taken into account when calculating higher-order corrections to QCD processes. These corrections will modify the Born level matrix element:

$$\mathcal{M}_0 \longrightarrow \mathcal{M}_1 = \mathcal{M}_0\left[1 + a_1\epsilon\right]$$

where we assume $\epsilon$ is small. By adding in factors from all higher-order processes we obtain a (hopefully) convergent expression for corrected matrix element

$$\mathcal{M} = \mathcal{M}_0\left[1 + a_1\epsilon + a_2\epsilon^2 + \cdots\right]$$

and from this we can define an effective coupling constant $\alpha_s$ for the process.

The leading order s-channel contribution to the $q\overline{q} \rightarrow q\overline{q}$ rate, for example, is shown in Figure 1.4. The leading order corrections to this process involve modifications of the qqg vertex and of the gluon propagator. The vertex corrections and the fermion-loop corrections to the gluon propagator are shown in Figure 1.4, along with their QED analogs. However the self-coupling between gluons means



that we also have to include contributions from gluon loops in the propagator (Figure 1.4), a process with no QED counterpart. This extra contribution is sufficient to drastically alter the form $\alpha_s$ from the case in which there are no gauge field self interactions (QED). In QED higher-order corrections lead to charge screening effects and an effective coupling which decreases at large distances (small energy scales), and diverges at small distances (large energies):

$$\alpha(q^2) = \frac{\alpha(\mu^2)}{1 - \alpha(\mu^2)\frac{1}{3\pi}\log\left(\frac{q^2}{\mu^2}\right)}.$$

In QCD, however, the gluon self coupling leads to anti-screening, with a running $\alpha_s$ that decreases at high energy and increases lower energies. Summed to all orders, $\alpha_s$ has the form

$$\alpha_s(q^2) = \frac{\alpha_s(\mu^2)}{1 + \alpha_s(\mu^2)\frac{b_0}{4\pi}\log\left(\frac{q^2}{\mu^2}\right)},$$

where $q$ is the momentum transfer involved in the process and $\mu$ is a reference energy scale at which point we have *measured* the value of $\alpha_s$ and from which we can extrapolate to other scales. The constant $b_0$ is given by $3b_0 = 11N_C - 2N_F$, where $N_C$ is the number of colors in QCD (usually 3), and $N_F$ is the number of quark flavors. Since $b_0 > 0$ (otherwise QCD would look like QED) we expect at most 16 flavors (or 8 doublets) in a theory with $N_C = 3$.

The asymptotic behaviour of the strong coupling is born out experimentally. No free colored particles have ever been observed. The increasing strength of the strong force with distance between colored particles tends to bind them very strongly, a phenomenon known as 'confinement'. At the other end of the distance/energy scale, measurements of the deep inelastic scattering of high energy photons off protons in electron-proton collisions can be explained by assuming the proton to be composed of point like fermions (quarks). Furthermore the constituent quarks behave as if they are essentially free during their interaction with the photon, and yet are still strongly confined within the proton. This 'asymptotic freedom' is explained by the running of the QCD coupling $\alpha_s$, as is confinement, and both of these predicted properties led to the acceptance of QCD as the gauge theory of the strong interaction.

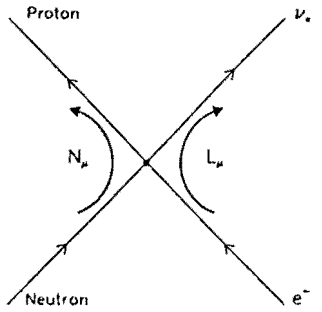


Figure 1.1: The Fermi Current-Current Interaction as a Model of Neutron Decay.

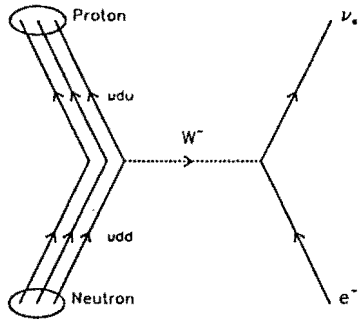


Figure 1.2: Weak Decay Of The Neutron As Described By The Standard Model.



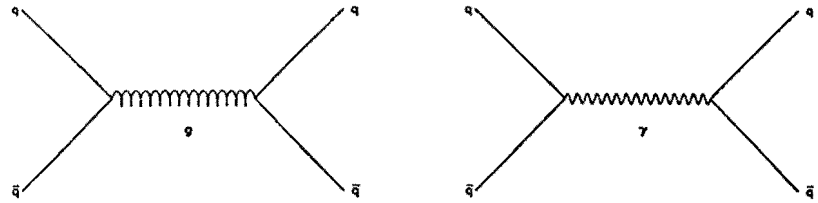


Figure 1.3: Leading Order Processes Contributing to $q\bar{q} \rightarrow q\bar{q}$ In QCD And QED.

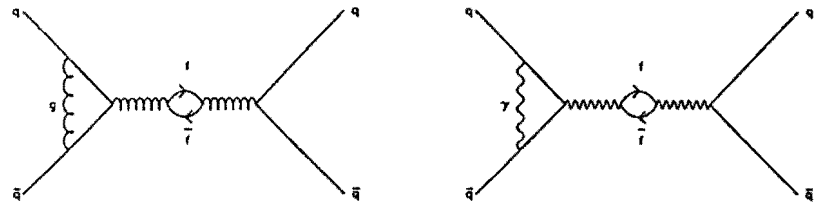


Figure 1.4: Fermion Loop And Vertex Corrections to $q\bar{q} \rightarrow q\bar{q}$ In QCD And QED.

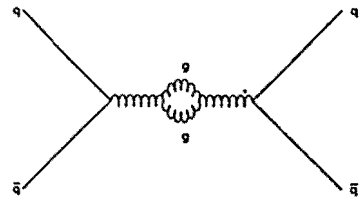


Figure 1.5: Gauge Boson Loop Corrections to $q\bar{q} \rightarrow q\bar{q}$ In QCD.

# Chapter 2

# Leptoquarks: A Theoretical Motivation And Current Limits

*"...they are ill discoverers that think there is no land when they can see nothing but sea."* Francis Bacon

## 2.1 Extensions to the Standard Model and the Appearance of Leptoquarks

While so far no effect has been observed which contradicts the model and though many of its predictions have been confirmed, nevertheless the Standard Model appears to be somewhat arbitrary in both the number of free parameters and in the patterns found within it. We might, therefore, view the Standard Model as a fundamentally correct yet incomplete description of particle physics, and by looking beyond it we can address many unanswered questions.

A search for leptoquarks is particularly attractive because they appear to be a generic feature of many attempts to go beyond the Standard Model. While properties such as their electric-charge and couplings to known particles can vary between competing models, all leptoquarks share the common feature of being massive bosons carrying both color and lepton quantum numbers.

Rather than give a general overview of new physics possibilities, we will consider several Standard Model extensions individually and focus specifically on where leptoquarks appear. Theories based on $SU(5)$ and $E_6$ symmetry seek to embed the Standard Model in a higher gauge group and therefore attempt to unify forces. Other models such as technicolor and nearby-compositeness theories give substructure to the quarks and leptons. Finally, superstring theories start from the 'top-down' and try to derive the Standard Model from a theory with just two



fundamental parameters. All of these theories have been the subject of intense theoretical and experimental activity over the past decade, and in all of them we find leptoquarks in one form or another.

### 2.1.1 $SU(5)$

The Standard Model has the group structure $SU(3) \otimes SU(2)_L \otimes U(1)$. Grand Unification schemes attempt to do what electroweak unification did for the electromagnetic and weak forces, namely the description of strong, weak and electromagnetic interactions as different manifestations of a single underlying force. The gauge symmetry group $\mathcal{G}$ for this force should be large enough to contain the Standard Model i.e. $\mathcal{G} \supset SU(3) \otimes SU(2)_L \otimes U(1)$. A Higgs type mechanism would then spontaneously break the underlying symmetry at some very large energy scale $V_{GUT} >> V_{EWK} \sim 250$ GeV. The new energy scale must be very large since the symmetry breaking of $\mathcal{G}$ leads to new massive gauge bosons whose effects must be very much smaller than those of the $W^{\pm}$ and $Z^0$, or they would have been apparent already. These effects include proton decay, and current limits on the proton lifetime require that $V_{GUT} \sim 10^{16}$ GeV in the simplest models.

The smallest acceptable group for $\mathcal{G}$ is $SU(5)$. Based on this, Georgi and Glashow [23] proposed a grand unified model in 1974, the consequences of which can be found in several detailed reviews; see for example [24, 25].

As a gauge symmetry group, SU(5) has several very attractive features. Firstly, such a choice leads naturally to charge quantization. This follows since the eigenvalues of the generators of a simple non-abelian group such as $SU(5)$ are discrete. Electric charge Q is a generator of $SU(5)$ and hence is quantized. Furthermore, $SU(5)$ predicts that

$$Q_d = 1/3 Q_e$$

i.e. not only is charge quantized, but the relation between electron and quark charges is explained. These are very significant predictions.

Secondly, $SU(5)$ accommodates the known quarks and leptons very economically. The $\bar{5}$ and 10 representations of $SU(5)$ have the following $SU(3) \otimes SU(2)$

content:

$$\overline{5} = (\overline{3},1) \oplus (1,\overline{2})$$

$$10 = (\overline{3},1) \oplus (3,2) \oplus (1,1)$$

We then have

$$\overline{5} \oplus 10 \supseteq \overline{d}_L + (e^-, \nu_e) + \overline{u}_L + (u_L, d_L) + \overline{e}_L$$

i.e. we can completely contain one generation of quarks and leptons without having to introduce new fermions to fill the representation. Again, this is a remarkable result which is not trivial. For example, Georgi points out [26] that for another choice of color group such as $SU(N)$ we can recover the above quark and lepton representations *provided* $N$ is odd, *but* at the expense of many new fermions if $N \neq 3$. The economy of SU(5) in containing the quarks and leptons is therefore very encouraging.

Thirdly SU(5) predicts a single coupling strength above the unification scale $V_{GUT}$. The convergence of the running couplings of the strong, weak, and electromagnetic forces has now been tested and remarkably all three do indeed appear to converge at approximately $10^{15}$ GeV. This is roughly the same scale as is derived from limits on proton decay.

One final reason that might make us believe in $SU(5)$ is the freedom of the corresponding theory from anomalies. Anomalies arise in field theories containing fermions and are essentially terms in perturbative expansions which arise from fermion loops. Their presence ruins attempts to renormalize the theory, and so any successful renormalizable theory has to be anomaly free. Again, $SU(5)$ passes the test.

Having described the attractive features of $SU(5)$ in terms of describing the Standard Model, we now ask what new predictions it gives. We have shown how the fermions fit compactly into SU(5) representations. What about the gauge bosons? These are contained within the 24 representation of $SU(5)$ which has the $SU(3) \otimes SU(2)$ decomposition

$$24 = (8,1) \oplus (1,3) \oplus (1,1) \oplus (3,2) \oplus (\overline{3},2)$$



The first three terms describe the 8 gluons and 4 electroweak gauge bosons. We are left with 12 vector fields that carry non-trivial $SU(3)$ *and* $SU(2)$ indices. These particles have both diquark and leptoquark couplings, and in the latter case can mediate transitions between leptons and quarks. In $SU(5)$ the new vector-bosons are labelled $X$ and $Y$ and their charges are predicted to be

$$Q_X = -4/3 \qquad\qquad Q_Y = -1/3$$

The $X, Y$ of minimal SU(5) can, amongst other things, mediate proton and neutron decay (Figure 2.5). In order to be compatible with current limits on the proton lifetime ($\tau_P > 5.5 \times 10^{32}$ years [27]), their masses are required to be extremely large, of order $2 \times 10^{16}$ GeV. From the point of view of a search for leptoquarks at hadron colliders this is unfortunate since the $X$ and $Y$, with their leptoquark couplings, are then kinematically inaccessible by many orders of magnitude.

However, as nice as minimal SU(5) appears to be, it too has some fundamental problems. These include a lack of insight into the generational structure of the fermions, no predictions for the fermion masses and mixing angles, and the puzzling existence of two mass scales separated by around 13 orders of magnitude.

Some of these problems can be solved by extending SU(5) to a larger gauge symmetry group $\mathcal{G}' \supset SU(5)$. We also find that it is then often possible to find mechanisms which suppress proton decay, thereby allowing relatively light $X, Y$ bosons, an important point for a leptoquark search. To see how this can arise we firstly note that minimal SU(5) conserves $B - L$, but not both separately. If we could find, in an extended SU(5), a symmetry that requires separate lepton and baryon number conservation at vertices involving the $X, Y$ bosons, then we automatically suppress nucleon decay. Such a model is presented in [28], where the $X, Y$ appear as true leptoquarks, having *only* lepton-quark couplings.

Having seen that such models exist, we therefore leave open the possibility of observing light vector leptoquark bosons from an extended SU(5), these having charge $-1/3$ or $-4/3$, and which conserve $B$ and $L$.

### 2.1.2 Technicolor

Technicolor models address problems in a different area of the Standard Model, those of the Higgs sector. As discussed earlier, the Higgs mechanism is responsible for breaking the $SU(2)_L \otimes U(1)$ electroweak symmetry but at the expense of introducing a new neutral scalar field $\phi^0$. As it breaks electroweak symmetry the Higgs mechanism gives masses to the $W^\pm$ and $Z^0$ bosons. The mechanism also predicts that $M_W = M_Z \cos\theta_W$, which is experimentally confirmed. On the other hand, masses for the elementary fermions have to be introduced arbitrarily through their Yukawa couplings with the Higgs field. Unfortunately, the Standard Model has no prediction for the coupling Yukawa strengths, and so models with Higgs scalars are left with many free parameters which have to be added by hand. There are also no predictions for the mass of the Higgs boson itself, and its charge is not constrained, though in the minimal Standard Model a neutral Higgs is assumed.

Technicolor and similar models invoke 'dynamical symmetry breaking' to break electroweak symmetry and give masses to the corresponding gauge bosons. This avoids the need for the introduction of an elementary Higgs scalar and all the accompanying arbitrary couplings. Of significance is the fact that these models can reproduce $M_W = M_Z \cos\theta_W$. A review of technicolor and experimental signatures can be found in Reference [30].

In technicolor the Higgs boson and other fundamental particles appear as bound states of even more elementary particles called 'technifermions'. These are bound together by a new technicolor interaction with scale $\Lambda_{TC} \sim 1$ TeV. As a choice for the gauge symmetry group, $\mathcal{G}_{TC} = SU(3)_{TC}$ is often used. The technifermions are usually given the same $SU(2)_L \otimes U(1)$ quantum numbers as ordinary fermions and are then subdivided into techniquarks and technileptons.

In the simplest technicolor models there are no mechanisms for giving mass to Standard Model fermions. By embedding $\mathcal{G}_{TC}$ in an extended group $\mathcal{G}_{ETC} \supset \mathcal{G}_{TC}$ we can generate mass terms by exchange of an extended technicolor (ETC) gauge boson. These new bosons are associated with the breakdown of $\mathcal{G}_{ETC} \to \mathcal{G}_{TC}$ which



occurs at a scale 30 – 300 TeV and so must be extremely massive.

It is in extended technicolor models that leptoquarks appear. As an example we consider the Fahri-Susskind model [32] which contains a pair of color-triplet techniquarks $(U, D)$ and a pair of color-singlet technileptons $(N, E)$. Above $\Lambda_{TC}$ the technicolor Lagrangian obeys a chiral symmetry, that is $\mathcal{G}_{TC} \supset SU(n_f)_L \otimes SU(n_f)_R$ where $n_f$ is the number of techniflavors (8 in the Fahri-Susskind model). The breakdown of the chiral symmetry at $\Lambda_{TC}$ leads to the appearance of many Goldstone bosons, to which are given the generic name 'technipions'. The technipions of ETC can appear as color-singlets, color-triplets, and even color-octets. The color triplet $P_3$'s are isospin-triplets with electric charge $2Y+1, 2Y, 2Y-1$. The usual assignment is $Y = 1/3$, and so they couple to lepton-quark and quark-quark pairs. Their decays to lepton+quark pairs therefore qualify them as leptoquarks.

Interestingly, we can make some quantitative statements about these particular leptoquarks. Firstly, their masses are predicted to be

$$M(P_3) \simeq 160 \text{ GeV} \left(\frac{4}{N}\frac{n_f}{8}\right)^{1/2}$$

where N is the number of technicolors in $SU(N)_{TC}$. For $n_f = 8$ and $N = 3$ we have $M(P_3) \simeq 160$ GeV.

Secondly, since their couplings are proportional to fermion mass, we would expect the dominant decay channels of the leptoquarks to be

$$P_3 \to t\tau^+, t\overline{\nu}_\tau, b\tau^+, \overline{t}\overline{b}, \text{ etc.},$$

depending on the particular electric charge assignment and assuming channels are kinematically accessible.

Further details on technicolor leptoquarks, including production cross-sections and prospects for detection in $\overline{p}p$ collisions can again be found in Reference [30].

### 2.1.3 Compositeness

Leptoquarks also arise naturally in models of quark and lepton sub-structure. In these theories new elementary constituents called 'preons' are proposed. One

type of preon carries lepton number, while the other carries baryon number and color. Possible preon bound states are then leptons, quarks, and leptoquarks.

The composite-model leptoquarks appear as color-triplet composite objects in the form of pseudo-Goldstone bosons, much like the leptoquarks found in ETC. Both scalar and vector leptoquarks are expected and they carry charge 2/3. In the simplest models, there is only a single leptoquark $\chi$ which couples to all lepton-quark pairs with coupling strength $\lambda \sim m_q + m_l$. In the so-called 'nearby-compositeness' models there are generational selectional rules determined by different generations of preons. These rules carry over to the leptoquarks and we then require three generations of leptoquark

$$\chi_1 \rightarrow u\nu_e, de^+$$

$$\chi_2 \rightarrow c\nu_\mu, s\mu^+$$

$$\chi_3 \rightarrow t\nu_\tau, b\tau^+$$

One of the early models in which composite leptoquarks appear is the so-called strongly-coupled Standard Model proposed by Abbott & Fahri in 1981 [33]. A review of this, along with other composite and technicolor models as sources of leptoquarks, can be found in [34].

#### 2.1.4 Superstrings and $E_6$

We finally mention superstrings as a source of leptoquarks. Strings start with few parameters (usually two) and a very large gauge group which will contain all known particles, gravity, the Standard Model, and much more. Finding particular favor recently has been a description of interacting strings based on the $E_8 \otimes E_8$ symmetry group [35], which at low energies is expected to give an $E_6$ grand-unified model. $E_6$ contains the popular $SU(5)$ as a subgroup along with all of its accompanying nice features as described above. $E_6$ predicts the existence of scalar leptoquarks which are fractionally charged and which can have reasonably low masses. As in the case of nearby-compositeness, $E_6$ models naturally incorporate one leptoquark per fermion-generation and therefore have generation dependent



masses and couplings. Separate baryon and lepton number conservation is easily accommodated, thereby avoiding rapid nucleon decay.

The spectrum of particles arising in $E_6$ models is reviewed extensively by Hewett and Rizzo in [36].

$E_6$ leptoquarks appear to be very attractive. They have well defined experimental signatures, don't violate current limits on nucleon decay, and can have masses which are accessible at current colliders. Furthermore, their family structure allows for intra-generational transitions between quarks and leptons and naturally explains why quarks and leptons appear in equal numbers. Such a 'horizontal' quark-lepton symmetry has long been suspected particularly when we consider the collusion of quarks and leptons in cancelling anomalies. However it remains unexplained by the Standard Model. It is for these reasons that the properties of $E_6$ leptoquarks have usually been assumed in current literature by both theorists and experimentalists in their search for leptoquarks, and we will do the same. These properties will be summarized in the following section.

### 2.2 Leptoquark Properties: A Summary

In this thesis we will describe a search for leptoquarks of the $E_6$ type. We assume that the leptoquarks come in three families, and have generation-diagonal couplings. Baryon and lepton number is conserved at all leptoquark vertices. The leptoquarks are assigned baryon and lepton numbers $B = 1/3$ and $L = 1$. The leptoquarks are assumed to be color-triplet scalars and carry fractional electromagnetic charge. For this thesis it is irrelevant whether $|Q_{LQ}| = 1/3$ or $2/3$. We will assume $Q_{LQ} = -1/3$.

Recent literature gives as possible names for the leptoquarks $\chi_i$, $D_0$, and $S_i$, as well as $P_3$ for the color-triplet technipion. We find $\chi$ and $D_0$ to be confusing with the names of other standard particles and S (Scalar) to be too general. We therefore assign leptoquarks the name $LQ$ and attach a generation subscript unless otherwise clear. The following discussion involves $LQ_1$ particles, but the same ideas apply equally to the higher generation leptoquarks $LQ_2$ and $LQ_3$.

We assume that generation-1 leptoquarks having charge $Q = -1/3$ couple to the corresponding generation of quarks and leptons via the following interaction Lagrangian

$$\mathcal{L} = \lambda_L(LQ)^c_\alpha \left(\overline{u^\alpha_R} e^-_L - \overline{d}_R \nu_{eL}\right) + \lambda_R(LQ)_\alpha \left(\overline{u}^\alpha_R e^c_L\right) \quad + h.c. \tag{2.1}$$

where the $\lambda_{L,R}$ are referred to as the left- and right-handed couplings of the generation-1 leptoquark $LQ_1$ (we drop the generation index on the couplings though its presence should be regarded as implicit). Here $\alpha$ is an SU(3) color index, and $e^c_L$, for example, is understood to mean $(e^c)_L$.

The decay widths in the left and right handed channels are then

$$\Gamma_L = \frac{2 \times 3 \times \lambda_L^2 M_{LQ}}{16\pi} \qquad \Gamma_R = \frac{3 \times \lambda_R^2 M_{LQ}}{16\pi} \tag{2.2}$$

From these we can obtain the fraction of times that the leptoquark decays in the charged lepton mode ($x$), and the corresponding fraction of neutral lepton events, $1 - x$.

$$x = \frac{\Gamma_{e^- u}}{\Gamma_L + \Gamma_R} = \frac{\lambda_L^2 + \lambda_R^2}{2\lambda_L^2 + \lambda_R^2} \tag{2.3}$$

and

$$1 - x = \frac{\Gamma_{\nu_e d}}{\Gamma_L + \Gamma_R} = \frac{\lambda_L^2}{2\lambda_L^2 + \lambda_R^2} \tag{2.4}$$

Note: leptoquarks can decay in the neutral-lepton mode *only* if $\lambda_L \neq 0$.

In recent papers authors make various choices for $\lambda_L$ and $\lambda_R$. With the choice $\lambda_L$ =fixed and $\lambda_R = 0$ we expect $LQ \to u + e^-$ and $LQ \to d + \nu_e$ to appear in the final state an equal number of times on average. i.e. $x = 1/2$. Alternatively, for $\lambda_L = \lambda_R$ we would expect $x = 2/3$ and $1 - x = 1/3$.

In this thesis we leave the ratio of couplings, and hence x, as a free parameter. However we note that for *any* choice of $\lambda_L$ or $\lambda_R$, we always have the condition

$$\frac{x}{1-x} = \frac{\lambda_L^2 + \lambda_R^2}{\lambda_L^2} \geq 1 \tag{2.5}$$

This immediately implies that $x \geq 1/2$ and we *always* expect the same number or more charged lepton events than we do neutral lepton events. We should keep this in mind, though in this thesis we will aim to be more general and consider all possibilities,that is $0 < x < 1$.



## 2.3 Leptoquark Production Mechanisms and Event Signatures at High Energy Colliders

### 2.3.1 Leptoquarks at $\bar{p}p$ Colliders

Pair Production

Since they carry QCD color, pairs of sufficiently light leptoquarks could be produced copiously in $\bar{p}p$ collisions via quark-antiquark annihilation and through gluon-gluon fusion; at $\sqrt{s} = 1.8$ TeV 'sufficiently light' means leptoquarks with masses of order 100 GeV or less. In Figure 2.2 we show the lowest order contributions to the production of a pair of generic (i.e. any generation) leptoquarks. Note that conservation of lepton flavor requires that the pair of leptoquarks be of the *same* generation.

The leptoquark pair production processes shown in Figure 2.2 are of $\mathcal{O}(\alpha_s^2)$, by which we mean that the resulting cross section is proportional to $\alpha_s^2$. As noted in Section 1.4, the QCD coupling constant $\alpha_s(Q)$ decreases as the momentum scale Q increases. The momentum transfer required to produce a pair of massive leptoquarks (typically $Q \sim M_{LQ}$) is large enough that $\alpha_s(M_{LQ}) \sim 0.1$, and so to a reasonable approximation we are justified in considering only the lowest order pair production diagrams. Smaller contributions from higher-order processes are considered by the authors of Reference [37, 38] and are discussed further in Chapter 6.

Having produced an $LQ_i\overline{LQ_i}$ pair, the leptoquarks decay to generation-i quarks and leptons in either the charged-lepton mode with $\mathrm{BR}(LQ \to q + l^\pm) = x$, or in the neutrino channel with $\mathrm{BR}(LQ \to q' + \nu_l) = 1 - x$. The possible decay modes for the three generations of leptoquarks are then

| | | |
|---|---|---|
| $LQ_1 \to u + e^-$ (BR= $x_1$) | or | $LQ_1 \to d + \nu_e$ (BR= $1 - x_1$) |
| $LQ_2 \to c + \mu^-$ (BR= $x_2$) | or | $LQ_2 \to s + \nu_\mu$ (BR= $1 - x_2$) |
| $LQ_3 \to t + \tau^-$ (BR= $x_3$) | or | $LQ_3 \to b + \nu_\tau$ (BR= $1 - x_3$) |

Note: The decay branching fractions $x_i$ are not known a priori. and, along with the leptoquark masses $M(LQ_i)$, are left as free parameters in this analysis.

For generation-1 and generation-2 we expect the quarks from leptoquark decays to hadronize into jets of observable particles, and we would therefore expect clean dilepton+dijet event signatures from $LQ_1$ or $LQ_2$ pairs. In the case where one or more of the leptons is a neutrino, an event will be characterized by missing energy. Given that a leptoquark can decay in the charged- or neutral- lepton mode there are three possible event signatures per generation at least for 1st and 2nd generation leptoquarks. The situation for 3rd generation leptoquarks is somewhat complicated by the fact that $\tau$-leptons decay rapidly to other particles (quarks and/or lighter leptons). In Figure 2.3 we show the three signatures for first-generation leptoquark pair production, this being the subject of this thesis. For all three generations $LQ_i (i = 1-3)$, the relative rate for each channel depends on the unknown charged branching fraction $x_i$ as follows (assuming each channel is kinematically allowed):

$$\begin{aligned} l_i^+ l_i^- &+\text{dijet} \qquad \text{Rate} \sim x_i^2 \\ l_i^\pm \nu_{l_i} &+\text{dijet} \qquad \text{Rate} \sim 2x_i(1-x_i) \\ \nu_{l_i}\bar{\nu}_{l_i} &+\text{dijet} \qquad \text{Rate} \sim (1-x_i)^2 \ . \end{aligned}$$

In events containing one or more charged leptons we can form lepton-jet invariant mass combinations and so directly reconstruct the leptoquark mass. With many such events we would see a peak in the lepton-jet mass spectrum. The issue of reconstructing leptoquark masses in practice will be taken up later in this thesis when we describe the analyses in each of the individual decay channels.

For generation-3 leptoquarks the situation is more complicated. The bottom and top quarks and the tau lepton are so heavy that their subsequent decay can lead to events with complex topologies containing several jets and sometimes several electrons and/or muons. In such events we would lose our simple dilepton-dijet signature, along with our ability to reconstruct the leptoquark mass. At the present time the mass of the Standard Model top quark is known to be greater then 91 GeV at 95% CL [6]. In the case that $M(LQ_3) < M_t$ one of the two $LQ_3$ decay channels would be closed, leaving only $LQ_3 \to b + \nu_\tau$ (or $b + \tau$ depending on the model-dependent charge assignment for the $LQ_3$. Because of the lack of



a clean signal, and the many difficulties involved in identifying tau leptons in multi-tau plus multijet events, and because of the loss of ability to reconstruct a leptoquark mass peak we believe a search for generation-3 leptoquarks at hadron-colliders would be extremely difficult.

Single Leptoquark Production

As well as being formed in pairs, leptoquarks can be produced singly at hadron colliders through such leading order processes as $qg \to LQ+l$ (Figure 2.4). To conserve lepton number, the production of a single generation-i leptoquark requires an accompanying generation-i lepton ($l^\pm$,$\nu_l$). Depending on whether the accompanying lepton is charged or neutral, and also on how the leptoquark decays, the signatures for single leptoquark production are $l^+l^-$+jet, $l^\pm$+jet+missing energy, or monojet events with missing energy. By associating the correct lepton with the single jet in the event we should also be able to reconstruct the leptoquark mass, as for leptoquark pair production.

Unlike pair production where the rate is of $\mathcal{O}(\alpha_s^2)$, the single leptoquark cross section is proportional to $\alpha_s \alpha_{LQ}$, where $\alpha_{LQ}$ characterizes the strength of the q-l-LQ coupling. Since the three new couplings $\alpha_{LQ}^i$ are not predicted by leptoquark models, the rate at which we produce single leptoquarks is unknown. The best constraints on $\alpha_{LQ}^1$ come from measurements of the forward-backward asymmetry in $e^+e^-$ collisions and comparisons with Standard Model predictions; t-channel exchange of a light first generation leptoquark with strong q-l-LQ couplings would significantly alter the angular distributions of the final state particles. This is discussed by Hewett and Rizzo [40] who find that $\alpha_{LQ}^1 < 0.1$ assuming $M(LQ_1) < 100$ GeV and $|A_{FB}(\text{Measured}) - A_{FB}(SM)| < 5\%$. For tighter constraints on $\Delta A_{FB}$, it is found that $\alpha_{LQ}^1$ becomes even smaller. In light of this, the generation-1 single leptoquark rate is almost certainly less than that for pair production. Furthermore we expect an approximately 5-fold increase in the background event rate once we require only one jet in an event rather than two (Equation 6.9). For these reasons we do not consider single production any further in this thesis. Though not considered in this thesis, we note that for generation 2 and 3 leptoquarks there are no similar constraints on the corresponding $\alpha_{LQ}^{2,3}$. In principle the single

leptoquark production rate could then be higher than that for pairs, though the observation about increased background rate still applies.

### 2.3.2 Leptoquarks at $e^+e^-$ Colliders

Leptoquarks are charged particles and so have unambiguous couplings to the photon. They also couple to the $Z^0$, though the electroweak coupling strengths of the leptoquark are model dependent. With both $\gamma$ and $Z^0$ couplings, leptoquarks of all three generations can be pair-produced in $e^+e^-$ collisions, leading order diagrams for which are shown in Figure 2.5. We also show an $\mathcal{O}(\alpha_{EM}^2\alpha_{LQ})$ process which can lead to single leptoquark production. Note there are no $\mathcal{O}(\alpha_{EM}^2)$ processes for the production of a single fractionally charged leptoquark at an $e^+e^-$ collider. The LQ pair production cross sections are expected to be much smaller than those arising from collisions between quarks of comparable energy at hadron colliders, simply because $\alpha_{EM}/\alpha_s \ll 1$ at current accelerator energies.

Once a pair of generation-i leptoquarks has been produced in an $e^+e^-$ collision, the subsequent leptoquark decays lead to event signatures identical to those already described for pair production at $\bar{p}p$ colliders. We therefore do not discuss event signatures at $e^+e^-$ accelerators any further.

### 2.3.3 Leptoquarks at $e^\pm p$ Colliders

Electron-proton colliders are, in a sense, the perfect place to look for generation-1 leptoquarks. A quark from a high energy proton can fuse with an electron to form a leptoquark which then promptly decays either back to $u + e$, or to $d + \nu_e$. The leading order Feynman diagrams for this s-channel resonant formation are shown in Figure 2.6, and the corresponding sub-process cross section is given by

$$\hat{\sigma} = \frac{1}{48\pi Q^2}\left\{\frac{2\times 3\times \lambda_L^4 Q^4}{(Q^2-M_{LQ}^2)^2+\Gamma_L^2 M_{LQ}^2} + \frac{3\times\lambda_R^4 Q^4}{(Q^2-M_{LQ}^2)^2+\Gamma_R^2 M_{LQ}^2}\right\} \qquad (2.6)$$

where $M_{LQ}$ is the mass of the first-generation leptoquark [41]. In the Standard Model, electron-proton interactions occur via the mediation of the electroweak gauge bosons, a process known as deep inelastic scattering (DIS) and shown in



Figure 2.7. Since DIS initial and final states are the same as those for resonant leptoquark production, the amplitudes from both processes must be added. This leads to the superposition of a resonant signal on a Standard Model background, along with some interference between the two.

At the time of writing, the HERA $e^-p$ collider has recently begun operating at a center of mass energy of $\sqrt{s} = 315$ GeV. In the presence of a 200 GeV generation-1 leptoquark, the differential cross section $d^2\sigma/dxdQ^2$ for HERA energies is shown in Figure 2.8 [42]. Here x is the fraction of energy carried by the colliding up-quark. The leptoquark resonance is immediately obvious, as is the asymmetry arising from the interference of leptoquark and DIS amplitudes. The HERA leptoquark event rate varies as $\lambda_{L,R}^4$ and $1/M_{LQ}^4$ and so the running time required to see such a resonance is very sensitive to the value of $\lambda/M$, In Reference [43] $5\sigma$ leptoquark discovery limits are given as a function of leptoquark mass and $F_R$ assuming one year of running.

We finally note that, unlike $\bar{p}p$ and $e^+e^-$ accelerators, $ep$ colliders are unable to directly produce generation-2,3 leptoquarks of the type considered in this thesis.

## 2.4 Earlier Searches for Leptoquarks

### 2.4.1 $e^+e^-$ Colliders

In 1984 some excitement was generated by a paper published by the CELLO collaboration [44] at PETRA ($\sqrt{s} = 43.45$ GeV). This paper reported an unusual event which contained two isolated oppositely-charged muons and two hadronic jets. The number of such events expected from Standard Model sources in the 3.9 pb$^{-1}$ data set was estimated by CELLO to be around $10^{-3}$. The muon-jet invariant masses were $19.4 \pm 1.3$ GeV and $22.2 \pm 1.6$ GeV respectively, and some authors speculated that the event arose from the production and subsequent decay of a pair of generation-2 leptoquarks [45, 34]. The AMY collaboration at TRISTAN in Japan then performed their own search for leptoquarks [46], this time using 27.4 pb$^{-1}$ of data collected at center-of-mass energies in the range

$\sqrt{s} = 50-60.8$ GeV. No evidence was found for either generation-1 or generation-2 leptoquarks and AMY excluded $M(LQ_1) < 22.6$ GeV and $M(LQ_2) < 23.2$ GeV at 95% C.L.

In the 1990 running period the LEP $e^+e^-$ collider was operated at center of mass energies between 88.2 and 94.3 GeV. This led to the possibility of producing leptoquarks in pairs right up to the kinematic limit of $M_{LQ} \simeq 47$ GeV. All four experiments at LEP (L3, OPAL, DELPHI, and ALEPH) looked for leptoquarks, and have since published their results [47, 48, 49, 50]. No evidence was found for the pair-production of any generation of leptoquark having a mass less than around 44 GeV, independent of charged branching fraction. The L3 and OPAL results are shown in Figure 2.9.

### 2.4.2 $\bar{p}p$ Colliders

Upgraded from a proton synchrotron accelerator in 1981, the SPS at CERN was the first, and prior to the Fermilab Tevatron, the only $\bar{p}p$ collider in the world. Between 1981 and 1983 the SPS was operated at a center of mass energy of $\sqrt{s} = 540$ GeV, and at $\sqrt{s} = 630$ GeV from 1984 to 1990, after which the collider shut down indefinitely as the new LEP $e^+e^-$ program got underway.

All three generations of leptoquarks have been searched for in $\bar{p}p$ collisions at CERN. The UA1 collaboration first reported results of a search for generation 2 and 3 leptoquarks in 1987 [51, 52], while more recently UA2 have published their results for generation-1 leptoquarks [53]. Treating them in historical order, we now consider these analyses in more detail.

Generation-3 Leptoquarks

As discussed earlier, the decay of a pair of third generation leptoquarks leads to events containing two jets and either a $\tau^+\tau^-$, $\tau^\pm\nu_\tau$, or $\nu_\tau\bar{\nu}_\tau$ lepton pair. UA1 considered the $\tau^+\tau^-$+dijet channel in the case where both $\tau$'s decay hadronically, and also in the case where one $\tau$ decays hadronically and the other decays to a muon via $\tau \rightarrow \mu\nu_\mu\nu_\tau$. In both cases it was hoped that the narrow jets resulting from hadronic $\tau$ decays could be distinguished from those produced in standard



QCD multijet events.

For the double hadronic $\tau$-decay channel UA1 planned to use their 4-jet data set (0.7 pb$^{-1}$) as an event sample. However, a preliminary study found that the signal would be completely dominated by QCD 4-jet production (70 QCD events vs. 0.1 signal events), and the search in this channel was abandoned.

In the single muon channel around 700 background events, where a QCD jet was misidentified as a $\tau$ jet, were expected in the isolated-$\mu$ + 3jet data sample. When compared to 12 predicted leptoquark events, it was again concluded that this channel held no hope of observing a signal.

Generation-2 Leptoquarks

In the $\mu^+\mu^-$+dijet channel, UA1 found one candidate event after all cuts, while $1.8 \pm 0.9$ events from background were predicted. The $\mu$-jet invariant masses were 18.4 and 28.1 GeV, each with a 25% error, and the event was therefore not inconsistent with the existence of a 20-GeV leptoquark. Given the expected signal rate at CERN, the unknown charged branching fraction for $LQ_2 \rightarrow \mu^\pm + s$ would then have to be $< 10\%$ to account for only one such event being seen. Using the predicted rate for other leptoquark masses and assuming this event to be signal, UA1 set limits on $M(LQ_2)$ and the charged branching fraction. At 50% charged branching fraction UA1 excludes $M(LQ_2) < 35$ GeV at 90% C.L. using this channel.

The single-$\mu$ + dijet data sample yielded 60 events after all cuts, while 32.5 events were predicted from background sources. An excess of events was not claimed since the production cross sections used in rate estimation had large theoretical uncertainties associated with them. Instead a likelihood separation of signal from background was used. The likelihood distribution for the data was found to be in good agreement with background predictions, and again limits were set on the leptoquark mass and charged branching fraction.

Finally, in the case where both leptoquarks decayed to $\nu_\mu + c$, UA1 used their large-missing $E_T$ sample to exclude the possibility of very small charged branching fractions. The results of all three searches are shown in Figure 2.10

(from Reference [51]). Using all three channels, UA1 can exclude $M(LQ_2) < 33$ GeV at 90% C.L. independent of the unknown charged branching fraction, except for a small window in the region $21 < M(LQ_2) < 25$ GeV and $\mathrm{BR}(LQ_2 \rightarrow \mu^+ + s) < 10\%$.

Generation-1 Leptoquarks

Using $13\mathrm{pb}^{-1}$ of data collected over the running period 1988-1990, the UA2 collaboration has looked for generation-1 leptoquarks in the $e^+e^-$+dijet and $e^\pm\nu_e$+dijet channels. In the dielectron+dijet channel, transverse energy requirements were placed on the electrons and jets to eliminate low-$E_T$ Drell-Yan and QCD backgrounds, while $Z^0$ + 2jet events were removed by cutting events with $80 < m(e^+e^-) < 100$ GeV. After all cuts, UA2 observed no events and set limits on the charged branching fraction $\mathrm{BR}(LQ_1 \rightarrow e^\pm + u)$ and leptoquark mass $M(LQ_1)$. The highest mass limit is obtained at BR= 100%, and in this case UA2 exclude $M(LQ_1) < 74$ GeV at 95% CL.

In the $e^\pm\nu_e$+dijet channel, which is sensitive to intermediate values of the charged branching ratio, UA2 used a high-$E_T$ electron data set and imposed missing-$E_T$ and transverse-mass cuts to reduce QCD and $W^\pm$+2jet backgrounds. After initial cuts, 6 events were found in the transverse mass range $60 < M_T^{e\nu} < 90$ GeV. UA2 estimated 5 events in this region using QCD calculations of $W^\pm$ + 2jet rates (within large theoretical uncertainties). After removing this transverse mass range from both signal and background processes, UA2 reported zero events observed and set mass and branching ratio limits accordingly. The results are shown in Figure 2.11, taken from Reference [53], along with limits from LEP. UA2 combine results from both channels, and at BR = 50% exclude $M(LQ_1) < 67$ GeV at 95% CL.

## 2.5 An Outline of the Thesis

The remainder of this thesis describes the results of a search for leptoquarks in $\overline{p}p$ collisions at $\sqrt{s}$ = 1.8 TeV using 4.05 $\mathrm{pb}^{-1}$ of data collected using the CDF detector over the running period 1988-1989.



In the next chapter we begin by describing the experimental setup, namely the Tevatron accelerator and those parts of the CDF detector most relevant to this work. Chapter 4 is devoted to how the data sample central to this thesis was constructed, while Chapter 5 explains how we identify and reconstruct the properties of leptons and jets in events at CDF.

In Chapter 6 we describe a search for generation-1 leptoquark pairs in the $e^+e^-$+dijet channel, that is where both leptoquarks are assumed to have decayed to an $e + u$ pair. Properties of the signal are described, as are the dominant sources of background and methods for their removal. Results of the analysis are presented at the end of the chapter.

Chapter 7 extends the generation-1 leptoquark search to the case where one leptoquark decays in the charged lepton channel ($e + u$) while the other decays to $\nu_e + d$, giving an $e^\pm\nu_e$+dijet signature. Again signal and background are compared, and results which complement those of the dielectron+dijet analysis are presented.

Finally in Chapter 8 we summarize the results of analyses and present the conclusions of this thesis.

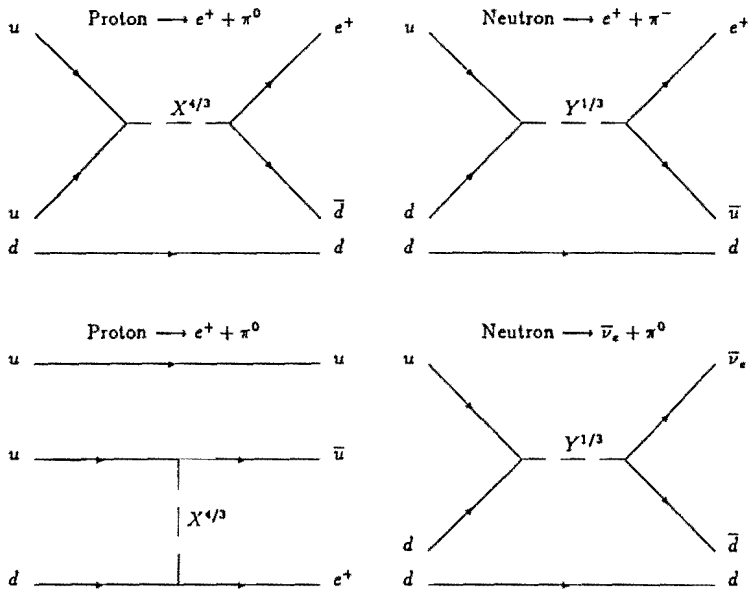


Figure 2.1: Examples of nucleon decay in $SU(5)$.

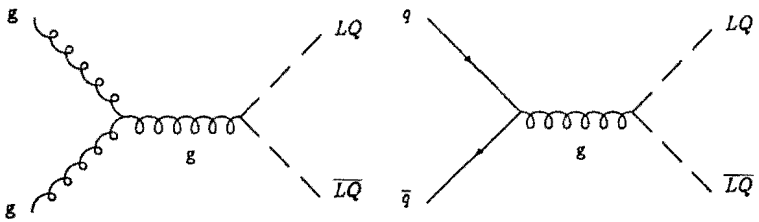


Figure 2.2: Examples of $\mathcal{O}(\alpha_s^2)$ processes contributing to the production of pairs of leptoquarks in $\overline{p}p$ collisions.



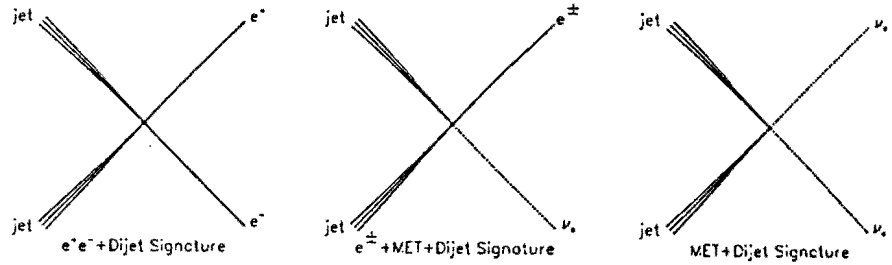


Figure 2.3: Event signatures from the decay of an $LQ_1\overline{LQ}_1$ pair.

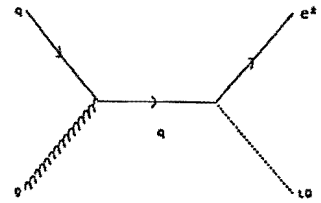

Figure 2.4: A leading order process contributing to single $LQ_1$ production in $\overline{p}p$ collisions.

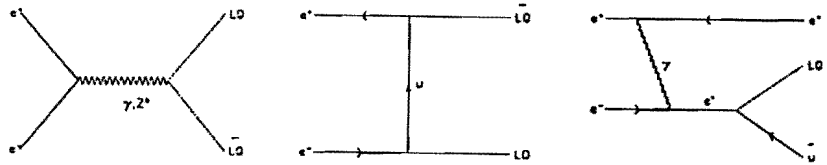

Figure 2.5: Processes leading to single and pair production of generation-1 leptoquarks at $e^+e^-$ colliders.

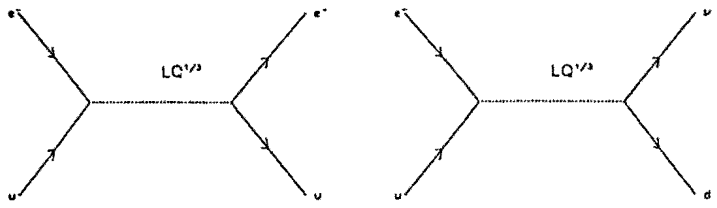

Figure 2.6: The s-channel resonant formation and subsequent decay of a generation-1 leptoquark in $ep$ collisions.

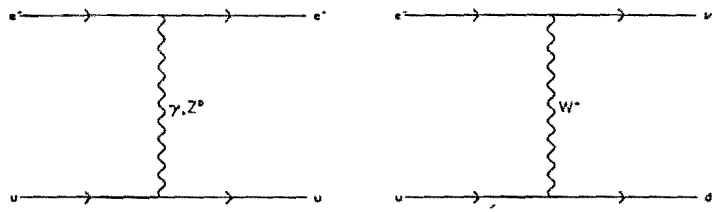

Figure 2.7: Standard Model deep inelastic scattering processes in $ep$ collisions.

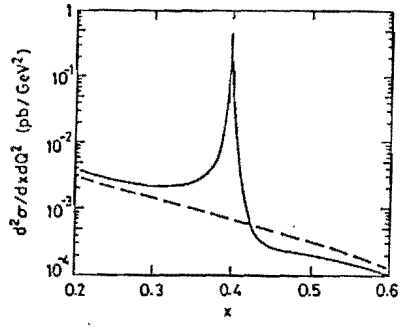


Figure 2.8: Resonant leptoquark production (solid) and DIS background (dashed) in $e^-p$ scattering at $\sqrt{s} = 315$ GeV and $Q^2 = 10^4$ GeV$^2$ (from DESY-86-150).



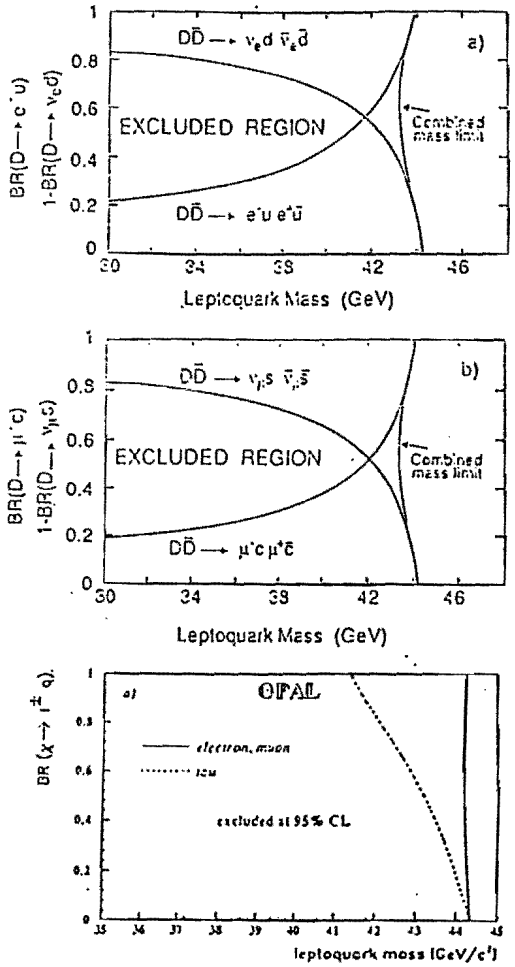


Figure 2.9: Limits from L3 on the masses and branching ratios of the $LQ_1$ and $LQ_2$, and limits from OPAL on all three leptoquark generations.

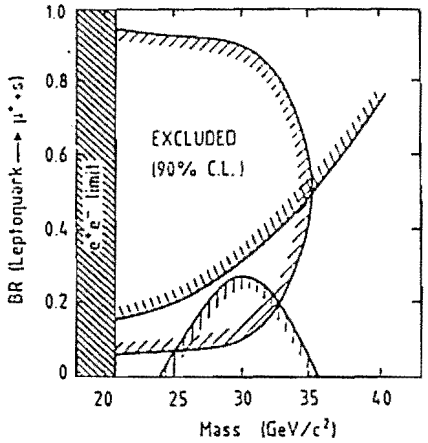


Figure 2.10: Limits from UA1 on the mass of the second generation leptoquark and the charged branching ratio $x_2$ =BR($LQ_2 \rightarrow \mu^{\pm} + s$).

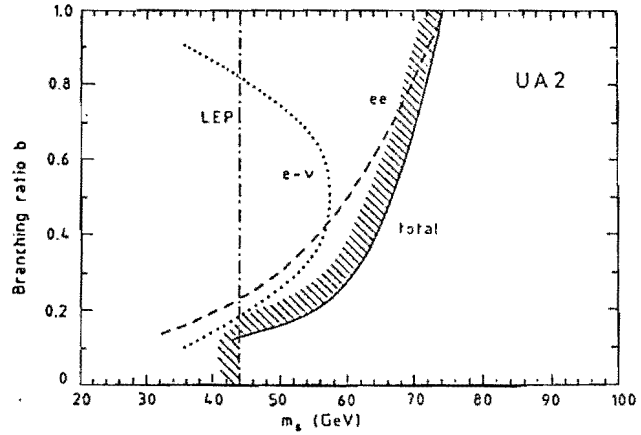


Figure 2.11: Limits from UA2 on the mass of the first generation leptoquark and the charged branching ratio $x_1$ =BR($LQ_1 \rightarrow e^{\pm} + u$). Results for individual and combined channels are shown.



# Chapter 3

# The Collider Detector at Fermilab

## 3.1 The Tevatron $\overline{p}p$ Accelerator

The Tevatron, located at Fermilab in Batavia, Illinois, is currently the highest energy proton-antiproton collider in the world. With a circumference of almost four miles, it uses superconducting bending magnets and accelerates counter-circulating beams of protons and antiprotons to energies of 900 GeV, giving an available center of mass energy of 1.8 TeV.

The $\overline{p}p$ interaction rate R is

$$R = \sigma_{\overline{p}p} \cdot \mathcal{L}. \tag{3.1}$$

Here $\sigma_{\overline{p}p}$ is the proton-antiproton total scattering cross section, which at a center-of-mass energy of $\sqrt{s}$ = 1.8 TeV is approximately 70 millibarns (1 barn = $10^{-24}$cm$^2$).

The beam luminosity $\mathcal{L}$ is a measure of beam intensity and is given by

$$\mathcal{L} = n \cdot f \cdot \frac{N_{\overline{p}} N_p}{A} \tag{3.2}$$

where n is the number of particle bunches in each beam (usually six), f is the revolution frequency of each bunch in the Tevatron, N is the number of particles in a bunch, and A is the cross sectional area of the beam. During the 1988-89 run a proton bunch contained typically $7 \cdot 10^{10}$ particles, while the number of antiprotons in a bunch was around $3 \cdot 10^{10}$.

With a transverse beam size of 70$\mu m$ the peak beam luminosity was around $2 \cdot 10^{30}$ cm$^{-2}$s$^{-1}$, giving a rate of 140,000 $\overline{p}p$ interactions per second.

We now briefly describe the production of beams of protons and antiprotons and how these beams are tuned to improve the $\bar{p}p$ interaction rate. A more detailed description can be found in [54].

The FermiLab accelerator complex is shown in Figure 3.1. Protons from an 800-keV Cockcroft-Walton generator are passed through a 200-MeV linac and from there into a booster ring where their energy is increased up to 8 GeV. The booster then injects the protons into the 4-mile Main Ring, originally used as a 400-GeV proton accelerator for the fixed target program.

The protons are now accelerated up to 120 GeV, then focussed onto a tungsten fixed target to produce antiprotons. The antiprotons travel through a lithium lens and enter the debuncher ring with an energy of 8.5 GeV. Stochastic cooling and bunch rotation techniques reduce the energy spread and transverse motion of the antiprotons. After approximately two seconds in the debuncher, the antiprotons are transferred to the accumulator ring. The accumulation of antiprotons is called 'stacking', and with an accumulation rate of $\sim 2 \cdot 10^{10}$ $\bar{p}$'s per hour, it can take many hours to build a stack sufficient to provide the required antiproton beam luminosity.

Once enough antiprotons have been created and stored, a bunch of $\sim 3 \cdot 10^{10}$ particles is injected into the Main Ring and accelerated up to 150 GeV. The bunch is then injected into the superconducting Tevatron ring, lying directly underneath the Main Ring, where 6 bunches of previously accelerated protons are already circulating in the opposite direction at 150-GeV.

The injection process from the accumulator is repeated until there are 12 bunches in the Tevatron, 6 proton and 6 antiproton. The beams are now 'ramped' up to 900-GeV and then focussed as much as possible by 'low-$\beta$' quadrupole magnets ($\beta$ being a measure of the transverse size of the beam). The beam crossing points are finally adjusted (cogging) so that one of the primary interaction regions will be centered within the CDF detector. With colliding proton-antiproton beams at maximum luminosity we are now ready to take data with our detector.



## 3.2 The CDF Detector: An Overview

The CDF detector is a large general purpose detector designed to study the leptons and jets that emerge from proton-antiproton collisions at 1.8 TeV. In Figures 3.2 and 3.3, we show isometric and elevation views of the detector and its various subcomponents.

The detector is both forward-backward and azimuthally symmetric, and the trajectories of particles within it are described in terms of right handed cylindrical coordinates (r,$\phi$,z). The origin of the coordinate system is naturally taken to be at the center of the detector, this being where the proton-antiproton collisions are expected to occur. The positive z-axis follows the direction of the proton beam, while the $\phi = 0$ axis points towards the center of the accelerator ring.

Other coordinates which are frequently used, and which will be employed throughout this thesis, are the polar angle

$$\theta = \tan^{-1}\left(\frac{r}{z}\right) \tag{3.3}$$

and the related quantity pseudo-rapidity

$$\eta = -\log(\tan\frac{\theta}{2}) \tag{3.4}$$

The so called 'central' part of the detector provides energy and momentum measurements over the polar angle region $30° < \theta < 90°$, while the Plug and Forward detectors cover the regions $10° < \theta < 30°$ and $2° < \theta < 10°$ respectively. The use of all three regions in event reconstruction allows almost complete $4\pi$ coverage. Note that for simplicity we refer only to $\theta < 90°$ ; coverage is symmetric in the $-z$ direction ($\theta > 90°$).

While it is beyond the scope of this thesis to describe the individual detector subsystems in great detail, we will now attempt to present the main features. A much more comprehensive description of the CDF detector can be found in [55], and in the accompanying references.

### 3.3 The Vertex Time Projection Chambers (VTPC)

While we expect proton-antiproton collisions to occur, on average, at z=0 in the CDF coordinate system (i.e. at the center of the detector), the reality is that finite bunch sizes lead to a Gaussian distribution in the primary event vertex z position. Over the length of a typical run, the rms standard deviation in the position of the event-vertex along the beam pipe was around 35cm.

The Vertex Time Projection Chamber system (VTPC) is a set of 8 tracking modules that surround the beam-pipe. Their primary function is to provide accurate reconstruction of the location of the primary event-vertex, or of several such vertices should there be more than one hard collision in the same beam crossing. To do this, tracks from charged particles leaving the primary vertex are reconstructed and extrapolated back to the point at which the interaction took place. In Figure 3.4 we show a projection of VTPC wire hits from a typical event. By constraining the tracks to emerge from a single point we are able to locate position of the primary vertex to within ±1mm.

Knowledge of the location of the z-vertex is important in order to correctly derive transverse energies from measured calorimeter energies ($E_T = E \sin\theta$). The ability to identify more than one primary vertex helps us distinguish between random multiple-interactions and single vertex events when measuring, for example, jet-multiplicity and lepton+multijet rates.

Since we will be interested in electrons emerging from the primary vertex, an important secondary function of the VTPC is to distinguish such electrons from photons, including those which have converted to an $e^+e^-$ pair after leaving the VTPC but before reaching the Central Tracking Chamber (CTC). This distinction is made by requiring that there be a charged VTPC track associated with an electron candidate. We discuss this further in Chapter 5.



### 3.4 The Central Tracking Chamber (CTC)

The Central Tracking Chamber is a large cylindrical drift chamber operating inside 1.4 Tesla axial magnetic field. Its primary function is to allow the full reconstruction of 3-dimensional tracks left by charged particles passing through it. By measuring the curvature of a given track in the $r-\phi$ plane we can deduce the corresponding transverse momentum $P_T$, while the direction of the curvature gives us the charge of the particle.

The CTC contains 36,504 sense and field-shaping wires, each 3.2 meters long. The gas inside the chamber is a 50-50 mixture of argon and ethane, and the wires are arranged so as to provide an approximately uniform drift field of 1350 V/cm.

The wires are grouped into 84 cylindrical layers, and these into 9 'superlayers' (see Figure 3.5). Within a superlayer wires in adjacent layers are grouped into measurement cells which again can be seen in the Figure 3.5. Five axial superlayers with twelve sense wires in each cell alternate with four stereo superlayers containing six wires per cell. The wires in the axial superlayers run parallel to the beam direction and allow a measurement of the transverse momentum $P_T$ of an isolated particle with a resolution of

$$\frac{\Delta P_T}{P_T} \sim 0.0011 \cdot P_T. \tag{3.5}$$

In the stereo superlayers, the six wires are tilted at 3° relative to the beam axis, permitting 3-D track reconstruction in the r-z plane.

With so many wires in the CTC, excellent track separation and position measurements are attainable. In the $r-\phi$ plane the position resolution is of order 0.2mm, while in the z-direction it is around 4mm.

By comparing the number of tracks and their momenta to energy deposited in the calorimeter, we can measure such quantities as the charge particle fraction in jets. Of more relevance to this analysis, the presence of a CTC track can distinguish electrons from photons, while in the case of muons the momentum of a CTC track, correctly matched to hits in the muon chambers, gives us our best measurement of the muon momentum. Finally a CTC track can allow us

to account for missing transverse energy in the case where a particle has passed through a crack in the detector calorimetry and whose energy has therefore been substantially underestimated, if measured at all.

## 3.5 CDF Calorimetry

Calorimeters measure the energy of both charged and neutral particles, while tracking chambers provide complimentary measurements of both the charge and momenta of charged particles. For massless objects energy and momentum are equivalent, and in this case the use of both central calorimetry and the CTC provides a cross check that both detectors are working as they should.

In each of the three detector regions at CDF (central, plug, and forward) there are two distinct calorimeters, one to measure electromagnetic energy (CEM, PEM, and FEM), and one to measure hadronic energy (CHA, PHA, and FHA). All of these detectors are sampling calorimeters. This means that they use alternating layers of a heavy absorbing material, which causes an incoming particle to shower, and layers of an active medium in which the energy of the developing shower is 'sampled'. The absorber is lead for the EM calorimeters, and iron for the hadron calorimeters. The active medium depends on the particular calorimeter in question: in the central region polystyrene (EM) or acrylic (HAD) scintillators are used, while the plug and forward detectors are gas calorimeters. The geometric design of all the CDF calorimeters is based on a projective tower geometry as will be explained in the following sections, where we discuss the individual calorimeters in more detail.

### 3.5.1 Central Calorimeters

Covering the region $-1 < \eta < 1$, the central calorimeter (CEM+CHA) forms a cylinder that is concentric with the smaller radius CTC and VTPC detectors. Unlike the one-piece CTC, the calorimeter is constructed from two cylindrical halves symmetric about the $z = 0$ plane. Each half is divided into 24 azimuthal segments, or 'wedges', each of which subtends 15° in $\phi$. This segmented structure,



and the calorimeter halves, can be seen in the isometric view of the CDF detector shown in Figure 3.2 .

An individual wedge containing both CEM and CHA calorimeters is shown in Figure 3.6. The CEM consists of 31 alternating layers of lead absorber (0.32cm thick) and polystyrene scintillator (0.5 cm thick), light from the scintillators being guided into, and collected by, a phototube array. In addition, high spatial resolution of the developing shower is obtained by the use of a set of strip chambers (CES) located 6 radiation lengths inside the CEM, this being the position of the maximum development of the shower). The total depth of the CEM is 18 radiation lengths . In the CHA there are 32 layers. The absorber consists of 2.5 cm thick steel plates, while 1.0cm thick layers of acrylic scintillator are used to sample the energy of the hadronic shower.The energy resolution of the CEM is

$$\frac{\sigma(E)}{E} \simeq \frac{13.5\%}{\sqrt{E \sin\theta}} \tag{3.6}$$

measured with test-beam electrons, while the CHA resolution is

$$\frac{\sigma(E)}{E} \simeq \frac{80\%}{\sqrt{E \sin\theta}} \tag{3.7}$$

as measured with test-beam pions.

To provide segmentation in the $\eta$ direction the central wedges are further divided into 10 sections, each subtending 0.1 units of $\eta$, and each read out separately. The boundaries of these $15° \times 0.1\eta$ sections of calorimeter lie in planes of constant $\eta$ and $\phi$, and so in three dimensions form projective towers pointing back toward the origin. This can be seen more clearly in the side view of a central wedge (Figure 3.7). The projective tower geometry is continued into the plug and forward regions (next section), as shown in Figure 3.8, though with finer $\phi$ segmentation in these regions.

Combining both $\eta$ and $\phi$ segmentation we obtain a detector capable of providing a detailed quantitative and geometrical picture of the energy flow out from the primary vertex in an event.

### 3.5.2 Plug and Forward Gas Calorimeters

Like their central counterparts, the plug and forward calorimeters are sampling detectors based on a projective tower geometry. The absorbing layers are again lead for the PEM and FEM calorimeters, and are each of thickness 0.27cm and 0.48cm respectively. For the PHA and FHA, 5.1cm thick steel is used. Unlike the central calorimeter, however, the sampling medium in both plug and forward regions is a 50-50 argon-ethane gas mixture rather than a scintillator. Instead of collecting light with phototubes, the gas calorimeters measure the gas ionization as particles pass through it. The number of primary electrons produced is a linear function of the incoming particle's energy, which is what we mean when we say the gas calorimeters are 'proportional chambers'. Ionized electrons within the gas accelerate towards anode wires, and in doing so ionize yet more of the gas producing secondary electrons. This results in an electron 'avalanche'.

For each primary electron approximately $10^5$ secondaries are produced under normal CDF operating conditions, the ratio of secondaries to primaries being known as the gas-gain. Our measured signal is then a function of both the energy of the ionizing particle and the gas-gain. Under ideal circumstances the gain would be constant. Unfortunately, gas-gain is a complex function of several variables, each of which must be stabilized as much as possible and monitored continuously so that the detector energy scale can be compensated. These variables include the pressure, temperature, and composition of the gas, and the high voltage on the anode wires. A reference energy scale is provided by $Fe^{55}$ sources mounted on monitor tubes through which argon-ethane Gas flows under the same conditions as for the calorimeters. By measuring shifts in the position of the 6-keV peak, we can deduce the change in the gas-gain, and hence in our detector energy scale.

Finally the detector energy resolutions are measured to be

$$\frac{\sigma(E)}{E} \simeq \frac{28\%}{\sqrt{E}} \tag{3.8}$$

for the PEM and FEM calorimeters, and

$$\frac{\sigma(E)}{E} \simeq \frac{130\%}{\sqrt{E}} \tag{3.9}$$



for the PHA and FHA.

## 3.6 The Central Muon Detectors

Muons are minimum-ionizing particles, meaning that they have a very low interaction rate with matter as compared to electrons or pions, for example. The consequences of this are that muons deposit little energy in the CDF calorimeters, typically $\sim 0.5$ GeV in the EM section, and $\sim 2$ GeV hadron section (assuming, of course, that $E_\mu > 2.5$ GeV). Calorimeters are therefore of little use in measuring muon energy. However, from the track curvature in the CTC we can reconstruct the muon momentum. A high $P_T$ track in the CTC, and little or no energy in the corresponding calorimeter tower (EM or HAD), is our first hint that we are dealing with a muon.

In the CDF central region, muon detectors in the form of drift chambers were built onto the back of the calorimeter wedges (Figure 3.3) and cover the range $-0.63 < \eta < 0.63$. To reach these chambers, a particle must have passed through both the CEM and CHA and must have lived long enough to travel the 3.5 meters from the beam line. The construction of the chambers is illustrated in Figure 3.9. As in the CTC and gas calorimeters, the central muon (CMU) detectors use a 50-50 argon-ethane gas mixture as the active medium. Ionization of the gas leads to anode wire pulses in each of the four chambers the muon traverses. By measuring the time of arrival of each pulse and knowing the drift velocity of an electron within the a cell, we can deduce the path of the muon in the $r-\phi$ plane (Figure 3.9). A left-right ambiguity as to which side of the wires the muon passed is resolved by offsetting the top two planes of wires relative to the bottom two. The direction of muon travel in the $z$-direction can be determined by measuring the relative pulse heights at both ends of the anode wires. Hits in the muon chambers are used to reconstruct the path of the muon in three dimensions. This path is extrapolated back through the central calorimetry to the CTC where we would expect to find a charged track left by the muon. The matched track is then used to find the muon momentum.

For the 1988-89 run the CDF detector had no further muon coverage in the range $0.63 < |\eta| < 1.9$. Although not used in this analysis, large steel toroids between three sets of drift chambers did provide additional muon detection capability in the forward detector region $1.9 < \eta < 4.0$, or equivalently in the range $2° < \theta < 17°$ with respect to the beam axis (and similarly in the -z direction). These are shown in the isometric view of CDF in Figure 3.2. Muon coverage has been substantially increased for the 1992 run.



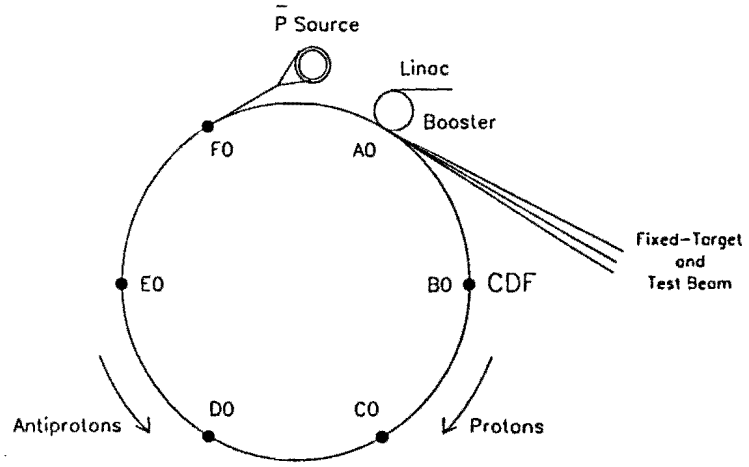


Figure 3.1: Accelerators at FermiLab.

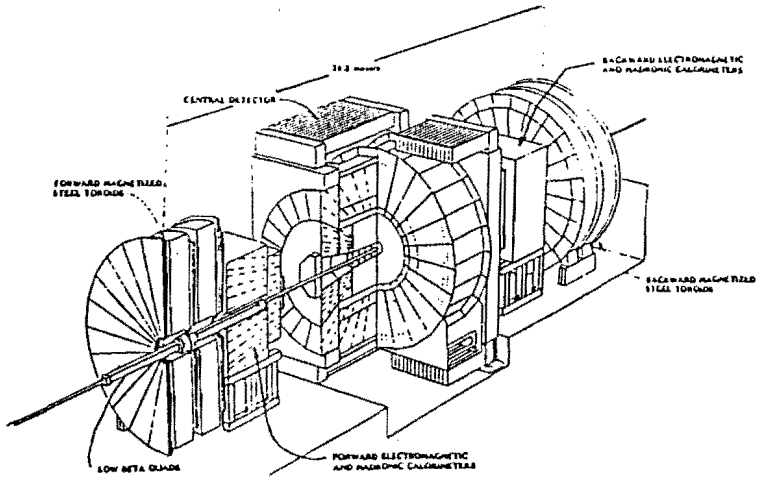

Figure 3.2: Isometric view of the CDF detector.

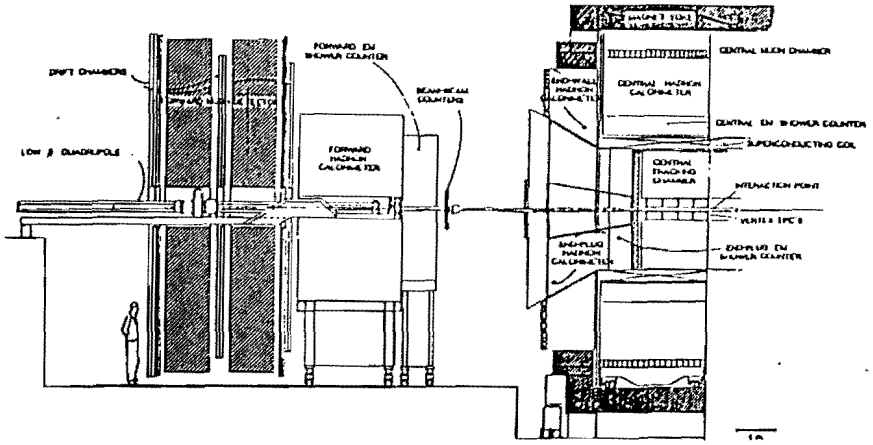

Figure 3.3: Side view of the CDF detector.



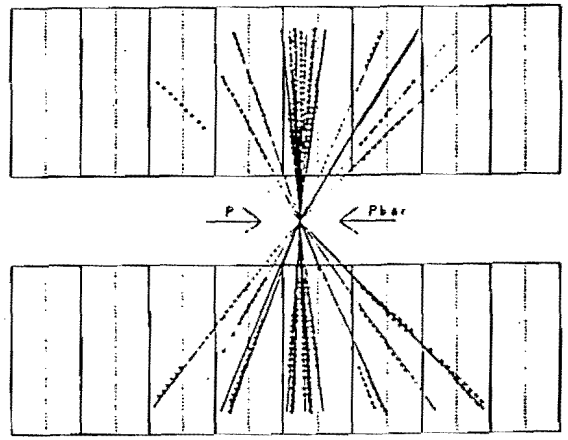


Figure 3.4: The VTPC event display showing wire hits in a typical event.

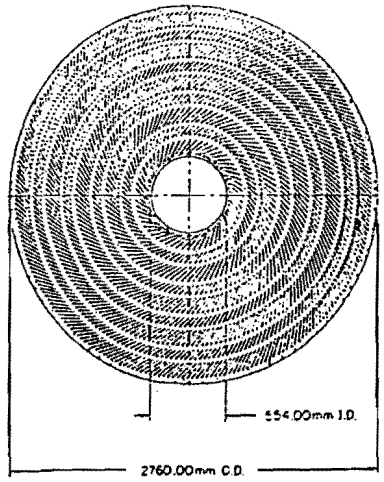


Figure 3.5: The CDF central tracking chamber (end view).

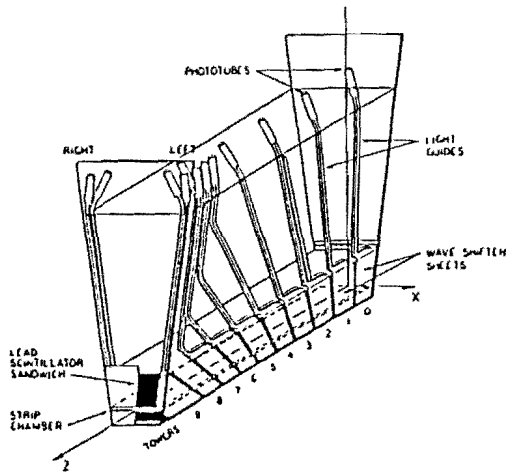


Figure 3.6: A CDF central wedge showing CEM and CHA calorimeters. Also shown are the central strip chambers (CES) and light guidance/collection system.

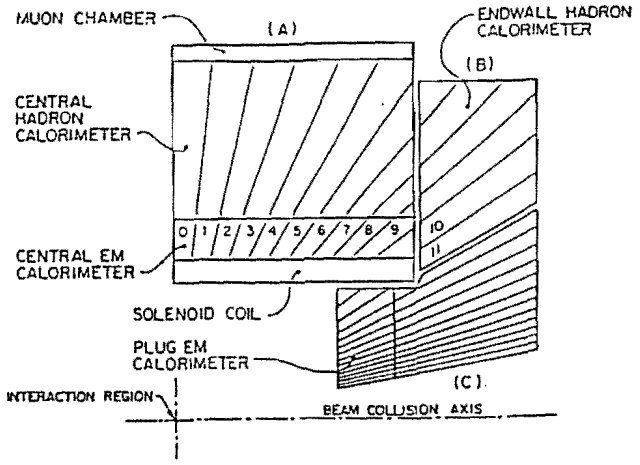


Figure 3.7: Side view of a central wedge showing projective tower geometry.



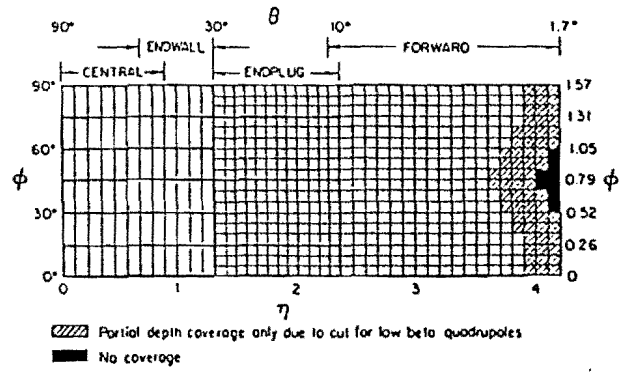


Figure 3.8: Calorimeter segmentation at CDF. Central towers cover 15° × 0.1 in $\phi - \eta$ space. Plug and forward towers are 5° × 0.1. Only 1 of 8 possible quadrants is shown.

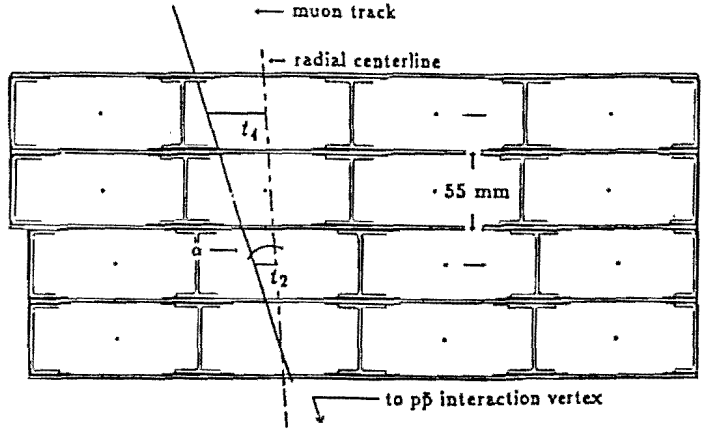


Figure 3.9: CDF central muon chamber geometry, and the path of a muon through the chambers.

# Chapter 4

# Data Acquisition and Offline Event Reconstruction

In this chapter we describe the series of steps we take in going from high-energy proton-antiproton collisions inside the Tevatron to a data set that we can analyze in our search for leptoquark production.

## 4.1 The CDF Trigger System

As discussed in Chapter 3, the proton-antiproton scattering cross section at 1.8 TeV is around 70 mb which gives $\sim 10^5$ interactions per second at typical Tevatron beam luminosities. By far the majority of these events are so-called minimum bias events in which few, if any, high momentum particles emerge at large angles with respect to the beam axis. While much can be learned from such events, we are limited by the rate at which we can acquire data from the detector and record it on magnetic tape ($\sim 1-2$ Hz during the 1988-89 run). Furthermore, we would like to observe other interesting processes such as, for example, high-$E_T$ multijet formation, events containing heavy quarks and/or vector bosons, and new particle production. These processes are much rarer than the minimum bias events. For instance the cross section for the process $\bar{p}p \rightarrow W^{\pm} + X \rightarrow e^{\pm}\nu + X$ at CDF is only around 2.2 nb [57], equivalent to producing only one such event for every 30 million minimum bias interactions. For leptoquarks, the cross section is even smaller. For $M_{LQ} = 45$ GeV we would expect a leptoquark-pair event for every 120 million minimum bias events, while for $M_{LQ} = 125$ GeV the number is just 1 in 30 billion.

By making fast evaluations of the characteristics of an event, the CDF trigger system acts as a filter that allows us to both reduce the effective event rate and



most importantly to ensure that those events which are saved are of interest to us. The trigger used at CDF is a sequential, four-stage decision path, known as Level-0 through Level-3. Events which fail requirements at Level-0 are rejected; those which pass are passed on to Level-1. This continues until an event is either rejected at a higher level or eventually passes Level-3, in which case the event is written to tape. The decisions made at each stage, and the associated timings, assuming a beam luminosity of $\mathcal{L} = 1 \times 10^{30}$ cm$^{-2}$s$^{-1}$, are briefly described in the following subsections.

### 4.1.1 The Level-0 Trigger

The Level-0 trigger is our first indication that an inelastic collision has taken place. It requires a coincidence of hits in two sets of scintillator planes which are located at $z = \pm 591$ cm from the nominal primary interaction point $z_0$. These scintillator planes are known as beam-beam counters (BBC's) and can be seen in the center of Figure 3.3. The scintillators surround the beam pipe and cover the region $3.24 < |\eta| < 5.9$. The coincidence is required to occur within a 15ns window centered on the time at which the proton and anti-proton bunches cross each other within the detector. Requiring hits in both East and West BBC's reduces contributions to the triggered-event rate from beam-gas interactions. These occur when a proton or antiproton in the beam collides with an atom of the residual gas inside the beam pipe. This looks like a fixed target event with many secondaries produced in the forward beam direction, and nothing in the backward region.

Given the geometry of the BBC's and the 15ns window requirement, it has been estimated that the effective cross section of the level-0 trigger is $47 \pm 3$ mb. The corresponding rate at which events are passed to the Level-1 trigger is then around 47 KHz, or 67% of the total inelastic rate. Furthermore, the time between consecutive bunch crossings is 3.5$\mu$s. By requiring that the Level-0 trigger make a decision in a time less than this the trigger is ready for the next beam-crossing should the current event be rejected. If the event does pass the Level-0 trigger, further data taking is inhibited so that the higher level triggers can make their

evaluations.

### 4.1.2 The Level-1 Trigger

The Level-1 trigger decision is based primarily on the characteristics of energy deposition throughout the CDF detector. Fast analog signals from the calorimeters are sent to hardware processors located approximately 200 ft. from the collision hall. The total time taken from the initial interaction to the Level-1 decision should be less than $7\mu s$ so that if the event is rejected all readout systems can be reset in time for the next possible interaction (we have already missed one crossing by going to Level-1).

The Level-1 hardware processors group signals from calorimeter towers into 'trigger towers' of size $0.2\eta \times 15^0\phi$. All trigger towers with energy above a programmable threshold are summed (electromagnetic and hadronic energies are added separately) and the event is passed if it meets one of several criteria. For example, one of the Level-1 triggers, the so called 'jet-20' trigger, requires that the total $E_T$ summed over all trigger towers above a 1-GeV threshold be greater than 20 GeV. The effective cross section of this trigger is around $400\mu$b, or 0.85% of the events considered at Level-1. For the 'Level-1 Central Electron-6' trigger, at least one CEM trigger tower with $E_T(EM) > 6$ GeV is required. The effective cross section is approximately $22\mu$b (0.05% of Level-1 input).

The total Level-1 effective cross section is around 1mb, which means events are passed at a rate of approximately 1 KHz to Level-2.

### 4.1.3 The Level-2 Trigger

The Level-2 trigger continues the event-analysis in a much more sophisticated way. There are many possible ways for an event to pass at Level-2 since there are correspondingly many different physics processes in which we are interested, each with their own individual event characteristics. As an example we will consider the Level-2 trigger most relevant to this analysis, the Level-2 12-GeV Central Electron trigger.



The trigger towers found by Level-1 are passed to an electronic card known as the 'Cluster Finder' which groups trigger towers into local clusters of energy. For each cluster found the $E_T$, the centroid in $\eta - \phi$, and the cluster width are calculated. Again HAD and EM energies are considered separately.

A hardware track-finder known as the Central Fast Tracker (CFT) uses fast-out information from the CTC to find all two dimensional tracks in the $r - \phi$ plane above a preset momentum threshold. The CFT takes on average $2.5\mu s$ to find all high $P_T$ tracks in an event, though this varies with the track multiplicity of the event. The momentum resolution of the CFT is approximately $\Delta P_T/P_T \sim 0.035 P_T$.

For the Level-2 Electron-12 trigger, at least one cluster is required in the Central region ($|\eta| < 1.0$) with both $E_T(\mathrm{EM}) > 12$ GeV and $E_T(\mathrm{HAD})/E_T(\mathrm{EM}) < 12.5\%$. Furthermore, the CFT must find a track with $P_T > 6$ GeV pointing to the cluster. The effective cross section of this trigger is approximately 0.49 $\mu$b, so that only 0.5 events per second pass this trigger and go on to Level-3. The efficiency of this trigger is measured using independently selected electrons. For those near the 12-GeV threshold, an independent trigger with a 7-GeV threshold is used. For higher-$E_T$ electrons the 12-GeV trigger efficiency is studied using $W \rightarrow e\nu$ events selected with a trigger which requires a large missing energy. Using the lower threshold, a 12-GeV trigger efficiency of $\varepsilon = 98.0 \pm 0.5\%$ is found for electrons with $E_T > 15$ GeV. This is found to fall off steeply with decreasing $E_T$ and is less than 50%(10%) for an electron $E_T = 12(10)$ GeV. For $W^{\pm}$ events the electron trigger efficiency is found to be $97.3 \pm 0.5\%$. Further details can be found in [6] and [57]. Given this efficiency, the chance of neither electron triggering the readout system in a central-central dielectron event, for example, is around $(1 - 0.98)^2 < 0.04\%$.

The total effective cross section of the Level-2 trigger is around 3-4 $\mu$b and so events are passed to Level-3 at 3-4 Hz. The Level-2 trigger decision takes approximately 20 $\mu$s, though again this varies widely with the complexity of the event. If the event is accepted, all data from the detector is read and passed to the Level-3 software processors. The total readout time is around 1 ms, after

which the front-end electronics are reset so that data taking may resume, even though a Level-3 decision is still being made.

#### 4.1.4 The Level-3 Trigger

The final stage of the trigger process is Level-3. After the detector is read out the formatted event is passed to one of 60 Motorola 68020 microprocessors executing streamlined versions of CDF offline event reconstruction algorithms written in FORTRAN. Unlike the earlier stages, Level-3 has access to all detector data from an event. Sources of noise in the event are removed, and cluster and track parameters are recalculated. For Central Electrons, Level-3 requires a reconstructed cluster $E_T(EM)$ above the Level-2 threshold and a 6-GeV track pointing to the cluster. As in Level-2, many different algorithms are used in Level-3 so as to be sensitive to many classes of event.

In the 1988-89 run Level-3 rejected approximately 50% of the events it considered, giving a final event-to-tape rate of 1-2 Hz.

Finally, we summarize the rates for the multi-level triggers and for the central electron triggers relevant to this analysis. Note that all rates assume $\mathcal{L} = 1 \times 10^{30}$ cm$^{-2}$s$^{-1}$, and at this luminosity, an effective trigger cross section of 1$\mu$b corresponds to an event rate of 1 Hz.

| Trigger | $\sigma(\mu b)$ | Rejects | Trigger | $\sigma(\mu b)$ | Rejects |
|---|---|---|---|---|---|
| None | $70 \times 10^3$ | N/A | None | $70 \times 10^3$ | N/A |
| Level-0 | $47 \times 10^3$ | 33% | Level-0 | $47 \times 10^3$ | 33% |
| Level-1 | 400 | 99% | L1 Central Ele-06 | 22 | 99.95% |
| Level-2 | $\sim 3.5$ | 99% | L2 Central Ele-12 | 0.49 | 97.8% |
| Level-3 | $\sim 1.75$ | 50% | L3 Central Ele-12 | 0.25 | 50% |

Table 4.1: Cross Sections and Event Rejection Rates for CDF Multi-level and Central Electron Triggers.

For the 1-year run during 1988-89, over 4 million events passed the Level-3 trigger and were recorded on some 5500 magnetic tapes.



### 4.2 Event Reconstruction

Offline analysis of data can be thought of as a two step process.

The first stage is to reconstruct each event. This involves clustering calorimeter energy deposits using full detector segmentation, carefully reconstructing two- and three-dimensional tracks in the CTC, identifying, for example, electrons, photons, muons, and jets in the event, and calculating such global event parameters as the total and missing transverse energy, and the location of the primary interaction point. Much of this was done to a good approximation when making the online Level-3 trigger decision, but the process is now repeated more completely. We will not describe methods of identifying particles such as muons, photons, or taus, for example, but instead discuss only those event reconstruction processes relevant to this thesis namely electron and jet reconstruction, and $\not\!\!E_T$ estimation.

Once all events have been fully reconstructed, the second stage is to form a data subsample containing events whose topology, kinematic characteristics, or particle content are of relevance to the kind of physics process that we are seeking. In this thesis, for example, we will start by requiring events with at least one electron candidate with $E_T > 20$ GeV. This second stage of offline analysis and the exact cuts used in making our inclusive electron data set are the subject of the next section.

#### 4.2.1 Electron Clustering

In identifying electrons or photons in an event, an offline electromagnetic clustering algorithm EMCLST, searches for all towers in the CEM, PEM, and FEM with energy depositions in excess of some threshold, usually $E_T(EM) > 3$ GeV. The tower segmentation used is that of the actual detector, and not the coarser trigger-tower segmentation used in making the online trigger decision. Any EM tower above threshold is known as a 'seed-tower' since clusters are formed around the seed; the 3 GeV cut is then known as the 'seed-threshold'. To form a cluster, EMCLST adds in all adjacent towers whose energy is above an adjustable tower-threshold, usually $E_T(EM) > 0.1$ GeV, but below the energy of the seed-tower.

If any adjacent tower has an $E_T(EM)$ greater than that of the current seed tower, the clustering process is stopped, then restarted using the higher energy tower as the seed. EMCLST limits the size of electromagnetic clusters as shown in the following table, and depicted in Figure 4.1.

| Detector | Cluster Size ($\eta$) | Cluster Size ($\phi$) |
|---|---|---|
| CEM | Seed $\pm 1$ Tower | Seed $\pm 0$ Towers |
| PEM | Seed $\pm 2$ Towers | Seed $\pm 2$ Towers |
| FEM | Seed $\pm 3$ Towers | Seed $\pm 3$ Towers |

Table 4.2: Default Electromagnetic Cluster Size in the EMCLST Clustering Algorithm.

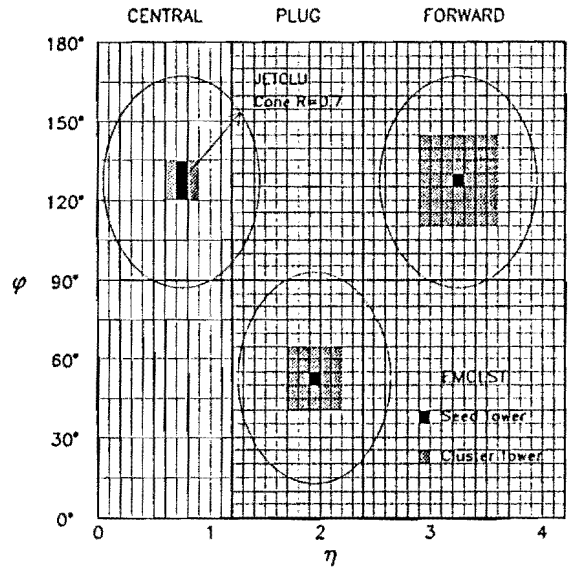


Figure 4.1: Maximum Cluster Sizes in Central, Plug,and Forward Calorimeters for EMCLST and JETCLU Clustering Algorithms. Area Shown Represents 1/4 of Total CDF Calorimetry.



Analysis of energy deposition patterns obtained at the CDF testbeam using electrons of energies in the range 10-150 GeV show that isolated electrons should be well contained within the maximum cluster sizes shown in Table 4.2. Therefore, one motivation for imposing a cluster size limit is that in doing so we avoid identifying broad jets with unusually high electromagnetic fraction as a possible electron/photon candidate. Jets in CDF events are common; isolated high $E_T$ electrons and photons are relatively rare.

EMCLST continues clustering until either no further towers are found above threshold, or if the cluster size exceeds the limits shown above. After all EM clusters have been found, those which fail the cluster $E_T$ cut $E_T(EM) > 5$ GeV are removed. Since we are trying to find EM clusters the final test is to sum the hadronic energy for all towers in the cluster and compare it to the EM energy. Only those clusters with $E_T(\mathrm{HAD})/E_T(\mathrm{EM}) < 12.5\%$ are retained.

### 4.2.2 Jet Clustering

The basic philosophy behind the CDF jet clustering algorithm JETCLU is very similar to that already outlined in the preceding section for EMCLST. For JETCLU we obviously do not impose a HAD/EM cut on the cluster, but seed towers are formed as before and neighbours are added to the cluster if above threshold. The JETCLU seed tower threshold is $E_T(TOT) > 1$ GeV while the cluster tower threshold is $E_T(TOT) > 0.1$ GeV. As for EMCLST, the jet clusters are limited in extent, but the JETCLU definition of cluster size is in terms of a cone radius rather than a seed $\pm$ n-towers. For this analysis all jets are clustered using a cone size $R = \sqrt{\Delta\eta^2 + \Delta\phi^2} = 0.7$, defined from the $E_T$-weighted jet centroid. While this is the default cone size, other choices are sometimes used such as $R = 0.4$ or $R = 1.0$. In Figure 4.1 we also show the $R = 0.7$ JETCLU clustering cones in three different detector regions and compare them to the corresponding EMCLST cluster size limits.

The algorithm used in JETCLU is by no means the only choice of how to form jet clusters, but seems to avoid many of the pathologies associated with other

algorithms. A detailed comparison of algorithms tested at CDF can be found in [61], while a more complete description of JETCLU, including centroid definition and tests of the clustering algorithm, is given in [60].

### 4.2.3 Missing $E_T$ Calculation

At the Tevatron, the initial state proton-antiproton system has zero net momentum. Therefore in any event containing N final state particles, momentum conservation requires that

$$\sum_{i=1}^{N} \vec{P}_i = 0 \tag{4.1}$$

In the approximation where all N particles are massless, this becomes a sum over vector-energies

$$\sum_{i=1}^{N} \vec{E}_i = 0 \tag{4.2}$$

where $\vec{E}_i = E_i \cdot \hat{n}_i$, and $\hat{n}_i$ is the unit vector pointing in the direction of the particle momentum. We work in this massless approximation since CDF calorimeters measure energy deposition. The Central Tracking Chamber can be used to measure particle momenta but the $\eta$ coverage is limited and, unlike the calorimeters, the CTC is limited to measuring charged particles.

It is not possible to completely measure all final state energies in an event using the CDF calorimeters. There are several holes and cracks which arise naturally whenever one constructs a segmented detector. More important is the fact that the CDF calorimeters do not cover the large-$\eta$ region, particularly the region within the beam-pipe. This is unfortunate since this is where most of the final state particles and event energy is to be found.

In order to be able to make statements about energy flow in an event, we restrict ourselves to the transverse ($r - \phi$) plane. The corresponding energy balance relation is then

$$\sum_{i=1}^{N} \vec{E}_{Ti} = 0 \tag{4.3}$$

Final state particles travelling down the beam pipe, and hence which are lost to our calorimeters, have little or no transverse energy. Equation 4.3 will then



usually be a good approximation.

In the case where this relation is not satisfied, we have a transverse energy imbalance, and we then define the missing transverse energy as

$$\text{missing} - E_T = -\sum_{i=1}^{N} \vec{E}_{Ti} \tag{4.4}$$

Sources of $\not\!\!E_T$ which are of interest are events that contain particles which deposit little or no energy in the calorimeters. In the Standard Model, such particles include muons and neutrinos, but more exotic particles which are also expected to give events with large $\not\!\!E_T$ signatures include, for example, the photino predicted by supersymmetry. Muons produced in the central rapidity region can be identified by the presence of a track which points to hits in the central muon chambers, as well as a small energy deposit in the corresponding calorimeter tower. For neutrinos there is no such track, no muon chamber signal, and no calorimeter energy deposit. One of the two analyses presented in this thesis makes extensive use of the $\not\!\!E_T$ signature due to the expected presence of a high energy neutrino in the event.

Other common sources of $\not\!\!E_T$ include events in which a high-$E_T$ particle has been lost down a calorimeter crack. If the particle is charged and in the central region, then we can correct our $\not\!\!E_T$ estimate by using the track momentum. If the particle is neutral, for example a pion or photon, then there is little we can do. Jets often contain many neutral particles and it is relatively easy for some of these to be lost. Jet energy corrections attempt, amongst other things, to rectify this problem by adding in energy if part of the jet overlaps calorimeter cracks. After such corrections are made, the $\not\!\!E_T$ is re-calculated and is often found to be far less significant. A detailed explanation of this and other lesser $\not\!\!E_T$ corrections can be found in [62].

# Chapter 5

# The Inclusive Electron Data Set

## 5.1 Introduction

Having described the first stage of offline analysis, namely event reconstruction, we now turn our attention to creating a subset of the data which contains events of relevance to our leptoquark search.

In the first of the two analyses presented in this thesis (Chapter 6) we assume that a pair of leptoquarks has been produced, and that each has then decayed to an $e + u$ pair. We consider leptoquarks in the range $M_{LQ} = 45 - 125$ GeV, and at these masses we typically expect the decay products to be well separated from each other. The signature for such events is then the observation of two isolated, high-$E_T$, and oppositely charged electrons and the presence of two high-$E_T$ jets. More quantitative statements on leptoquark decay kinematics will be given in the next chapter, but for now it is sufficient to state that the electron and jet $E_T$ spectra peak at $\sim M_{LQ}/2$. Given the range of leptoquark masses that we consider, we can therefore reasonably expect events containing electrons and jets having $< E_T >$ in the range $20 - 65$ GeV.

In the second analysis (Chapter 7) we again consider the production of an $\overline{LQ}LQ$ pair, but then assume one leptoquark decays to $u + e$ and the other to $d + \nu_e$. Events of this type would then be signalled by observation of a high-$E_T$ electron, substantial missing transverse energy, and again the presence of two high-$E_T$ jets.

In both of the decay channels considered in this thesis we therefore expect at least one high-$E_T$ electron and two high-$E_T$ jets. Since jets are far more common in the CDF data than are electrons (see Section 4.2.1), we take the approach



of building an inclusive electron data set and *then* looking for two or more jets, rather than the converse process where we would be searching for electrons in the myriad of multijet events recorded during the run.

Before actually making our electron data set it is instructive to consider in which CDF detector region, if any, we would be most likely to observe electrons from leptoquark decay. If we consider just one of the leptoquarks and assume it decays via $LQ \rightarrow u + e$ then we estimate from Monte Carlo simulated events that the electron should be produced in the central region of the detector approximately 70%(80%) of the time for $M_{LQ} = 45(125)$ GeV. For the dielectron+dijet channel, the chance of observing at least one electron in the central region is then around 90%(96%). This is fortuitous since electrons are, in general, measured very well in the central detector.

Given then that both channels contain at least one electron, and that this will be produced with high probability in the central region, we begin our analysis with an inclusive central electron data set. The remainder of this chapter is devoted to the discussion of how this data set is made.

The starting point is the set of reconstructed events, described in the previous chapter, which are known to have passed the level-2 central electron trigger. These will now be subjected to more stringent requirements to try to ensure that they do indeed contain a high-$E_T$ electron and as such we will focus almost exclusively on the electromagnetic clusters in the events.

## 5.2 Kinematic Cuts

The first requirement that we make of any central electron candidate is that it has a transverse energy cluster with $E_T > 20$ GeV. We expect, on average, electrons from leptoquark decay to pass this cut, the efficiency improving at higher leptoquark masses. However, because of various detector effects the true electron energy and the energy which we measure are often not the same quantity, although the agreement is usually within $\pm 5\%$. In making the inclusive electron data set we first correct the electron energies before applying our $E_T$ cut.

### 5.2.1 Central-Electron Energy Corrections

In correcting the measured energy of a central electron we consider

- Tower-to-Tower variations in response
- Overall CEM calorimeter energy scale
- Detector response variations with position within a single CEM tower

The first correction accounts for tower-to-tower variations in calorimeter response to electrons of the same energy. This is done using a sample of $\sim$ 17000 central electrons recorded during the collider run and which are distributed throughout the CEM. For all the electrons found within a given calorimeter tower the $E/P$ distribution is formed, where $E/P$ is the ratio of the measured CEM energy $E$ to the momentum $P$ as determined by the CTC. By comparing the means of the $E/P$ distributions, relative correction factors are obtained for the individual towers. The spread in the size of the corrections needed is on the order of $\pm 3\%$.

The second correction sets an absolute energy scale for the CEM calorimeter. To first order, this determined at the CDF testbeam using electrons of known energy. However, since the momentum scale of the CDF central tracking chamber (CTC) has been determined very precisely ($\pm 0.05\%$) from a mapping of the magnetic field within the solenoid, and since we expect the energy-momentum ratio $E/P$ to be $\simeq 1$, the CEM scale can be recalibrated to that of the CTC. This is done at the collider using a sample of around 1800 high-$E_T$ central electrons coming from probable $W^{\pm} \rightarrow e\nu_e$ decays. One subtlety that has to be accounted for is that before reaching the CEM calorimeter the electron can radiate bremsstrahlung photons. The CEM calorimeter will measure the total energy of the electron and radiated photons, providing a reasonable estimate of the original energy of the electron. However, the electron momentum as determined by the CTC track is somewhat underestimated. The net effect is that the mean of the $E/P$ distribution is shifted to slightly higher than $E/P = 1$, the actual value being determined by detailed Monte Carlo simulations. Once the expected $< E/P >$ has been determined, the energy scale can be calibrated to the momentum scale accordingly.



The magnitude of this rescaling is of order $+1.7\%$.

The CTC scale is checked using muon tracks from $\Upsilon \rightarrow \mu^+\mu^-$ and $J/\psi \rightarrow \mu^+\mu^-$ decays. The reconstructed meson masses are $9.469 \pm 0.010$ GeV and $3.097 \pm 0.001$ GeV respectively. The $\Upsilon$ mass agrees to within 0.1% of the world average mass, while the CDF $J/\Psi$ mass agrees to within 0.03%. Combining all systematic errors in quadrature, the total uncertainty in the CTC momentum scale is estimated to be 0.11%.

Finally a correction is applied which accounts for variations in calorimeter response from different regions of a single CEM projective tower. At the CDF testbeam it was found that this response varies by around $\pm 5\%$, depending on exactly where an electron passes through the tower. A response map is obtained by scanning the inner face of a calorimeter wedge in both $\eta$ and $\phi$ directions using a beam of electrons of known energy. The beam position is determined using strip chamber information to locate the resulting electromagnetic shower within the tower. The response map obtained in this way is shown in Figure 5.1 and using it we can apply a position-dependent correction when estimating the energy of a CEM electron in collider events.

The overall effect of the corrections we have described is that the energy of an electron in an event can change by $\mathcal{O}(5\%)$, and neglecting them would have only a small effect on leptoquark event acceptance. However, for this analysis we will apply electron (and jet) energy corrections since one of the quantities we will later consider is the electron-jet invariant mass spectrum, an unexpected peak in which is possibly a signal for leptoquark decay. In the event of small event statistics, any improvement in reconstructed mass resolution is useful. Electron energy corrections are also very important when attempting, for example, a precision measurement of the mass of the $Z^0$ boson using the decay $Z^0 \rightarrow e^+e^-$. A much more detailed account of the electron energy corrections can therefore be found in [63].

### 5.3 Isolation Requirements

The isolation of an electron candidate is defined as follows:

$$\mathrm{ISO}_4 = \frac{E_T(R=0.4) - E_T(\mathrm{Ele})}{E_T(R=0.4)} \tag{5.1}$$

$E_T(R = 0.4)$ is defined to be the total electromagnetic energy within a cone of $R = 0.4$ centered on the electromagnetic cluster (recall $R = \sqrt{\Delta\eta^2 + \Delta\phi^2}$). The quantity $E_T(\mathrm{Ele})$ is simply the electromagnetic transverse energy of the cluster. If all the energy within the cone is equal to that found for the cluster, then we would have the ideal case of zero isolation for the electron.

On average, we expect the electrons from leptoquark decay to be well separated from other particles in the event, resulting in relatively small values of the electron isolation. Other sources of high-$E_T$ electrons, real or fake, can contaminate (perhaps even completely populate) our data sample and an isolation cut can prove very useful in removing such events. A good example which illustrates this is provided by events which contain one or more high-$E_T$ b-quarks which have decayed semileptonically via $b \rightarrow ce\nu_e$. The differential cross section for inclusive b-production $d\sigma/dP_T$ falls steeply but is still large enough that we can expect a non-negligible number of decays to give electrons with $E_T > 10$ GeV. However, unlike leptoquark decays, we find that the electron from such b-decays tends to emerge very close or even within the associated c-quark jet. In fact as the b-quark (and hence electron) $P_T$ increases, the electron isolation decreases, making an isolation cut even more efficient. Throughout this thesis a cut of $\mathrm{ISO}_4 < 0.1$ is imposed.

### 5.4 Electron Quality Cuts

Quality cuts are designed to distinguish real electrons from other sources of electromagnetic clusters in an event. These include, for example, isolated photons and those from the decay $\pi^0 \rightarrow 2\gamma$, or single charged pions which form a track in the CTC but which sometimes leave little or no energy in the hadronic calorimeters.



Application of the cuts described so far ensures only that events in our sample contain at least one high energy electromagnetic (HAD/EM< 12.5%) cluster somewhere in the detector, whose energy we are reasonably sure of, and which is well isolated from other electromagnetic calorimeter activity. This may, or may not, be the same cluster which passed the Level-2 Central-Electron trigger discussed in Section 4.1.3 (CEM cluster, $E_T > 12$ GeV, at least one associated track with $P_T > 6$ GeV, and HAD/EM< 12.5%). In building our high-$E_T$ isolated central electron data set we therefore re-examine the set of all clusters in an event which pass the $E_T$ and isolation cuts. We now explicitly require at least one of these clusters to be in the central detector region and that it has an associated track. Furthermore we apply further 'quality' cuts to ensure that in several important respects the candidate EM object is consistent with being an electron. These quality cuts are now described.

#### 5.4.1 Central Region Cuts

1. $E/P < 1.5$

   We require at least one reconstructed CTC track pointing to the EM cluster with $E/P < 1.5$. Since we already require $E_T > 20$ GeV this is equivalent to a cut of $P_T > 13.3$ GeV. Removing objects with high $E/P$ reduces contamination from EM clusters formed when, for example, a high-$P_T$ $\pi^0$ overlaps a low-$P_T$ $\pi^\pm$.

2. Strip-Track Match Cuts: $\Delta r\phi < 1.5$cm, $\Delta z < 3.0$cm

   Any track pointing to the cluster being considered, and which satisfies the $P_T$ cut, is then extrapolated to the CEM strip chambers (CES) which are located at the position of maximum longitudinal shower development within the calorimeter. For a real electron we expect that the CES position of the shower and the extrapolated track position at the chambers should match. In practice we find that the strip-track matching for 50 GeV electrons is of order $\pm 3$ mm $/ \sin\theta$ in the z-direction, and around $\pm 2$ mm in the $r - \phi$ direction. In making the data set we require $\Delta r\phi < 1.5$cm and $\Delta z < 3.0$cm.

The efficiency of these cuts was determined using a sample of W-decay electrons and they were found to have acceptances 97% and 98% respectively [57].

3. $\chi^2$(strips)< 15

   The $\chi^2$(strips) variable, while not a true $\chi^2$, is a statistical measure of the deviation of the EM shower shape, as determined using the strip chambers, from that found for testbeam electrons of similar energy. We impose a cut of $\chi^2 < 15$.

4. LSHR< 0.2

   A quantity commonly used at CDF in electron identification is the lateral energy sharing variable, LSHR. This is simply a measure of the lateral spread of the electromagnetic shower in the calorimeter. Testbeam studies show that the energy deposited by an electron in the CEM is usually well contained within a single tower, while for jets of particles we expect a much broader lateral shower profile.For any electron candidate we compare energy deposition in the cluster seed-tower (i.e. the tower containing the most energy) with that in the two towers adjacent in $\eta$. This gives a lateral 3-tower energy sharing profile which is compared to average profiles obtained for electrons under test-beam conditions. The LSHR variable quantifies the difference in measured and expected profiles and is defined as follows

$$\mathrm{LSHR} = 0.14 \sum_{i=1}^{2} \frac{E_i^{adj} - E_i^{exp}}{\sqrt{0.14^2 E + (\Delta E_i^{exp})^2}} \qquad (5.2)$$

   Here $E_i^{adj(exp)}$ is the observed(expected) energy in the adjacent tower, $E$ is the cluster energy, and $\Delta E$ is the uncertainty in $E_i^{exp}$ assuming a $\pm$1cm error in the shower location within the tower. In this thesis we require a cut of LSHR< 0.2.

5. HAD/EM< $5.5\% + 4.5\% E/100$

   In order to be considered an electromagnetic cluster, the clustering algorithm EMCLST requires that HAD/EM< 12.5%. This is a fairly liberal cut



since central electron showers are normally confined to the CEM calorimeter alone, with little or no energy deposited in the CHA. We therefore expect much lower values of HAD/EM than are required by EMCLST. As the electron energy increases however, the longitudinal size of the electromagnetic shower increases and there is inevitable leakage into the CHA, increasing the measured HAD/EM fraction of the electron. We therefore impose an energy dependent HAD/EM cut of the form given above. This is a much more restrictive cut at low electron energies than the straight < 12.5% requirement, yet allows for energy deposition in the CHA at higher energies. With this form of cut we can remove many clusters which are simply relatively low energy pions, while at the same time retaining our efficiency at observing the high-$E_T$ electrons which can signal new physics.

## 5.5 Z-Vertex Cut

The final cut we apply in making the inclusive central electron data set is not one restricted to electromagnetic clusters, but is rather a cut on a global event variable: the z-vertex position. In Chapter 3 it was stated that the position of the primary-interaction point within the CDF detector has a Gaussian distribution in the z-direction (i.e. along the beam pipe) with mean 0.0 cm and a spread of $\sigma \sim 35.0$ cm. The $z_v$ cut requires the event-vertex in any event be located within $z = \pm 60$ cm of the nominal interaction point. This corresponds to approximately a $2\sigma$ spread of allowed z-vertices which means that around 95% of events pass this cut.

The main reason we impose this cut stems from the projective tower geometry of the calorimeters. For events containing a primary vertex with a large displacement from $z_v = 0$, it is possible for particles to deposit energy in several different calorimeter towers, instead of just one. This is undesirable since it can artificially distort the profile of calorimeter clusters, the cluster isolation, and even our estimates of $E_T$ and missing-$E_T$. Furthermore at large values of $z_v$ the VTPC may no longer be fully efficient in reconstructing tracks emanating from the primary

vertex.

## 5.6 A Summary of the Inclusive Central Electron Data Set

Central Electron Data Set

- CEM Electron Cluster
- Corrected $E_T > 20$ GeV
- Iso($R = 0.4$) $< 0.1$
- $E/P < 1.5$
- Strip-Track Match $\Delta r\phi < 1.5$cm
- Strip-Track Match $\Delta z < 3.0$cm
- $\chi^2$(strips)$< 15$
- LSHR$< 0.2$
- HAD/EM$< 5.5\% + 4.5\% E/100$

This concludes the description of how the inclusive central electron data set is made. After all cuts are applied we find 4997 events, which corresponds to an integrated luminosity of $\int \mathcal{L} = 4.05 \pm 0.28$ pb$^{-1}$. This data set is common to both of the analyses which will be presented in Chapter 6 and 7 respectively. Further requirements tailored to the signatures in the individual channels will be imposed at that time.

## 5.7 Other Electron Cuts

There are further electron cuts which can, and will, be applied in one or both of the analyses that follow this chapter. Though they are not necessary in making the inclusive electron data set, we describe them here as this is both a convenient and natural place to do so.



### 5.7.1 The Fiducial-Region

In both analyses we will impose an additional requirement that ensures that the energy of any electron has been reliably measured. This involves checking that the EM shower is not too close to the various cracks and detector boundaries inherent in any segmented calorimeter. The region of the CDF calorimeters that is considered reliable in terms of electron energy response is known as the 'fiducial' volume. For example, if the cluster seed tower is located adjacent to a crack, it is likely that some, perhaps even most, of the original energy of the electron was lost down it.

Cracks and detector boundaries represent by far the majority of calorimeter volume excluded by fiducial cuts. In addition, however, we remove 3 dead towers in the PEM calorimeter, regions which do not have full hadronic calorimeter coverage, and several modified towers in the so-called chimney module, a CEM wedge through which cooling pipes access the CTC solenoid.

The exact details of the fiducial cuts have been given in several places, for example [57],[64],and [65], and we will not reproduce them here. We do indicate, however, the extent of the fiducial and excluded regions throughout the CDF detector. This is shown in Figure 5.2 in the form of accepted/excluded regions in $\eta - \phi$ space, and is taken from [65].

### 5.7.2 Electron Quality Cuts in the Plug and Forward Regions

In Chapter 6 we will search for events containing a second electron candidate anywhere in the detector, and will impose corresponding detector-specific electron quality cuts on it. These are as follows

Plug Electrons

- PEM Electron Cluster
- HAD/EM$< 5\%$
- $\chi^2_{3\times3} < 15.0$

- VTPC Occupancy > 0.5

The first requirement we make of a plug region electromagnetic cluster is that it satisfies HAD/EM< 5%. The remaining quality cuts are specific to the PEM, and are as follows

1. $\chi^2_{3\times3} < 15.0$

   Like the CES strip-$\chi^2$, the plug $\chi^2_{3\times3}$ variable is a statistical measure of the lateral shower shape, and uses the energy deposition in the eight towers surrounding the cluster seed-tower. The observed shower profile is compared to parameterizations obtained for electrons of similar energy at the CDF testbeam.

2. VTPC Occupancy > 0.5

   In the plug region our ability to distinguish electrons from photons and other neutral particles is somewhat diminished since we can no longer reliably reconstruct an electron track in the central tracking chamber. At the lower end of the plug-$\eta$ range (typically $1 < |\eta| < 1.7$) track reconstruction is often possible since the electron passes though at least some of the CTC wire layers. However at larger values of $\eta$ we are forced to look at the VTPC for indications of a charged track emerging from the primary vertex and pointing to the plug cluster. The VTPC occupancy is simply the ratio of the number of VTPC wires which register hits to the total number of wires on the path from the primary vertex to the plug cluster position. A VTPC occupancy of around 1 indicates a charged track, while an occupancy of zero indicates a likely photon or $\pi^0$ candidate.

We now consider the cuts which are imposed on any second electromagnetic cluster located in the forward region.

Forward Electrons

- FEM Electron Cluster



- HAD/EM< 5%

The only electron quality cut imposed on FEM electrons is a HAD/EM restriction, and as in the case of plug electrons we require HAD/EM< 5%. Other cuts which include isolation, fiducial, and kinematic requirements are discussed during the presentation of each analysis.

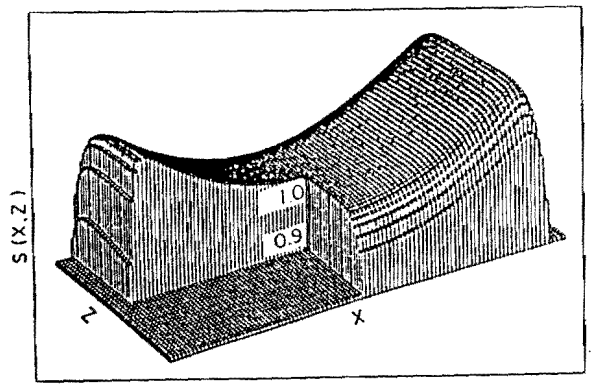


Figure 5.1: Relative response of a CEM calorimeter tower as a function of position.

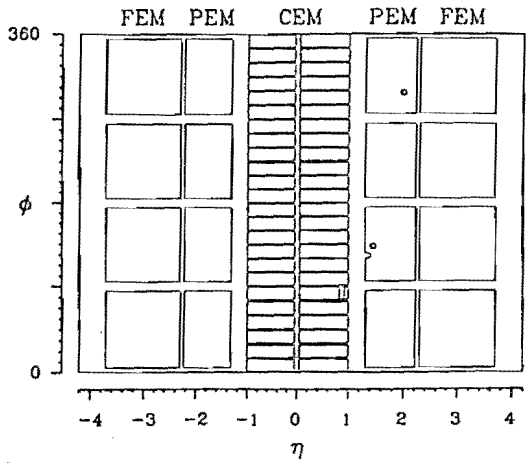


Figure 5.2: Fiducial and excluded regions of the CDF eletromagnetic calorimetry.



# Chapter 6

# A Search for Leptoquarks in the $e^+e^-$+Dijet Channel

## 6.1 Overview Of The Analysis

We now describe a search for evidence of the process

$$\bar{p}p \longrightarrow LQ_1\overline{LQ}_1 + X \longrightarrow (e^+\bar{u})(e^-u) + X \tag{6.1}$$

using the 1988-89 CDF data set. In this section, we will present a brief outline of the steps taken in the analysis and of the contents of the chapter.

We start our analysis in Section 6.2 by examining the features of leptoquark pair production. We make estimates of the pair-production cross section using a Monte Carlo which is based on leading order QCD matrix elements. We also consider the effects of including 'K-factors' arising from higher-order corrections.

This is followed in Section 6.3 by a discussion of leptoquark decays, in particular the kinematic properties of the resulting electrons and quarks; this will guide us when we later make cuts to reduce contributions from background processes. Also included is a section on the possibility of observing a leptoquark signal through an unexpected peak in the electron-jet mass spectrum.

Having outlined our expectations for leptoquark pair events, we next turn to those Standard Model sources of background which can fake the signal. Each of these is discussed in turn in Section 6.5, and we present appropriate cuts to reduce their contributions.

In Section 6.6 we give the total number of expected signal events and summarize the acceptances of the various cuts we impose.

Section 6.7 presents our analysis of the CDF data. Final results which take into account statistical and systematic uncertainties are given in Section 6.8.

## 6.2 Leptoquark Production Cross Section

The mechanisms whereby pairs of leptoquarks can be produced at hadron colliders were presented in Chapter 2. In this section we will estimate the cross section $\sigma_{LQ}$ for such events at $\sqrt{s} = 1.8$ TeV since this can be used to estimate the expected number of events produced as a function of leptoquark mass. When we later examine the CDF data, these predictions, along with corresponding ones for Standard Model backgrounds, can help to determine which processes, if any, are compatible with our observations.

For a quantitative estimate of $\sigma_{LQ}$ we rely, in the absence of a theoretical prediction, upon the ISAJET Monte Carlo (MC) event generator [29]. As a cross-check, the results obtained are compared to independent estimates for the pair production of color-triplet techni-pions [30]. These particles, which were discussed in Section 2.1.2, should be identical in terms of their pair production to leptoquarks of the type considered here. The techni-pion and leptoquark Monte Carlo results are found to be in reasonable agreement.

If no signal is observed then our analysis becomes essentially an independent *measurement* of the leptoquark production cross section $\sigma(M_{LQ}) \cdot x^2$, with no Monte Carlo dependence. However, if we wish to decouple our measurement and give separate limits on any one of $\sigma$, $M_{LQ}$, or $x$, then it is necessary to assume values for the other two. In particular separate mass and branching ratio limits rely upon our MC estimates for the production cross section. Fortunately such limits are easily re-estimated should a new cross section become favored at some point in the future.

Having presented in this prologue the reasons for our interest in the cross section, we now turn to the means of its estimation.

### 6.2.1 Leading Order Predictions

ISAJET is a Monte Carlo event generator. By this we mean that it produces random simulated $\bar{p}p$-collision events at a specified beam energy in one of several classes of parton level subprocesses. 'Monte Carlo' refers to the fact that after



generation, an event is accepted or rejected based on the throw of an electronic die.

To be more specific, ISAJET first calculates a parton-level cross section $\hat{\sigma}$, the magnitude of which depends on both initial and final state particle momenta, and which is based on leading order perturbative QCD matrix elements. Since initial parton states are not all equally likely, ISAJET convolutes $\hat{\sigma}$ with parton structure functions evaluated at an energy scale $Q$ which is given by

$$Q^2 = \frac{2\hat{s}\hat{t}\hat{u}}{\hat{s}^2 + \hat{t}^2 + \hat{u}^2} \tag{6.2}$$

where $\hat{s}, \hat{t}$, and $\hat{u}$ are the usual kinematic invariants for the sub-process. We note that this expression for $Q^2$ is only one of several reasonable guesses at its form, just as there are currently many parameterizations of the parton structure functions, each leading to somewhat different cross section predictions and final event topologies. For structure functions in this analysis we use the widely accepted Set B of Harriman, Martin, Roberts, and Stirling [31] which assumes a QCD scale of $\Lambda_{QCD} = 190$ MeV, and which we refer to from here on as 'HMRSB-190'. At the end of this chapter we will we show how our final results are affected by different choices of parton distribution functions and $Q^2$ scale.

Finally, after a hard parton-scattering has been generated at leading order, the effects of higher-order corrections to the parton level subprocess are included in ISAJET by adding in initial and final state radiation processes. With this complete, the total cross section $\sigma$ for the event is calculated.

After the event generation and cross-section calculation, the next step is to accept or reject the event depending on whether or not the event cross section $\sigma_{\text{Event}}$ satisfies

$$\sigma_{\text{Event}} > \epsilon \cdot \sigma_{\text{MAX}} \tag{6.3}$$

Here $\epsilon$ is a random number generated uniformly on the interval $0 - 1$, and $\sigma_{\text{MAX}}$ is an upper-limit on the process cross section based on user-defined cuts on quantities such as jet transverse momenta. By selecting events in this way, event configurations are generated with a frequency proportional to their likelihood of

being produced in real collisions. The cross section reported by ISAJET for the process of interest is then just the average of the cross sections for all accepted events. This estimate clearly becomes statistically more reliable as we increase the number of events generated.

For this analysis we use version 6.36 of ISAJET to generate events containing pairs of supersymmetric quarks of a specified mass in the final state. Like leptoquarks, squarks are massive colored scalars and so should be almost identical to leptoquarks in terms of their pair production cross section. We say 'almost' identical since supersymmetric-gluon (gluino) exchange in the $\hat{t}$-channel can lead to squark-pair production. In ISAJET these and any other subprocesses involving gluinos are suppressed by setting $m_{\tilde{g}} = \infty$. Supersymmetric quarks can be produced in either of two mass-degenerate chiral states, denoted $\tilde{q}_L$ and $\tilde{q}_R$. To recover a non-degenerate scalar-pair production cross section we therefore need to divide the ISAJET prediction by a factor of 2. Having done this, any distinction between squarks and leptoquarks in terms of production is lost and for the rest of this analysis we refer to the ISAJET squarks simply as leptoquarks.

For the purpose of cross section estimation only, we generate 25000 events for several masses in the range $45 < M_{LQ} < 145$ GeV while the leptoquark transverse momentum is constrained to lie in the range 1 GeV $< P_T(LQ) <$ 300 GeV for most values of $M_{LQ}$. The results obtained using HMRS-B structure functions are shown in Table 6.1 and in Figure 6.1. Also shown in the figure is the effect of higher-order corrections to the leading cross section, these being the subject of the next section. Note that results in both the table and figure have been corrected for the supersymmetry L,R factor of 2 as described above, and therefore represent our best estimation of the leptoquark cross section.

| $M_{LQ}$ (GeV) | 45 | 55 | 65 | 75 | 85 | 105 | 125 | 145 |
|---|---|---|---|---|---|---|---|---|
| $\sigma$(pb) | 595.5 | 222.3 | 94.5 | 44.3 | 22.5 | 6.95 | 2.54 | 1.07 |

Table 6.1: ISAJET Leptoquark Pair Production Cross Section as a Function of Leptoquark Mass.



### 6.2.2 Higher-Order Corrections

Montigny and Marleau have calculated the effect of soft gluon corrections to the leading order leptoquark production cross section at hadron colliders [37, 38]. They consider both single and pair production, and in each case give separate corrections to $q\bar{q}$ annihilation and $gg$ fusion subprocesses. These corrections, or K-Factors, are similar to the celebrated Drell-Yan K-factor which arises when considering higher-order effects in the process $q\bar{q} \rightarrow e^+e^-$. Unlike the case of Drell-Yan process however, leptoquark production involves two different K-factors depending on whether $q\bar{q}$ or $gg$ pairs were the initial state partons making the hard collision. Specifically, the authors conclude that the $q\bar{q}$ processes are slightly suppressed while the $gg$ processes can be significantly enhanced. In an obvious notation, the K-factors that arise are as follows:

$$K_{gg} = 1 + \alpha_s \frac{2\pi}{3} \qquad \& \qquad K_{q\bar{q}} = 1 - \alpha_s \frac{\pi}{6} \tag{6.4}$$

If the series of higher-order corrections forms a convergent exponential series, and the authors cite evidence for this, then the K-factors become

$$K_{gg} = \exp(\alpha_s \frac{2\pi}{3}) \qquad \& \qquad K_{q\bar{q}} = \exp(-\alpha_s \frac{\pi}{6}) \tag{6.5}$$

At low leptoquark masses we expect $gg$ fusion to be the dominant production process due to the dominance of the gluon structure function at low x. Since $K_{gg} > 1$ and $K_{q\bar{q}} < 1$ we would therefore expect the greatest positive correction to the leptoquark cross section at the lowest masses of interest.

As we move to higher leptoquark masses the average momentum of the parent partons must also increase and we expect $q\bar{q}$ annihilation to become competitive, decreasing the fraction of gluon-gluon fusion events. The strong coupling $\alpha_s$ also decreases with $M_{LQ}$ and both of these effects combine to reduce the size of the higher-order correction. Numerical values for the K-factors in [38] assume $\alpha_s = 0.3$. while in this thesis we derive values for the effective K-factors with $\alpha_s(Q^2)$ evaluated at some appropriate momentum scale, $Q$. The results are shown in the following table:

| $M_{LQ}$(GeV) | $N_{gg}$ (%) | $N_{q\bar{q}}$ (%) | $\alpha_s$ | $K_{E\not{H}}$ | $K_{E\not{H}}(Exp)$ |
|---|---|---|---|---|---|
| 45 | 92.7 | 7.3 | 0.134 | 1.26 | 1.30 |
| 65 | 86.2 | 13.8 | 0.126 | 1.23 | 1.26 |
| 85 | 75.0 | 25.0 | 0.121 | 1.18 | 1.21 |
| 105 | 68.2 | 31.8 | 0.117 | 1.14 | 1.17 |
| 125 | 54.0 | 46.0 | 0.114 | 1.09 | 1.11 |
| 150 | 44.7 | 55.3 | 0.111 | 1.05 | 1.07 |
| 175 | 35.9 | 64.1 | 0.109 | 1.03 | 1.04 |
| 200 | 27.6 | 72.4 | 0.108 | 1.00 | 1.01 |

Table 6.2: Relative Contributions of $gg$ and $q\bar{q}$ Subprocess to Leptoquark Pair Production and the Associated Soft-Gluon Correction Factor. Both 1-term and Exponentiated K-factors are Shown.

In Figure 6.1 we show the effect of scaling the leading order cross sections from Table 6.1 by the K-factors given in the above table.

To evaluate $\alpha_s(Q^2)$ we use the algorithm described in [39]. We choose $Q = M_{LQ}/2$ as the appropriate momentum scale, since this closely approximates the momentum scale used in ISAJET (the scales are actually equivalent at $\eta = 0$). To calculate an effective K-factor we use ISAJET to count the fraction $f(gg)$ of events which are initiated by gluon-gluon fusion and the fraction $f(q\bar{q})$ that come from $q\bar{q}$-annihilation. The effective K-factor is then given by

$$K_{E\not{H}} = f_{gg}(Q^2)K_{gg}(\alpha_s) + f_{q\bar{q}}(Q^2)K_{q\bar{q}}(\alpha_s) \tag{6.6}$$

with $K_{gg}$ and $K_{q\bar{q}}$ as given above.

The K-factors given in Table 6.2 show that at no point in the mass region of interest is leptoquark pair production actually suppressed and in fact can be significantly enhanced.

## 6.3 Leptoquark Decays

Having produced a pair of leptoquarks, we now turn to their decays. Recall that for both leptoquarks we assume the decay $LQ \to e + u$ with branching fraction $x$. We start this section with an examination of the kinematic distributions for the



resulting electrons and quarks and follow this with a discussion of how we can reconstruct the leptoquark mass.

### 6.3.1 Electron And Jet Kinematics

We first look at the parton-level $E_T$ spectra of the electrons and up-quarks emerging from leptoquark-pair decay. For this we use only the particle 4-momenta and do not attempt to include any fragmentation or hadronization effects, nor do we add any detector simulation. In so doing we are able to observe the true spectra with no biases introduced from trigger or clustering thresholds, for example. Later when we calculate cut acceptances, we will, of course, do so only after full event reconstruction.

In Figure 6.2 we show $E_T^e$ versus $E_T^u$ for four different leptoquark masses, while Figure 6.3 shows the corresponding projections onto the $E_T^e$ axis. We do not show the 1-dimensional $E_T$ spectra for the up-quarks, since for massless $e, u$ we cannot kinematically distinguish the two.

In anticipation of the electron and jet cuts that will be later imposed to reduce Standard Model backgrounds (Section 6.5), we also indicate in Figure 6.2 the effects of imposing 20-GeV cuts on the $E_T$'s of both the electron and up-quark. This gives us a first order indication of the fraction of real leptoquark events that would be likely to survive such cuts as a function of $M_{LQ}$. Clearly the kinematic cut acceptance $A_K$ is very poor at $M_{LQ} = 45$ GeV, while it is very good at 105-GeV. Fortunately, the decrease in event acceptance at lower leptoquark masses is balanced somewhat by the rise in production cross-section. A better variable which quantifies the interplay between the falling cross section and the rising kinematic acceptance is the effective cross section given by

$$\sigma_{E\not{H}} = \sigma \cdot A_K^2 \tag{6.7}$$

Note that we use $A_K^2$ rather than $A_K$ since for pair events there are two leptoquarks to consider. The effective cross sections obtained are shown in Table 6.3.

| | Leptoquark Mass | | | |
|---|---|---|---|---|
| | 45 GeV | 65 GeV | 85 GeV | 105 GeV |
| $\sigma_{ISAJET}$ | 595.5 pb | 94.5 pb | 22.5 pb | 7.0 pb |
| $A_K$ | 17.7 % | 53.1% | 71.7% | 81.4% |
| $\sigma_{Eff}$ | 18.7 pb | 26.6 pb | 11.6 pb | 4.6 pb |

Table 6.3: Kinematic Acceptance Factor $A_K$ and Effective Cross Section as a Function of Leptoquark Mass for 20-GeV Cuts on Final State Particle $E_T$.

### 6.3.2 Leptoquark Mass Reconstruction In $e^+e^-$+Dijet Events

For any leptoquark which decays to an $e + u$ pair, we can find its invariant mass using the electron and jet 4-momenta. Furthermore, in $LQ\overline{LQ}$ production we expect two electrons and two jets in the final state which means that we should be able to reconstruct both leptoquark masses. The observation of two electron-jet pairs of approximately equal mass will therefore be a minimum requirement of any candidate event in the data.

There is, however, a two-fold ambiguity as to the ways we can form electron-jet combinations, leading to two possible sets of reconstructed leptoquark masses.

1. Set 1: $M_1$ = M(Ele$_1$+Jet$_1$) and $M_2$ =M(Ele$_2$+Jet$_2$)
   or
2. Set 2: $M_1$ = M(Ele$_1$+Jet$_2$) and $M_2$ = M(Ele$_2$+Jet$_1$)

To resolve this ambiguity we make use of the fact that for the correct choice, the reconstructed masses $M_1$ and $M_2$ should be approximately the same. That is, assuming all electron and jet energies have been well measured we should find that $M_1 \simeq M_2 \simeq M_{LQ}$. In this analysis we therefore choose the electron-jet combinations for which $M_1 - M_2$ is the smallest (hopefully close to zero).

Using the Monte Carlo leptoquark data sets and applying a full CDF detector simulation, we first plot ($M_1$+$M_2$)/2 after making a random choice as to which set we use on an event by event basis. The results are shown in Figure 6.4 along with Gaussian fits to the mass peak. For all masses shown we observe a long combinatoric tail presumably from the 50% of the events that have incorrectly



paired electron-jet combinations after our random selection. We also note that the position of the fitted mass peak appears to systematically low (2% – 4%) in all cases (except at $M_{LQ}$ = 45 GeV), and one probable explanation is that the measured jet energies do not completely reflect the energies of the parent quarks energy, some having been lost outside of the jet cone, or down simulated detector cracks, for example.

If we now form the ($M_1$+$M_2$)/2 distribution according to the minimum-$\Delta M$ prescription as described above, then we find a reasonable improvement in the mass-peak resolution, with some (though not all) of the old combinatoric tail now contributing to the peak. The results are shown in Figure 6.5, as are the previous distributions from the random-choice approach, and we note that the fitted means are consistent with each other for both methods (as expected). Figure 6.6 justifies our assumption that $M_{LQ1} \simeq M_{LQ2}$ showing well defined clustering about the reconstructed leptoquark mass (in this case 85 GeV).

The conclusions of this study are as follows: Given the fact that we can reconstruct the leptoquark mass to within 4% of its generated value and with the resolutions shown in Figure 6.5, we are confident in our ability to reconstruct $M_{LQ}$ should we observe any signal events. Furthermore the peak resolutions we can attain set a quantitative standard as to how closely two reconstructed electron-jet masses need to match each other in order to be considered compatible with leptoquark pair production.

## 6.4 Estimation Of Kinematic And Geometric Acceptances

In this section we estimate the effect of imposing geometric and kinematic cuts on our signal. The geometric acceptances apply only to the electrons from leptoquark decay and are affected by the application of fiducial volume cuts, and by restricting the $e^+e^-$ pair to a given detector, or pair of detectors. The kinematic cuts, on the other hand, apply to both electrons and reconstructed jets in an event and involve imposing a minimum $E_T$ cutoff.

The kinematic and geometric acceptances found in this section could be combined to give an overall event acceptance as a function of leptoquark mass. However, rather than doing this we will later apply all simultaneously to the Monte Carlo LQ data sets and present the overall acceptances in Section 6.6. The purpose of this section is to illustrate why and how much signal is lost, and which cuts are primarily responsible.

### 6.4.1 Geometric Acceptances

We first consider the effect of restricting the electrons in an event to the fiducial volume of the CDF detector. As was shown in Section 5.7.1, the primary function of the fiducial cuts is to accept only those electrons which are well away from any cracks in the detector, both in $\eta$ and $\phi$ directions.

The $\eta$ fiducial cuts essentially require that the electron seed tower not be in a list of towers close to cracks or major detector interfaces. The restricted regions are clearly visible in Figure 5.2. To estimate acceptances we now need to know the $\eta$-distributions of the electrons in $LQ\overline{LQ}$ events. These are illustrated in Figures 6.7 and 6.8 for 45-GeV and 105-GeV leptoquarks, respectively. The one dimensional distributions show the CDF $\eta$-tower distribution for the leptoquark-decay electrons *only* and those found in restricted towers have been removed. We have also smeared the primary vertex of the events using a Gaussian of width 30cm so as to reflect the corresponding spread observed in the CDF data. All leptoquark samples originally contained 10000 events, and so the 1-D plots show that around 84%(86%) of the electrons are removed by the $\eta$-tower cut for 45(105) GeV electrons. However, since we also have positrons in the event this acceptance must be squared, giving an overall $\eta$ acceptance of 71%(74%) as shown in the two dimensional plots.

Since the decay electrons are emitted isotropically in the $\phi$ direction we can evaluate the $\phi$-crack cut acceptance geometrically without the use of Monte Carlo. For the CEM, the centroid of the electron shower at the strip chambers is required to be more than 3 cm away from any boundary between adjacent 15° calorimeter



wedges. Given the CDF detector geometry, this translates into a CEM $\phi$-cut acceptance of 86.7% for a single electron, and $(86.7\%)^2 = 75.2\%$ for a central-central (CC) $e^+e^-$ pair. Acceptances can be evaluated in a similar manner for the $\phi$−boundaries between PEM and FEM quadrants.

Figures 6.7 and 6.8 also show that the electrons from leptoquark decay are found primarily in the central region of the detector. This is an important point since our analysis of the data will be based on an inclusive *central* electron data set. Before any $\eta - \phi$ fiducial cuts are applied, we can show that requiring both electrons to be found in the CEM means that we retain over 50%(65%) of our signal for 45(105) GeV leptoquarks. If in addition we accept CEM-PEM and CEM-FEM topologies for the $e^+e^-$ pair, we increase our acceptance to 90%(96%) respectively. For this reason we will use the inclusive central electron data set, and will accept all events containing CC, CP,or CF dielectron pairs.

The 'naive' acceptances (that is, before any fiducial cuts or z-vertex smearing) are given in Table 6.4 for several representative leptoquark masses, while Table 6.5 shows the full acceptances after event-vertex smearing and all fiducial cuts, including dead tower elimination in the PEM, and chimney tower and 90° crack removal in the CEM. The second table shows that we lose around half of our signal events to the fiducial volume requirements.

| $M_{LQ}$ (GeV) | 45 | 65 | 85 | 105 |
|---|---|---|---|---|
| P(CC) (%) | 50.9 | 57.0 | 57.9 | 65.5 |
| P(CP) (%) | 31.9 | 30.6 | 31.5 | 27.4 |
| P(CF) (%) | 6.8 | 5.4 | 4.1 | 3.3 |
| P(PP) (%) | 7.0 | 4.8 | 4.4 | 2.7 |
| P(PF) (%) | 2.7 | 1.8 | 1.3 | 1.0 |
| P(FF) (%) | 0.4 | 0.1 | 0.1 | 0.1 |
| P(Cx) (%) | 89.6 | 93.0 | 93.5 | 96.2 |

Table 6.4: Probabilities of Finding the $e^+e^-$ pair from $LQ\overline{LQ}$ Decay in Any Given Detector Topology. No Fiducial Cuts Have Been Applied and there is No Event-Vertex Smearing.

| $M_{LQ}$ (GeV) | 45 | 65 | 85 | 105 |
|---|---|---|---|---|
| P(CC) (%) | 24.2 | 26.7 | 28.4 | 30.8 |
| P(CP) (%) | 16.7 | 16.7 | 15.5 | 15.4 |
| P(CF) (%) | 3.6 | 3.0 | 2.7 | 2.3 |
| P(PP) (%) | 3.7 | 2.9 | 2.4 | 2.0 |
| P(PF) (%) | 1.8 | 1.1 | 0.9 | 0.7 |
| P(FF) (%) | 0.2 | 0.1 | 0.1 | 0.1 |
| P(Cx) (%) | 44.5 | 46.4 | 46.6 | 48.5 |

Table 6.5: Fraction of Generated $LQ\overline{LQ}$ Events Remaining After Event-Vertex Smearing and All Electron Fiducial-Volume Cuts Have Been Applied.

### 6.4.2 Kinematic Acceptances

In Section 6.3.1 we obtained inclusive kinematic acceptance factors for $E_T$ cuts applied to the final state up-quarks and electrons in leptoquark decay (by inclusive we mean that there is no consideration of the electron or quark direction). In the real world we deal not with Monte Carlo particles but with electron and jet clusters. Associated with these are various complicated efficiencies that depend on, amongst other things, calorimeter tower thresholds, electron and jet isolation, energy losses down detector cracks, and the choice of clustering algorithm. Therefore, instead of using the parton level kinematic acceptance, we will evaluate $A_K$ after passing all events through CDF detector simulation and event reconstruction. Since the probability of an electron passing a given $E_T$ cut is $\eta$ dependent we give exclusive acceptances for CC, CP, and CF dielectron configurations. We do not consider jet-$\eta$.

To evaluate kinematic acceptances we start by doing the following:

- Generate 10000 leptoquark events for each $M_{LQ}$ and pass though CDF detector simulation.
- Determine the dielectron detector topology from the smeared event-vertex and parton level four-momenta. Accept only CC, CP, or CF events.
- Form electron and jet clusters using EMCLST and JETCLU with 5-GeV cluster-$E_T$ thresholds. Correct jet and electron energies.



- Keep only events in which both electrons formed separate clusters and which were both in the CDF fiducial detector volume.

After application of the above cuts we are left with a subset of the original 10000 events. We denote by $N_S$ the total number of remaining events and $n_S(Cx)$ the number of these events having a Cx dielectron pair (x=C, P, or F). By definition $n_S(CC)+n_S(CP)+n_S(CF)=N_S$. We now apply kinematic cuts to both electrons and jets for each of the CC, CP, and CF dielectron configurations. The kinematic acceptances are then defined to be

$$A_K(Cx)=\frac{n(Cx)}{n_S(Cx)} \tag{6.8}$$

The results obtained for different values of the $E_T$ cut on both electrons and jets are shown in Table 6.4.2.

| $M_{LQ}$ (GeV) | 45 | 55 | 65 | 75 | 85 | 95 | 105 | 115 |
|---|---|---|---|---|---|---|---|---|
| 15 GeV Electrons and 15 GeV Jets | | | | | | | | |
| $A_K(CC)$ | 36.0 | 61.2 | 72.3 | 80.6 | 84.7 | 88.1 | 89.5 | 90.5 |
| $A_K(CP)$ | 29.8 | 43.8 | 56.5 | 64.5 | 68.9 | 75.3 | 78.2 | 80.3 |
| $A_K(CF)$ | 7.2 | 18.9 | 30.3 | 30.4 | 30.4 | 36.6 | 32.3 | 38.6 |
| 20 GeV Electrons and 15 GeV Jets | | | | | | | | |
| $A_K(CC)$ | 23.5 | 40.5 | 57.2 | 69.3 | 76.2 | 82.9 | 85.5 | 87.2 |
| $A_K(CP)$ | 13.0 | 25.1 | 37.9 | 49.3 | 55.7 | 62.3 | 67.4 | 71.4 |
| $A_K(CF)$ | 2.9 | 9.0 | 15.4 | 13.6 | 13.4 | 18.6 | 17.7 | 20.5 |
| 20 GeV Electrons and 20 GeV Jets | | | | | | | | |
| $A_K(CC)$ | 15.5 | 30.1 | 47.0 | 59.0 | 68.3 | 76.1 | 80.1 | 82.2 |
| $A_K(CP)$ | 8.0 | 18.3 | 30.9 | 42.1 | 49.1 | 57.3 | 62.2 | 67.1 |
| $A_K(CF)$ | 1.0 | 5.6 | 12.5 | 11.7 | 11.9 | 15.3 | 16.7 | 18.7 |

Table 6.6: Kinematic Acceptances (%) by Dielectron Detector Region for Monte Carlo Leptoquark Pair Events. Numbers Give the Fraction of Events with the Given Dielectron Topology Which Also Pass Electron and Jet Kinematic Cuts.

Thus, for example, of all 45-GeV leptoquark pair events that contain a CF electron pair passing the cuts given in the list above, only 0.96% of them pass a cut of $E_T > 20$-GeV for both electrons and jets. As can be seen, 20-GeV cuts bite heavily into our signal. As expected the kinematic acceptance is largest in the central region and, as was shown in the previous section, this is fortunately where most of our events are found.

The overall event acceptance is a combination of the geometric and kinematic acceptances as well as those for any other cuts we might apply (such as z-vertex, electron quality etc.).

## 6.5 Sources Of Background And Their removal

### 6.5.1 $b\bar{b}$-Pair Production

The inclusive $b$-quark production cross section in $\bar{p}p$ collisions at $\sqrt{s} = 1800$ GeV is expected to be around $\sim 20\mu b$, assuming the rapidity of the $b$-quark to be in the region $|y| < 1$ and with no minimum $P_T^b$ cut [66]. Given this cross section, we expect a sizeable number of $b\bar{b}$ events in which both $b$-quarks have decayed semileptonically via $b \longrightarrow ce\nu_e$. If $P_T^b$ is high enough, the resulting c-quark can form a well defined jet, and when this is true for both $b$'s in a $b\bar{b}$ event we expect to observe a dielectron-dijet final state.

At first sight this might appear to be a serious background to our signal. However, we will argue that such events are easily removed through two independent effects, both of which conspire to help us.

Firstly, the $b$-production cross section falls steeply as we increase the minimum $P_T^b$ cut. For example, with $P_T^{min}(b) > 20$ GeV, the inclusive production cross section has dropped to around $0.2\mu b$. In this analysis we cut on electron $E_T$ rather than $P_T^b$ and so a more relevant quantity to consider when estimating $b\bar{b}$ contributions to our data set is the decay-electron $E_T$ spectrum. In the CDF top quark search in the $e\mu$ channel [67], an estimate was made of events expected in the 1988-89 Data set which contain high $E_T$ lepton pairs (in this case $e + \mu$) from $b\bar{b}$ decays. It was found that when the $E_T$ of both leptons is above 13 GeV or so, we would expect less than one event in our data. The $b\bar{b}$ cross-section falls rapidly with the $P_T^{min}$ cut imposed on both leptons. We then expect that based on this alone we can completely eliminate $b\bar{b}$ as a source of background when the $E_T$'s of both leptons are required to be $> 15$ GeV. After our analysis of the $\gamma, Z^0$ background we will actually impose a cut of $E_T > 20$ GeV for at least two electrons in any event, which in terms of $b\bar{b}$ production is obviously far more



restrictive.

Secondly, as we mentioned in Section 5.3, the electron-jet separation in a $b \rightarrow ce\nu_e$ decay decreases with the $P_T$ of the $b$-quark. Again, high energy electrons imply high energy $b$-quarks. We conclude that any electron from a $b$ decay that passes our cut $E_T > 15$ GeV is almost certainly likely to fail our isolation cut $ISO_4 < 0.1$.

We expect no events in our data sample from $b\bar{b}$-production after the imposition of electron-$E_T$ and isolation requirements. Finally there is the fact that so far we have not made any requirement on the $E_T$ of the jets in an event. As we will later discuss in Section 6.5.3, events will be required to contain at least two jets each passing a cut of jet-$E_T > 20$ GeV to reduce contributions from $\gamma, Z^0$+multijet production. Events containing two isolated 20-GeV electrons and two 20-GeV jets are incompatible with $b\bar{b}$-production at CDF.

### 6.5.2 $t\bar{t}$-Pair Production

Recent searches at CDF for the top quark place its mass above 91 GeV (in the absence of a non Standard Model charged Higgs boson). Assuming they exist, the decay of a pair of such heavy top quarks can easily give two high $P_T$ electrons and two jets which pass our kinematic cuts. Furthermore, the non-isolation arguments given in the $b$-quark case no longer apply here.

Although previous top searches at CDF, albeit with somewhat different cuts than in this analysis, failed to find any candidate events in the dielectron dijet channel, we must include $t\bar{t}$ production in our set of possible backgrounds if presented with a small number of candidate events. Further careful analysis of the topology and kinematic properties of each event would then allow us to make statements as to the likelihood of each of the possible parent processes.

### 6.5.3 $\gamma, Z^0$+Multijet Production

At CDF the dominant sources of high-$E_T$ isolated electrons are the decays of the electroweak bosons $W^{\pm} \rightarrow e^{\pm}\nu_e$ and $Z^0 \rightarrow e^+e^-$. At $\sqrt{s} = 1.8$ TeV the W-pair

production cross section is of order 10pb. When scaled by the Standard Model branching ratio $BR(W \rightarrow e\nu)^2 = (9.14\%)^2$ the effective cross section is $\sim 0.08$ pb which leads to only around 0.3 events *produced* in 4 pb$^{-1}$. We therefore do not consider W-pair production as a source of high-$E_T$ electron pairs.

The single $Z^0$ cross section, on the other hand, has been measured at CDF to be $\sigma \cdot BR(Z^0 \rightarrow e^+e^-) \simeq 200$ pb [65]. This corresponds to several hundred events containing pairs of electrons whose $E_T$ distributions peak at around 45 GeV. In addition to Z-production we also expect a continuum of lower mass electron pairs arising from Drell-Yan production $\bar{p}p \rightarrow \gamma + X \rightarrow e^+e^- + X$ (high mass Drell-Yan is also present but has a steeply falling cross-section). Despite its relatively large cross-section, *leading order* $\gamma, Z^0 \rightarrow e^+e^-$ processes are not a source of background to our signal since we recall that in leptoquark pair events we also expect two high-$E_T$ jets.

At higher orders in QCD perturbation theory however, the situation is not so good. The effects of gluon radiation from incoming quarks can lead to one or more high-$E_T$ jets in $Z^0 \rightarrow e^+e^-$ events. Examples of double initial state radiations, relevant to this analysis, are shown in Figure 6.9. Other higher-order processes that can lead to a dielectron+dijet final state include the radiation of a single high energy gluon in the initial state which then fragments into either a $q\bar{q}$ or $gg$ pair, the so-called gluon-splitting process, though the effective cross section for these processes is small when compared to double independent gluon radiation.

Before assessing the impact of such processes in terms of their contribution to our data-set, we first make some qualitative observations. Firstly, since $\alpha_s(Q^2) < 1$ at the energy scales involved here, we expect the cross section to decrease with jet multiplicity (this follows because each additional jet in an event requires another QCD vertex in the corresponding Feynman diagram). Specifically we expect

$$\frac{\sigma(Z + (n+1)\text{jets})}{\sigma(Z + (n)\text{jets})} \sim \alpha_s \simeq 0.2 \qquad (6.9)$$

and indeed this is one way of actually measuring $\alpha_s$. The consequences of the observation for this analysis, however, are that instead of a cross section of $200pb$,



we can make a very crude estimate of the $Z + 2$jet cross section to be around $200 \times (0.2)^2 \simeq 8pb$ (the branching ratio to $e^+e^-$ is included). We say 'very crude' since we have to be careful what we mean by a radiated jet.

This brings us to the second observation, which is that gluon radiation from quarks falls with both the energy of the radiated gluon and the quark-gluon opening angle. Turning the picture the other way around, we find that the QCD cross-section actually becomes divergent as $E_g \rightarrow 0$ (infra-red divergence) and/or $\Delta\theta(qg) \rightarrow 0$ (co-linear singularity). This is why we have to be careful in our jet definition. There exist several schemes within QCD to regulate these divergences, but the final outcome is that in calculating tree-level higher-order cross sections (including loops actually cancels some of the divergences) we usually have to specify both a minimum $E_T$ for any radiated jet, and also a minimum $qg$ opening-angle. In [70] for example, the $Z^0 + 2$jet cross section is given for 15 GeV ($E_T$ cut) jets in the rapidity region $|\eta| < 2$ ($qg$ separation cut) and $\Delta R_{jj} > 0.7$. The cross section given is in the range $3.2 - 5.2$pb depending on the choice of $Q^2$ scale. For 22 GeV jets, the cross section is predicted to be around $1.5 - 2.2$pb. For 20 GeV jets we might therefore expect a cross section of $2 - 3$ pb, or 8-12 events, before scaling by detector efficiencies etc. Presumably there is also a contribution form Drell-Yan+2jet events.

Given then that we expect a non-negligible number of such events, we ask the question do they look like our signal events? Unfortunately the answer is yes. The electrons should, on average, be very well separated from the jets and would therefore easily pass our isolation cuts. This is because, unlike in b-decay, the electron-jet pairs do not originate from a common parent. Furthermore the $E_T$ of the initial state jets tend to boost the $Z^0$ in the opposite direction, leading naturally to large electron-jet opening angles and distorting the back-to-back signature of a $Z^0$ decaying at rest. Topologically then, $\gamma, Z^0 + 2$jet events are inseparable from our signal. The one strong distinguishing factor, however, is the dielectron mass which we expect to be sharply peaked at $M_{ee} = 91$ GeV for the background, while displaying a much broader continuum distribution for the uncorrelated electrons in leptoquark-pair events.

Having given a qualitative picture, we now proceed to make somewhat more quantitative statements about what contributions we expect from $\gamma, Z^0 + 2$jet events. For this purpose we use the PAPAGENO Monte Carlo event generator v3.41 [68] to estimate the differential cross section as a function of dielectron invariant mass (that is, $d\sigma/dM_{e^+e^-}$). Like the ISAJET Monte Carlo described earlier, PAPAGENO calculates a cross section based on a hard scattering parton level cross section $\hat{\sigma}$ convoluted with the appropriate parton distributions functions. All parton level calculations in PAPAGENO are based on tree-level Feynman diagrams (that is, no loop corrections). Events are generated randomly throughout the whole phase space available to the initial and final state particles and all are retained with a weight proportional to the event cross section. This is in contrast to ISAJET which 'unweights' events at the time of their generation, as outlined in Section 6.2.1. In PAPAGENO it is left to the Monte Carlo user to perform this unweighting.

The cuts we make to avoid the cross-section divergences mentioned above are

- $E_T$ jet $> 15 - 20$ GeV
- $|\eta_j| < 3.5$,
- $\Delta R_{jj} > 0.8$.

We estimate the differential cross section at many points in the interval $5 < M_{ee} < 175$ GeV and for several different choices of minimum$-E_T$ for both electrons and jets. We emphasize that these are production cross sections, and to extract effective cross sections we would need to scale by appropriate kinematic and geometric acceptances.

The cross sections obtained from PAPAGENO are shown in Figure 6.10. The $Z^0$ peak is clearly visible and dominates the distributions (we stress that the plot is presented on a log-scale). We define the $Z^0$ peak to be the region $75 < M_{ee} < 105$ GeV and propose to remove any events from our data sample that fall within this region. The final jet-$E_T$ cut we use is $E_T > 20$ GeV for both jets since this reduces contributions from the Drell-Yan continuum outside the Z-peak to



acceptable levels without seriously compromising our leptoquark signal. For this analysis, the relevant curve in Figure 6.10 is therefore the lowest one (E2020-J2020).

By integrating the differential cross-section over the appropriate mass range we can obtain the number of events under, and outside, the Z-peak. The results are as follows

$$\int_{75}^{105} \frac{d\sigma}{dM_{ee}} dM_{ee} = 3.38\text{pb} \tag{6.10}$$

and

$$\int_{5}^{75} + \int_{105}^{175} \frac{d\sigma}{dM_{ee}} dM_{ee} = 0.57\text{pb} \tag{6.11}$$

The effective cross sections are obtained by scaling these production cross sections by a kinematic and geometric acceptance factor of $\sim 30\%$. This acceptance factor is obtained by performing event unweighting and full CDF detector simulation for one of the PAPAGENO data sets ($M_{ee} = 45$ GeV). All events are subjected to the kinematic, isolation, and fiducial cuts described in the previous chapter, as well as requiring only events with CC, CP, or CF dielectron topologies. We assume the 30% acceptance factor for all dielectron masses in the range 5-175 GeV. However, we note that the very low mass electron pairs are more likely to fail our kinematic cuts and so the effective cross section in the region below the Z-peak may be a little overestimated.

Scaling the PAPAGENO cross sections by 30% and multiplying by 4.05 pb$^{-1}$ we obtain the prediction

$$4.2 \pm 0.5 \pm 1.1 \text{ Events under the Z-peak}$$

and

$$0.7 \pm 0.1 \pm 0.2 \text{ Events outside of the Z-peak}$$

The first error shown comes from a 7% luminosity uncertainty and a 10% error on the acceptance scaling factor. The second , larger, error reflects the theoretical uncertainty on the normalization of the PAPAGENO cross section. This arises mainly from our lack of knowledge about the correct choice of $Q^2$ scale to use in our Monte Carlo. Different choices lead to a spread in the cross section of $\sim \pm 25\%$.

We have shown that the Z-peak cut is very effective and eliminates around 85% of the $\gamma, Z^0 + 2$jet background, leaving less than 1 event expected in our data set. However, removing events with $75 < M_{ee} < 105$ GeV has a non-negligible effect on our signal. Using the Monte Carlo leptoquark samples we form the dielectron mass distributions for each of the five leptoquark masses considered as shown in Figure 6.11. To make a quantitative estimate of how many $LQ\overline{LQ}$ events are likely to pass the cut, we simply count the fraction which survive and use this as our acceptance. The results presented in Table 6.7 show that we are losing around 25% of our signal.

| $M_{LQ}$ (GeV) | 45 | 65 | 85 | 105 | 125 |
|---|---|---|---|---|---|
| Acceptance (%) | $75.6 \pm 2.5$ | $76.3 \pm 1.2$ | $73.5 \pm 0.9$ | $75.7 \pm 0.8$ | $80.5 \pm 0.7$ |

Table 6.7: Fraction of $LQ\overline{LQ}$ Events Which Survive the Cut $75 < M_{ee} < 105$ GeV. All Other Cuts Have Been Made and the Indicated Errors Are Statistical Only.

The conclusions of this section are that with appropriate cuts on dielectron mass, electron-$E_T$, and jet-$E_T$, we can substantially reduce our last remaining major background to less than one event expected in our data set. Given that we expect no events from the other background ($b\bar{b}$ production) any events which we find in our data set after all cuts will be either cause for excitement or a re-investigation of our background estimates!

Before describing the data analysis we briefly present in the next section a summary of the acceptances of all our cuts for the leptoquark signal, and the corresponding number of expected events.

## 6.6 Expected Signal After All Cuts

The final set cuts used in the $e^+e^-$+dijet channel is as follows:

- At least two electrons with $E_T > 20$ GeV
- At least two jets with $E_T > 20$ GeV
- Only C-C, C-P, and C-F dielectron topologies are allowed



- Both electrons must be in the fiducial detector volume
- Both electrons must pass the isolation cut $ISO_4 < 0.1$
- Both electrons must pass the electron quality cuts listed in Section 5.6
- Events with $75 < M(e^+e^-) < 105$ GeV are removed
- Event z-vertex must satisfy $|z_v| < 60$ cm.

Using the Monte Carlo leptoquark samples we obtain the fraction of generated events which pass all of the cuts listed above *excluding* the electron-quality cuts. We do not explicitly apply quality cuts in our Monte Carlo samples since we thereby minimize our reliance on our ability to accurately simulate many detailed subsystems of the CDF detector. Instead, we will scale the Monte Carlo acceptances, obtained for all other cuts, by the quality acceptances. However, since the electron quality acceptances vary by detector region the price we have to pay is that we must estimate the Monte Carlo acceptances for each of the allowed cases of dielectron final state. In Table 6.8 we therefore show the fraction of events which pass all cuts (excluding quality) for CC, CP, and CF dielectron configurations. The $\eta$ position of any jet in the event is not restricted, though we note that the $E_T > 20$ GeV cut is sufficient to limit $|\eta| < 3.5$ or so.

| $M_{LQ}$ (GeV) | $A_{CC}$ % | $A_{CP}$ % | $A_{CF}$ % |
|---|---|---|---|
| 45 | $1.59 \pm 0.08$ | $0.57 \pm 0.05$ | $0.02 \pm 0.01$ |
| 65 | $6.41 \pm 0.24$ | $2.43 \pm 0.15$ | $0.06 \pm 0.02$ |
| 85 | $11.30 \pm 0.32$ | $4.32 \pm 0.20$ | $0.13 \pm 0.04$ |
| 105 | $14.60 \pm 0.35$ | $5.58 \pm 0.23$ | $0.24 \pm 0.05$ |
| 125 | $17.75 \pm 0.38$ | $6.73 \pm 0.25$ | $0.41 \pm 0.06$ |

Table 6.8: Monte Carlo Event Acceptances for CC, CP, and CF Dielectron Topologies As a Function of Leptoquark Mass. All Cuts, Excluding $z_v$ and Electron Quality Requirements, Have Been Imposed.

The above acceptances are calculated using Monte Carlo event samples of between 10000 and 22000 events. The errors shown are simply the binomial

errors incurred whenever we perform a counting experiment with a finite data sample.

We now use the Monte Carlo event acceptances given in Table 6.8 to estimate the final number of $e^+e^-$+dijet events we would expect to *observe* in 4.05 pb$^{-1}$. Note that we will assume $x = BR(LQ \rightarrow e+u) = 100\%$ and for any other $x < 1.0$ the predictions must be scaled accordingly (a factor $x^2$).

The total number of expected events is given by

$$N = \sigma(M_{LQ}) \cdot \mathcal{L} \cdot \epsilon_Z \cdot [A_{CC}\epsilon_C^2 + A_{CP}\epsilon_C\epsilon_P + A_{CF}\epsilon_C\epsilon_F] \qquad (6.12)$$

The cross sections are those from Section 6.2 which are leading order predictions obtained with ISAJET and HMRS-B structure functions. $\mathcal{L}$ is the integrated luminosity, 4.05 pb$^{-1}$. We have defined $\epsilon_z$ to be the efficiency of the 60 cm z-vertex cut (95.44%), while $\epsilon_x$ is the electron quality cut efficiency for the detector-$x$. These efficiencies have been measured for high-$E_T$ isolated electrons [64, 65] and were determined to be

$$\epsilon_C = 87.3 \pm 2.3\% \qquad (6.13)$$

$$\epsilon_P = 94.1 \pm 2.1\% \qquad (6.14)$$

and

$$\epsilon_F = 100.0 \pm 0.5\% \qquad (6.15)$$

| $M_{LQ}$ (GeV) | $\sigma$ (pb) | $N_{CC}$ | $N_{CP}$ | $N_{CF}$ | $N_{TOT}$ | $A$ (%) |
|---|---|---|---|---|---|---|
| 45 | 595.5 | 27.9±1.4 | 10.8±0.9 | 0.4±0.2 | 39.1±1.7 | 1.6±0.1 |
| 65 | 94.5 | 17.8±0.7 | 7.3±0.4 | 0.2±0.1 | 25.3±0.8 | 6.6±0.3 |
| 85 | 22.5 | 7.5±0.2 | 3.1±0.1 | 0.1±0.0 | 10.7±0.2 | 11.7±0.5 |
| 105 | 6.9 | 3.0±0.1 | 1.2±0.1 | 0.1±0.0 | 4.3±0.1 | 15.2±0.7 |
| 125 | 2.5 | 1.3±0.0 | 0.5±0.0 | 0.0±0.0 | 1.8±0.1 | 18.5±0.8 |

Table 6.9: Expected Number of $e^+e^-$+Dijet Events in 4.05pb$^{-1}$ as a Function of Leptoquark Mass. Numbers are After All Cuts Have Been Applied and we give Separate Estimates for the Three Allowed Dielectron Detector-Topologies. Also Shown are the Overall Final Acceptances.



The overall event acceptance in Table 6.9 is defined through Equation 6.12 and is simply

$$A = \epsilon_Z \cdot [A_{CC}\epsilon_C^2 + A_{CP}\epsilon_C\epsilon_P + A_{CF}\epsilon_C\epsilon_F] \qquad (6.16)$$

The quoted uncertainties on $A$ are obtained from the statistical errors on the $A_{Cx}$ and the systematic errors on the $\epsilon_x$.

The overall acceptance at low leptoquark masses is relatively poor but as discussed in Section 6.3, this is something that we can live with given the corresponding large cross sections. Indeed Table 6.9 shows that we can expect an easily observable signal at low leptoquark masses (again assuming $x = 100\%$) with around 40 events predicted above a background of around one event. By $M_{LQ} = 125$ GeV, we have clearly run out of cross section, even though our event acceptances are an order of magnitude better than at $M_{LQ} = 45$ GeV, leaving us with only one or two events at these high masses.

## 6.7 Analysis Of The CDF Data

Our starting point is the CDF inclusive central electron data set composed of 4997 events and described in detail in Chapter 5. Each event contains at least one 20-GeV central electron passing tight electron quality and isolation cuts.

In the present analysis we expect events with an $e^+e^-$+dijet signature, and where, on average, both electrons have $E_T > 20$ GeV for all but the lowest leptoquark masses considered. Our first priority then is to convert the inclusive central electron data set into a high-$E_T$ dielectron sample. Instead of restricting a second electron candidate to the central rapidity region, we can significantly increase our event acceptance by also admitting events containing Plug or Forward electrons as was described in Section 6.4.2. We also impose only a fairly loose kinematic cut of $E_T(\text{Ele}_2) > 10$ GeV to begin with, so as to increase sensitivity to any obvious signal at low $M_{LQ}$. In addition, the second electron must pass the appropriate detector-specific quality cuts, which were listed and explained in Chapter 5. Isolation requirements for the second electron are not made at this point, nor do we yet require either electron to be in the fiducial volume of the

detector.

With these requirements on a second electron in an event we find that around 90% of the data is removed leaving us with 423 events. The dielectron mass distribution for these events is shown in Figure 6.12 and with over 70% of the sample having high mass electron pairs in the range $80 < m_{ee} < 100$ GeV, it is clearly dominated by contributions from the process $Z^0 \rightarrow e^+e^-$. A Gaussian fit to the peak over the range $80 < M_{ee} < 100$ GeV gives the $Z^0$ mass as $90.8 \pm 0.3$ GeV, with a Gaussian width of $4.4 \pm 0.4$ GeV. The fact that the reconstructed $Z^0$ mass is within 0.3% of the current world average gives us confidence that we are correctly identifying and measuring the energy of high-$E_T$ electrons.

Having made a dielectron data sample, we now look for the additional presence of one or more jets in an event. As in the case of the second electron, we start with loose kinematic cuts, requiring any jet to pass the cut $E_T > 10$ GeV. We examine the $E_T$ spectra for the jets, recalling from Section 6.5.3 that in $\gamma, Z^0$+multijet events the cross section is expected to fall steeply with both jet-$E_T$ and jet multiplicity. The jet-$E_T$ spectra are shown in Figure 6.13 for the 170(61) events containing one(two) or more such jets. The shapes of the $E_T$ spectra appear to be consistent with expectations from initial state radiation effects, and there is no indication of an excess of $e^+e^-$+2jet events compared to $e^+e^-$+1jet events. Each distribution falls steeply, and there are few events out on the long exponential tail past $E_T > 30$ GeV. The fact that we see only seven dielectron events with two or more jets having $E_T > 20$ GeV immediately implies that there will be no large signal at intermediate to high leptoquark masses. For the present time we keep the loose kinematic cuts as they are and proceed to form electron-jet mass combinations in the hope of seeing an unexpected peak.

In Figure 6.14 we show the invariant masses of the two electron-jet combinations chosen as explained in Section 6.3.2, and the corresponding dielectron mass spectrum. In order that the electron energies be well measured, and hence that all invariant masses be reliably reconstructed, we now require that both electrons be in the fiducial volume of the CDF detector. This reduces the number of events from 61 to 41. Of these, 32 have a dielectron mass in the range $75 < M_{ee} < 105$



GeV, and are therefore *labelled*, not *identified*, as $Z^0 + 2$jet events. We also find 9 events that have dielectron masses outside of the $Z^0$ mass-window and similarly these are 'labelled' as $\gamma$+2jet events.

Requiring that the second electron now be isolated removes most of the 9 low and very high-mass events while leaving most of the 'Z' events. Figure 6.15 shows the same distributions after the isolation cut on the second electron and we see that we are left with 29(3) $Z(\gamma) + 2$jet events. Of these 32, 4 have very high electron-jet masses (both masses $> 100-$GeV) and one does not appear to be consistent with $Z^0$+2jet production. These events are summarized in the following table

| Run/Event | M(Ele-Jet)$_1$ | M(Ele-Jet)$_2$ | $E_T^{e1}$ | $E_T^{e2}$ | $E_T^{j1}$ | $E_T^{j2}$ | M(ee) |
|---|---|---|---|---|---|---|---|
| 17864/767 | 135.1 | 143.1 | 106.6 | 95.7 | 12.9 | 11.9 | 203.3 |
| 18172/12627 | 164.1 | 121.6 | 44.5 | 39.2 | 17.5 | 11.3 | 84.9 |
| 19156/12838 | 121.6 | 134.6 | 67.8 | 59.7 | 58.1 | 11.6 | 89.1 |
| 20070/26100 | 160.4 | 114.9 | 36.8 | 35.7 | 33.1 | 17.4 | 94.7 |

Table 6.10: Properties of Events with High Electron-Jet Masses in the CDF $e^+e^-$+Dijet Data for Loose (10 GeV) Cuts on Jets and the Second Electron.

The single $\gamma$+2jet event in the table, Run 17864/767, appears to be just that, namely a very high mass $\gamma \rightarrow e^+e^-$ event with two low-$E_T$ jets that barely pass our kinematic cutoff. Both of these jets are found in the forward regions of the detector, another indication of initial state radiation. If we were really observing the production of a pair of 140-GeV leptoquarks, as the electron-jet masses would suggest, then we consider it extremely unlikely that both jets would have such small $E_T$'s, and would be located so far from the central part of the detector.

The other 3 events have dielectron masses close to $M_{Z^0}$, and in the case of each of the second jets, the $E_T$'s again appear inconsistent with production of such high mass leptoquarks.

Event 19156/12838, though probably inconsistent with leptoquark production, is interesting for several reasons, and we use it as an illustration of the work involved when attempting to identify the parent process for a particular event. The CDF calorimeter and tracking displays for this event are shown in Figures 6.16

and 6.17 respectively. The calorimeter display shows a so-called 'lego-plot' which is essentially a three-dimensional representation of transverse energy deposited (vertical axis) as a function of $\eta - \phi$ tower. Hadronic energy is lightly shaded, electromagnetic is somewhat darker. The display shows tracks in the $r - \phi$ plane of the CTC. Calorimeter information is also shown in lego form around the outside of the CTC.

The event in question contains two high $E_T$ central electrons, which can be seen as large isolated electromagnetic energy depositions, each associated with a stiff track in the CTC. The dielectron mass is $M(e^+e^-) = 89.1$ GeV. In addition the event contains a relatively high-$E_T$ (58 GeV) central jet. The second jet in the event has low $E_T$ and is found in the forward region. The $\phi$ locations of the electrons and central jet ($23°, 295°, 163°$) appear to indicate, geometrically at least, that the event is a high $P_T$ $Z^0$-decay balanced by a recoil jet. The $Z_{P_T}$ is calculated and found to be 92 GeV, somewhat above the 58 GeV of recoil provided by the jet. However, after summing all calorimeter energies in the event we find 52-GeV of missing-$E_T$ at $\phi = 164°$, that is, almost exactly in the direction of the recoil jet. Assuming that the jet was somehow mis-measured (see discussion in Section 4.2.3) we can account for all of the $Z_{P_T}$ and can therefore, we believe, explain the event. The new electron-jet masses using the corrected jet energy are $M_1 = 143$ GeV and $M_2 = 156$ GeV.

We turn now to the lower mass electron-jet pairs shown in Figure 6.15. The motivation for an initially loose $E_T$-cut of 10-GeV was to make sure we were not missing a large signal at $M_{LQ} < 45$ GeV, though in light of the LEP results discussed in Chapter 2 this would be extremely unlikely. Indeed, we see no obvious clustering of events at low leptoquark mass. Furthermore, all but two of the low electron-jet mass events appear to be consistent with $Z$+2jet production. For these two events we find $M(e^+e^-) \sim 50$ GeV, while the $E_T$ of the two jets are (18 and 15) GeV for the first event, and (27 and 14) GeV for the second. The reconstructed leptoquark mass pairs are (26 and 37) GeV and (38 and 42) GeV, respectively. While neither event is inconsistent with relatively light leptoquark pair production, such an observation is expected from standard $\gamma$+2jet production



given that we predict 0.7 such background events with tighter $E_T$ cuts. There is then no excess of events and therefore no reason to suspect a low-mass leptoquark signal. We also note that the reconstructed leptoquark masses for these two events are below the lower limit excluded by LEP at 95% CL.

Having checked there is no obvious low mass signal we now raise our $E_T$ cuts to 20 GeV on the electrons and 15-GeV on the jets. Though not shown, we find 7 events with $75 < M_{ee} < 105$ GeV, and 1 event outside of this region with $M_{ee} = 54$ GeV. Integrating the E2020-J1515 differential cross section shown in Figure 6.10, and scaling by $\mathcal{L} \cdot 30\%$ (see Section 6.5.3) we predict

$$8.0 \pm 1.0 \pm 2.0 \text{ Events under the Z-peak}$$

and

$$1.2 \pm 0.1 \pm 0.3 \text{ Events outside of the Z-peak}$$

for these cuts. Our observation is therefore consistent, within errors, with the Monte Carlo prediction for the $\gamma, Z^0$+multijet rate.

Finally we raise the jet $E_T$ threshold to its chosen value of 20-GeV, giving us a kinematic regime where we would expect a reasonable signal and minimal background (less than one event) in our signal region. The electron-jet mass and dielectron mass plots are shown in Figure 6.18 for unrestricted isolation of the second electron, and in Figure 6.19 when both electrons pass $ISO_4 < 0.1$. These are our final cuts, and as can be seen only three events survive. All three events are consistent with $Z^0$+2jet production and are summarized in Table 6.11.

| Run/Event | M(Ele-Jet)$_1$ | M(Ele-Jet)$_2$ | $E_T^{e,1}$ | $E_T^{e,2}$ | $E_T^{j,1}$ | $E_T^{j,2}$ | M(ee) |
|---|---|---|---|---|---|---|---|
| 19967/74900 | 92.1 | 100.9 | 53.5 | 27.6 | 37.8 | 20.9 | 92.1 |
| 16036/164 | 60.6 | 101.4 | 36.0 | 28.2 | 41.2 | 40.4 | 87.8 |
| 17931/34787 | 61.6 | 59.4 | 35.5 | 30.5 | 24.8 | 21.9 | 94.4 |

Table 6.11: Summary of All Events in the CDF $e^+e^-$+Dijet Data After Tight (20 GeV) $E_T$ Cuts on Electrons and Jets, and Isolation, Quality, and Fiducial Requirements for the Electrons.

After removing all events that fall within the Z-mass window $75 < M(e^+e^-) < 105$ GeV we are left with no events in our signal region.

In summary we have found no evidence for leptoquark pair production in the $e^+e^-$+dijet channel. We observe 3 events with $75 < m_{ee} < 105$ GeV and 20-GeV $E_T$ cuts on both electrons and jets, consistent with our Monte Carlo prediction of $4.2 \pm 0.5 \pm 1.1$ events from $Z^0$+dijet production (Section 6.5.3). In our signal region $5 < m_{ee} < 175$ GeV, but excluding the $Z^0$ mass window, we find no events. This is again consistent with our Monte Carlo study where we find we expect $0.7 \pm 0.1 \pm 0.2$ $\gamma$+2jet events for the same set of cuts. We have also shown that when the kinematic cutoffs are relaxed there is no signal either in terms of electron-jet mass clustering or an excess of events above the predicted background. It now remains to draw conclusions based upon this.

## 6.8 Limits On Generation-1 Leptoquarks From The $e^+e^-$+Dijet Channel

Despite the fact that we see no events in our data set, we can still use this null observation to set new limits on the leptoquark production cross section $\sigma \cdot x^2$ as a function of leptoquark mass, where as usual $x = BR(LQ \rightarrow e + u)$. From this measurement, we can derive limits on the leptoquark mass and charged branching fraction $x$ by assuming a given cross section prediction, in our case that estimated by ISAJET. Our final limits will be derived after the inclusion of all major sources of systematic error. However, before doing so, we illustrate the method in the simpler case where such uncertainties are absent.

### 6.8.1 Limits In The Absence Of Systematic Uncertainties

The *measured* cross-section for leptoquark pair production is given by

$$\sigma \cdot x^2(\text{Measured}) = \frac{N(\text{Observed})}{\mathcal{L} \cdot A} \tag{6.17}$$

where $\mathcal{L}$ is the integrated luminosity for the data set (4.05 pb$^{-1}$) and $A$ is the overall event acceptance (Table 6.9). With no events observed Equation 6.17 would naively imply a measured production cross section of 0 pb. A more useful



quantity is the 95% upper confidence level on the cross section which is given by

$$\sigma \cdot x^2(95\%CL) < \frac{N_{95}}{\mathcal{L} \cdot A}. \tag{6.18}$$

Instead of $N$(Observed) we now use $N_{95}$ which is defined to be the maximum number of events in our data set compatible at the 95% CL with an observation of zero events. What do we mean by this? Imagine we repeat our measurement of the number of leptoquark events an infinite number of times. If for each measurement we expect to find $N_{95}$ events, then the probability of observing zero events should be less than $< 5\%$ on average. In calculating $\sigma \cdot x^2$ (95% CL) we need only determine the value of $N_{95}$, since $\mathcal{L}$ and $A$ are already known. Note that since our event acceptances are dependent on $M_{LQ}$, we expect that $N_{95}$ and hence $\sigma \cdot x^2$ also share this dependence.

The statistical probability distribution appropriate for the description of measurements that produce very small numbers of events (in our case zero) out of very many tested, is the Poisson distribution given by

$$P_\mu(n) = \frac{\mu^n e^{-\mu}}{n!}. \tag{6.19}$$

$P_\mu(n)$ is the probability of observing $n$ events when $\mu$ are expected (see also the appendix). In the case where $N_0$ events are observed, $N_{95}(> N_0)$ involves finding $\mu_0 = N_{95}$ which satisfies the equation

$$\sum_{n=0}^{N_0} \frac{e^{-\mu_0}\mu_0^n}{n!} = 5\% \tag{6.20}$$

This is usually solved numerically except in the particularly simple case when $N_0 = 0$. This happens to be true for the present analysis and we then just need the value of $\mu$ which satisfies

$$e^{-\mu} = 0.05 \tag{6.21}$$

This is easily found and we therefore have the result that $N_{95} = 2.996$ in the absence of systematic errors.

Using Equation 6.18 and the acceptances presented in Section 6.6, we have our first limits on generation-1 leptoquark production. These are presented in Table 6.12 along with the predictions from ISAJET assuming $x = 100\%$.

| $M_{LQ}$ (GeV) | 45 | 65 | 85 | 105 | 125 |
|---|---|---|---|---|---|
| $\sigma$(ISAJET) (pb) | 595.5 | 94.5 | 22.5 | 6.95 | 2.54 |
| $\sigma \cdot x^2$(Measured) (pb) | 46.2 | 11.2 | 6.3 | 4.9 | 4.0 |

Table 6.12: Limits on the Generation-1 Leptoquark Production Cross Section $\sigma \cdot x^2$ at 95% CL. No Systematic or Statistical Errors are Included. Also Shown is the ISAJET Prediction With $x = 100\%$.

We note from these results that we can exclude $M_{LQ} < 105$ GeV at 95% CL in the absence of systematic errors, assuming the ISAJET cross section; we cannot however exclude $M_{LQ} < 125$ GeV. A more precise mass limit can be obtained by finding that value of $M_{LQ}$ for which our measurement and the ISAJET prediction coincide, but we postpone deriving this limit until the next section when we include systematic uncertainties.

Limits on the charged branching fraction $x$ at the 95% CL are easily obtained from $\sigma \cdot x^2$ limits by assuming a particular cross section. From Equation 6.18 we have

$$x^2(95\%CL) < \frac{N(95\%CL)}{\sigma \cdot \mathcal{L} \cdot A} \tag{6.22}$$

which is just

$$x^2(95\%CL) < \frac{N(95\%CL)}{N(\mathrm{MC}; x = 100\%)} \tag{6.23}$$

Assuming the cross-section values given by ISAJET we obtain the following upper limits on $x = BR(LQ \rightarrow e + u)$

| $M_{LQ}$ (GeV) | 45 | 65 | 85 | 105 | 125 |
|---|---|---|---|---|---|
| Upper Limit on $x$ (%) | 27.9 | 34.5 | 53.0 | 84.0 | 126.4 |

Table 6.13: 95% CL Limits on the Generation-1 Leptoquark Branching Fraction $x = BR(LQ \rightarrow e + u)$. No Systematic or Statistical Errors are Included and the Results Assume the ISAJET Prediction for the Pair-Production Cross Section

Again we note that we cannot set any limits in the case that $M_{LQ} > 125$ GeV.



### 6.8.2 Limits Including Systematic Uncertainties

The case of evaluating 95% confidence levels in the presence of systematic and statistical errors is discussed in the appendix. There it is shown that if we introduce an uncertainty $\sigma_s$ on the number of signal events which should pass our cuts, then we find that $N_{95}(n_0) \longrightarrow N_{95}(n_0; \sigma_s)$, as given by Equations A.5 and A.11. Here $n_0$ is the number of events observed. These expressions are solved numerically for $N_{95}$ using $n_0$ (in this case zero), and the overall uncertainty $\sigma_s$ which we now proceed to evaluate.

In estimating our systematic and statistical errors we consider each of the following:

- Uncertainty in choice of jet energy correction scheme
- Structure function choice
- Statistical Uncertainty from generating finite Monte Carlo samples
- Uncertainty in the integrated luminosity $\mathcal{L}$ for the data set

Jet Energy Correction Scheme

In attempting to measure the energy of a jet several sources of systematic error arise. Any uncertainty in the measured jet energy translates into an uncertainty in our event acceptance since we explicitly make a cut on jet $E_T$. At the lowest leptoquark masses considered (45-GeV), the mean jet $E_T$ and the $E_T$ cutoff roughly coincide. This means that any small shift in our jet energy definition produces much larger changes in the event acceptance for the $E_T$ cut. We find that at low leptoquark masses this turns out to be by far the dominant source of error in our event acceptance. The uncertainty becomes smaller as $< E_T^{\mathrm{jet}} > - E_T^{\mathrm{min}}$ increases, and is only a minor effect at $M_{LQ} = 125$ GeV.

In our analysis we consider the following sources of uncertainty in our measured jet energy

- Absolute Jet energy scale uncertainties.

- Unknown losses of jet energy outside of the clustering cone.
- Unknown additive contributions from the underlying event.

These are estimated using our Monte Carlo leptoquark samples and a CDF detector simulation.

Firstly the absolute jet energy scale is varied by $\pm 5\%$ from its default value in the energy correction routine. As we increase the energy scale, jet $E_T$'s are pushed higher giving us an increased number of events which survive the kinematic cuts. Similarly, we find that our acceptance decreases at lower jet energy scales. At $M_{LQ} = 45$ GeV we find the cut acceptance changes by around $\pm 12\%$ for $\pm 5\%$ changes in scale. At $M_{LQ} = 125$ GeV the uncertainty is only around $\pm 1.5\%$.

An out of cone correction adds energy back into the jet. Since the jet is clustered in a finite-size cone, it is possible that we miss energy that has fallen outside of the cone radius. Correcting for this effect increases our acceptance.

Finally in performing an underlying event correction we are subtracting energy out of the jet cone, energy which we assume is coming from the soft processes which make up the underlying event. This correction effectively lowers the jet energy and hence the acceptance.

From these qualitative arguments we expect our event acceptance to be highest for

- Jet energy scale = 1.05 x default
- No underlying event subtraction
- Out of cone energy correction done

and to be lowest for

- Jet energy scale = 0.95 x default
- Underlying event subtraction done
- No out of cone energy correction done



This is indeed found to be the case. We write the relative error in the acceptance due to jet energy correction effects as follows

$$\Delta A_J = \frac{A_J^{hi} - A_J^{lo}}{A_J^{hi} + A_J^{lo}} \tag{6.24}$$

As we have already pointed out, this systematic uncertainty depends upon the mass of the leptoquark. The uncertainties due to choice of jet energy correction scheme are evaluated for all leptoquark masses considered and are given in the following table:

| $M_{LQ}$ (GeV) | 45 | 65 | 85 | 105 | 125 |
|---|---|---|---|---|---|
| $\Delta A_J$ (%) | 26.1 | 15.5 | 8.2 | 5.4 | 3.6 |

Table 6.14: Relative Uncertainties in Event Acceptances from Varying the Jet Energy Correction Scheme.

Structure Functions, Statistical Errors, and Electron Quality Cuts

By using different structure functions in our leptoquark Monte Carlo we produce different geometric distributions for the final state electrons and jets. Since we explicitly impose fiducial cuts on the electrons, this in turn leads to changes in our event acceptance. To estimate the size of the uncertainty we generate several thousand events at each leptoquark mass for each of the following structure functions, using the notation of [39].

- HMRSB-190
- EHLQ2
- KMRS-B0
- M&T Set-1

The geometric acceptances are then recalculated as in Section 6.4.1. We denote the highest acceptance obtained by $A_G^{hi}$ and the lowest by $A_G^{lo}$. The absolute spread in acceptances is then given by

$$2\Delta A_G = A_G^{hi} - A_G^{lo} \tag{6.25}$$

Before calculating the relative uncertainty we first evaluate the error on the error! Associated with each acceptance $A_G^{hi}, A_G^{lo}$ is a statistical error due to generating a finite number of events in our Monte Carlo data samples. There are also systematic uncertainties in the measurement of the electron quality cut efficiencies which were presented in Section 6.6. Using the form

$$A = \frac{N_{CC}\varepsilon_c^2 + N_{CP}\varepsilon_c\varepsilon_p + N_{CF}\varepsilon_c\varepsilon_f}{N_{GEN}} \tag{6.26}$$

for the geometric acceptance we can find the appropriate spread $\sigma_A$ due to errors in $\varepsilon_x$ and $N_{Cx}$. The error on $\Delta_G$ is therefore taken to be $\sqrt{\sigma^2_{A_G^{hi}} + \sigma^2_{A_G^{lo}}}$. We then obtain relative errors on the geometric acceptance, which include structure function choice, statistical, and electron quality uncertainties, and these are shown in Table 6.15.

| $M_{LQ}$ (GeV) | 45 | 65 | 85 | 105 | 125 |
|---|---|---|---|---|---|
| $\Delta A_{SF,STAT,ELE}$ (%) | 12.3 | 10.1 | 6.6 | 6.9 | 4.6 |

Table 6.15: Combined Statistical Errors and Uncertainties From Structure Function Choice and Electron Selection Cut Efficiencies.

Integrated Luminosity Uncertainty

The uncertainty on the size of data sample has been found to be ±7%, as is described in detail in [57]. Obviously this is independent of leptoquark mass.

Combined Errors

To summarize, we have estimated the following sources of error on our event acceptances:

- Jet energy correction scheme: Mass dependent. 26.1%-3.6% for $M_{LQ}$ = 45 – 125 GeV
- Combined statistics, structure function choice, and electron selection cut efficiency: Mass dependent 12.3%-4.2% for $M_{LQ}$ = 45 – 125 GeV
- Integrated Luminosity: 7%



Adding these uncertainties in quadrature we obtain the following mass-dependent systematic errors:

| $M_{LQ}$ (GeV) | 45 | 65 | 85 | 105 | 125 |
|---|---|---|---|---|---|
| All Errors (%) | 29.7 | 19.8 | 12.6 | 11.2 | 9.1 |

Table 6.16: Combined Statistical and Systematic Errors.

Using the combined systematic and statistical errors found above we now obtain values for $N_{95}(\sigma_s)$. These are summarized in the following table:

| $M_{LQ}$ (GeV) | A (%) | $\sigma_s$(%) | $N_{95}$ | $N_{LO}(x = 100\%)$ | $K \cdot N_{LO}(x = 100\%)$ |
|---|---|---|---|---|---|
| 45 | 1.6 | 29.7 | 3.54 | 39.1 | 50.8 |
| 65 | 6.6 | 19.8 | 3.20 | 25.3 | 31.9 |
| 85 | 10.7 | 12.6 | 3.07 | 10.7 | 12.9 |
| 105 | 15.2 | 11.2 | 3.05 | 4.3 | 5.0 |
| 125 | 18.5 | 9.1 | 3.03 | 1.8 | 2.0 |

Table 6.17: Event Acceptances, Systematic Uncertainties $\sigma_s$, and the 95% Upper Confidence Levels on the Number of Events in the Data. Also Shown are the Number of Events Expected at x= 100% With and Without Higher-Order Corrections.

We now present in Table 6.18 our final results for the $e^+e^-$+dijet channel, obtained using

$$\sigma \cdot x^2(95\%CL) < \frac{N_{95}}{\mathcal{L} \cdot A}$$

and

$$x^2(95\%CL) < \frac{N(95\%CL)}{N(\mathrm{MC}; x = 100\%)}.$$

| $M_{LQ}$ (GeV) | $\sigma \cdot x^2$(95% CL)(pb) | $x$(95% CL) LO | $x$(95% CL) NLO |
|---|---|---|---|
| 45 | 54.6 | 0.30 | 0.26 |
| 65 | 12.0 | 0.36 | 0.32 |
| 85 | 7.1 | 0.56 | 0.49 |
| 105 | 5.0 | 0.85 | 0.78 |
| 125 | 4.0 | 1.30 | 1.23 |

Table 6.18: Final Limits At 95% CL on $\sigma \cdot x^2$ and $x = BR(LQ \rightarrow e + u)$. Results With and Without the Higher-Order K-Factor Are Given.The $x$ Limits Assume the ISAJET Cross Section Evaluated with HMRS-B Structure Functions.

These results are also presented graphically in Figures 6.20 and 6.21 respectively, and from either figure we can extract the following mass limits assuming $\sigma$(ISAJET) and $x = 100\%$:

$$M_{LQ} > 113 \text{ GeV at } 95\% \text{ CL using } \sigma(\text{LO}) \tag{6.27}$$

and

$$M_{LQ} > 116 \text{ GeV at } 95\% \text{ CL using } K \cdot \sigma(\text{LO}) \tag{6.28}$$

As Figure 6.21 shows, we are relatively insensitive to leptoquark pair production in this channel for small values of $x$, while our highest mass limits are obtained at $x = 100\%$. This is precisely what we expect since $N_{EV} \propto x^2$ in this channel. A more sensitive avenue for exploring the possibilities of leptoquarks with intermediate and low values of $x$ is provided by the $e^{\pm}\nu_e$+dijet channel and this is the subject of our second major analysis which is presented in the next chapter.



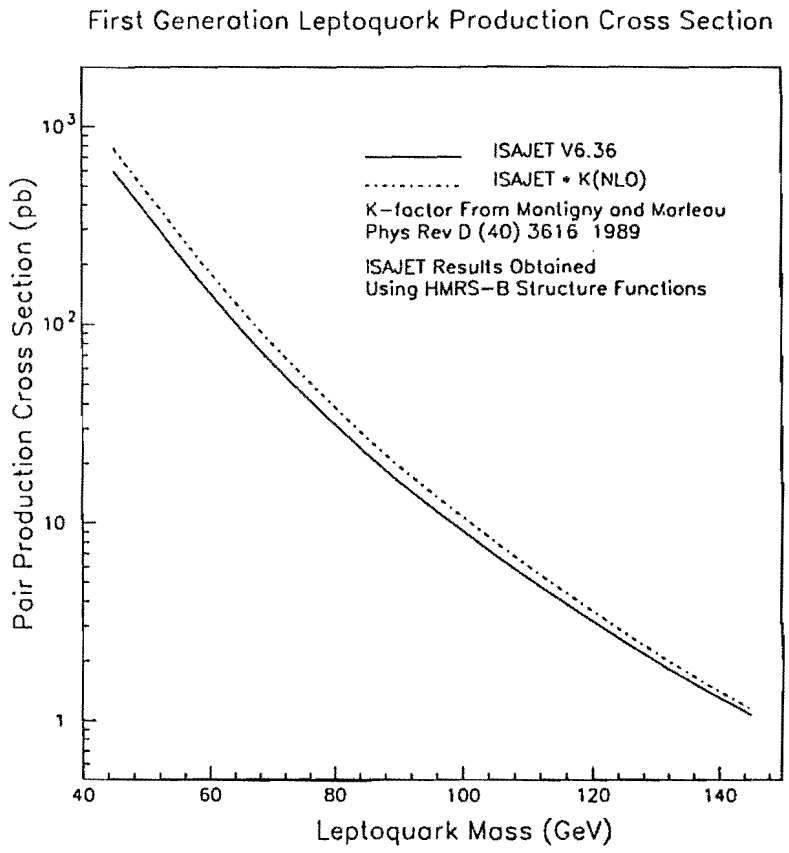


Figure 6.1: ISAJET Leptoquark Pair Production Cross Section as a Function of Leptoquark Mass.

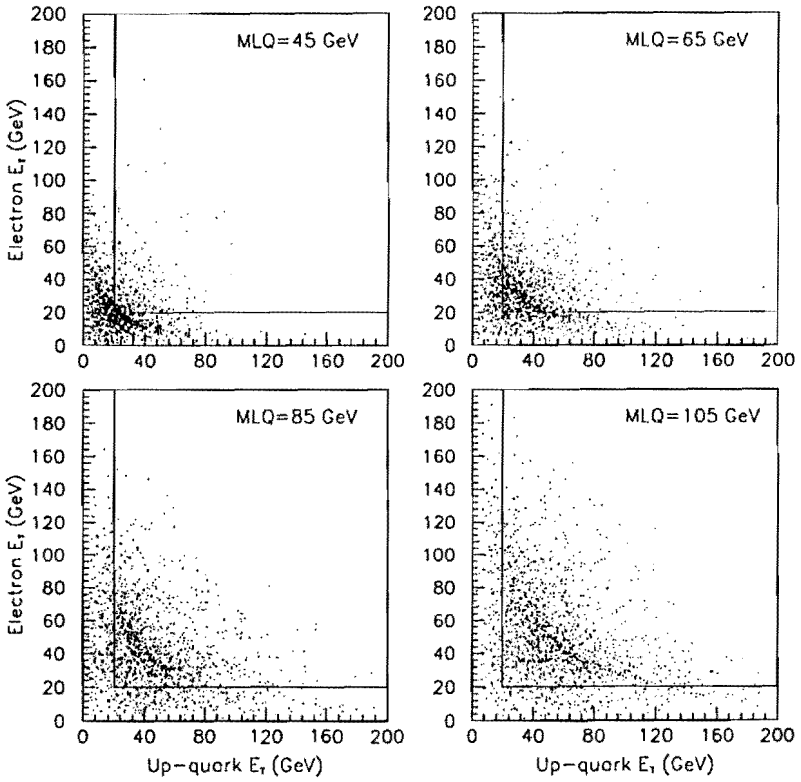


Figure 6.2: Parton-Level Monte Carlo $E_T$ Distributions for Electrons and Up-Quarks Emerging from the Decay of One of the Leptoquarks in $LQ\overline{LQ}$ Events. Also Indicated is the Effect of an $E_T > 20$-GeV Cut.



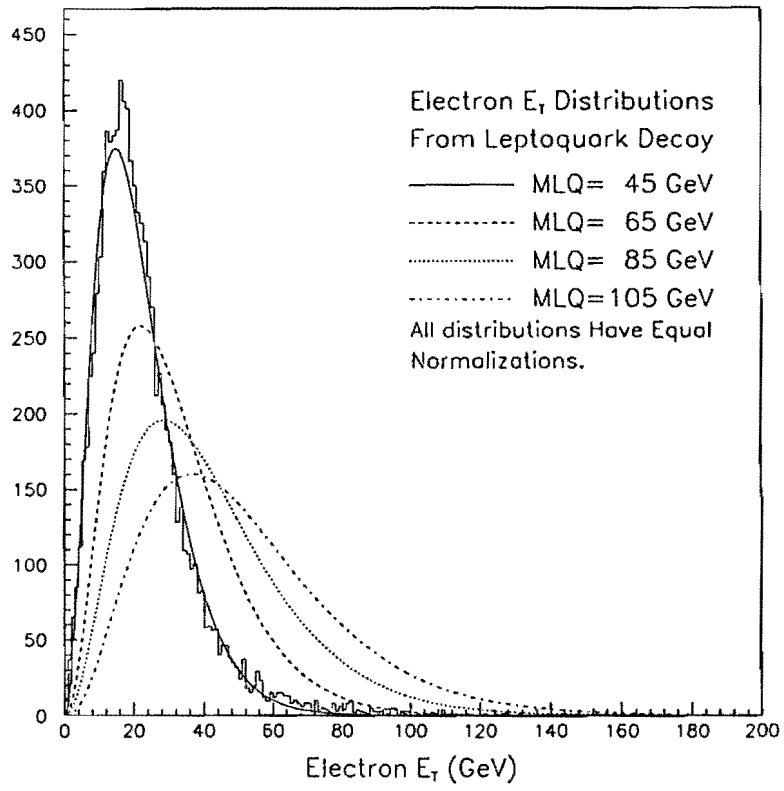


Figure 6.3: Parton level $E_T$ Spectra for LQ-Decay Electrons in $LQ\overline{LQ}$ Events for Four Different Leptoquark Masses. For Figure Clarity We Use Fitted Distributions and Illustrate the Fit Quality Using $M_{LQ} = 45$ GeV.

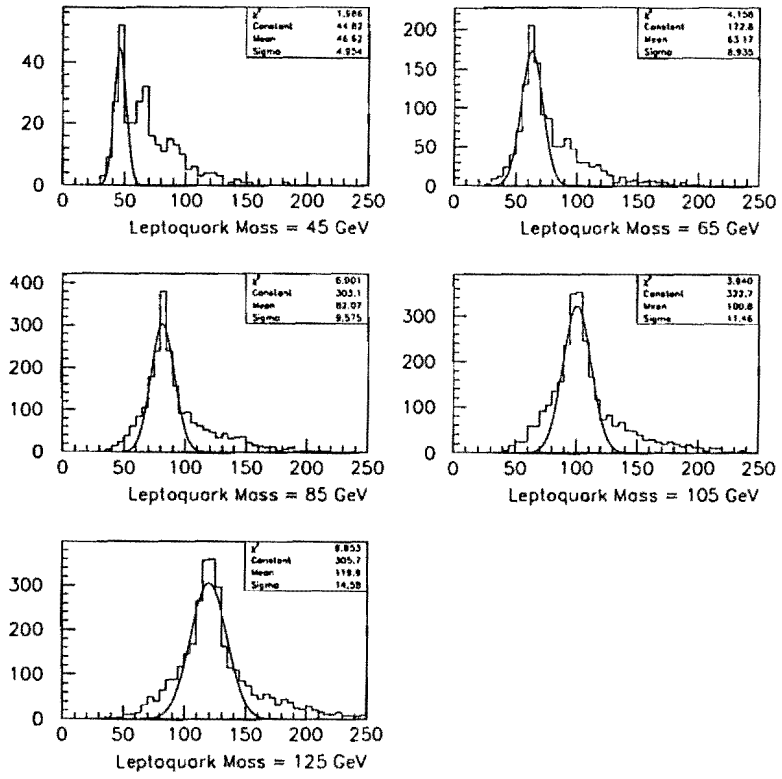


Figure 6.4: Resolution of Reconstructed Leptoquark Mass using Randomly Chosen Electron-Jet Combinations (see text). The Curves are Gaussian Fits to the Mass Peak.



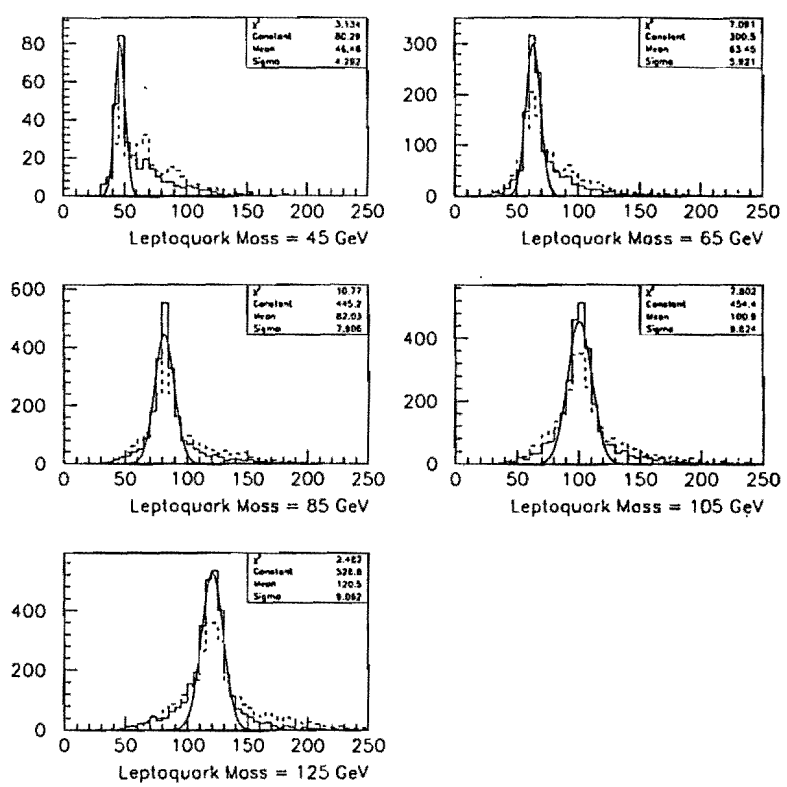


Figure 6.5: Resolution of the Reconstructed Leptoquark Mass Using $\Delta M$ Algorithm (*Solid*) and Randomly Chosen Electron-Jet Pairs (*Dashed*). Also Shown are Gaussian Fits to the $\Delta M$ Peak.

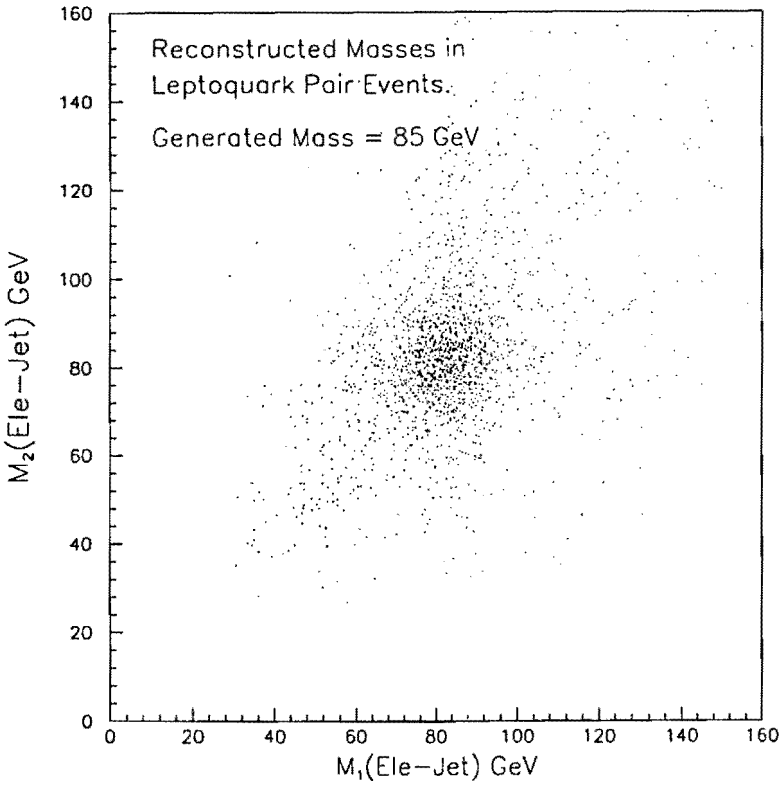


Figure 6.6: Reconstruction of Both Leptoquark Masses in 85-GeV $LQ\overline{LQ}$ Events After CDF Detector Simulation.



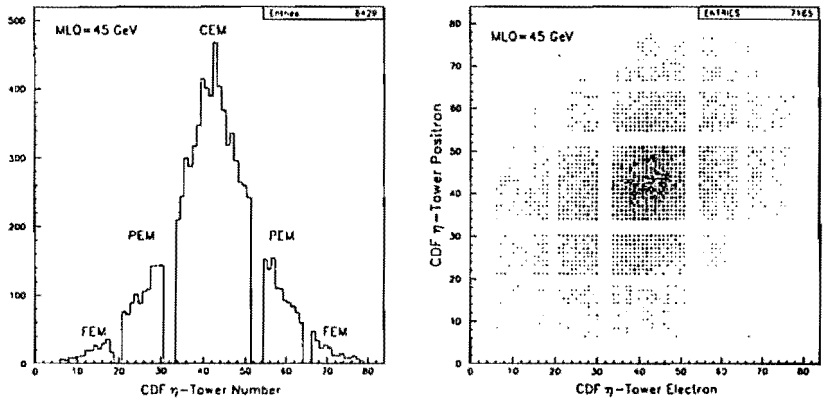


Figure 6.7: $\eta$-Tower Distribution For One(Both) Electron(s) in 45-GeV $LQ\overline{LQ}$ Events. Electrons Failing $\eta$-Tower Fiducial Cuts Have Been Removed.

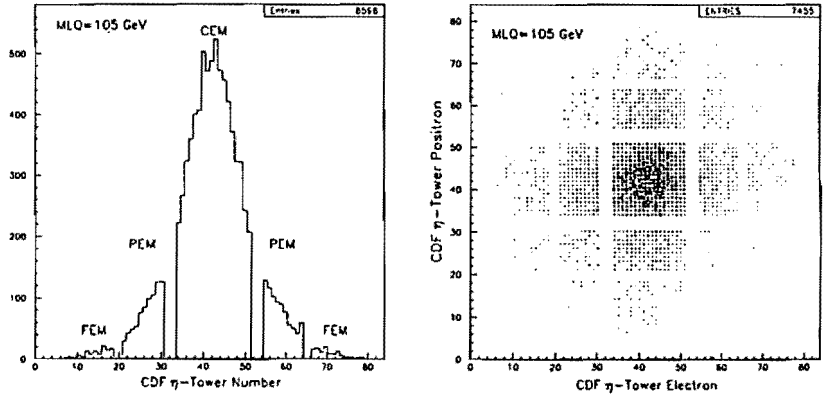


Figure 6.8: $\eta$-Tower Distribution For One(Both) Electron(s) in 105-GeV $LQ\overline{LQ}$ Events. Electrons Failing $\eta$-Tower Fiducial Cuts Have Been Removed.

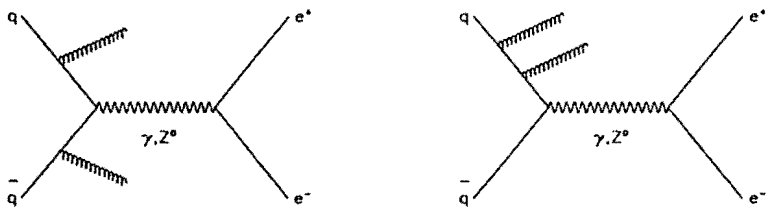


Figure 6.9: Higher-Order QCD Processes Contributing to the $\gamma, Z^0 + 2$jet Background.

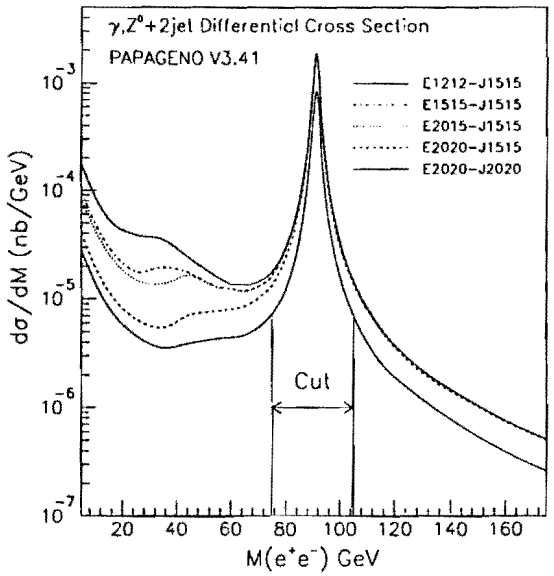


Figure 6.10: Differential Cross Section for $\gamma, Z^0 + 2$Jet Events From PAPAGENO. Different Curves Correspond to Different Choices of $E_T$ Cuts on Electrons and Jets.



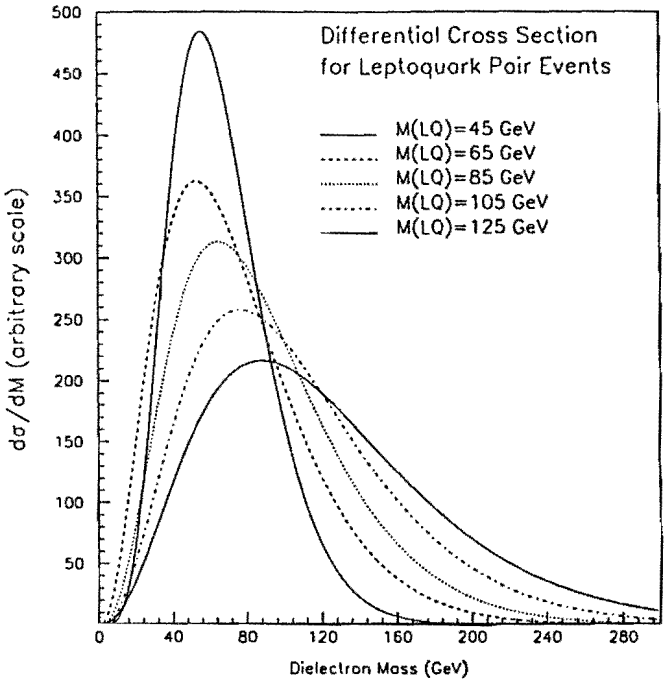


Figure 6.11: Dielectron Mass Distributions for ISAJET Leptoquark-Pair Events After CDF Detector Simulation. Five Different Leptoquark Masses Are Shown. All Curves Are Normalized to the Same Area.

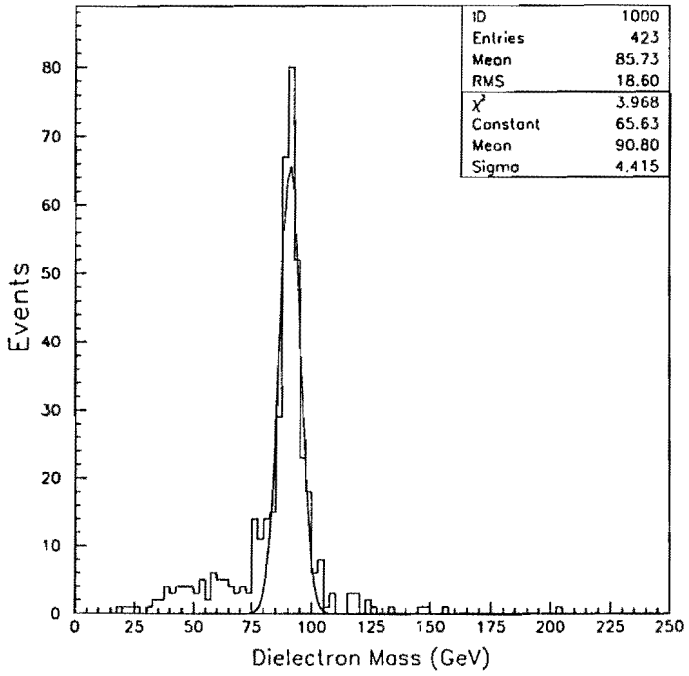


Figure 6.12: Dielectron Invariant Mass Spectrum for the 423 Events Found in the CDF Inclusive Electron Data Set. Also Shown is a Gaussian Fit to the Mass Peak Over the Range $80 < M_{ee} < 100$ GeV.



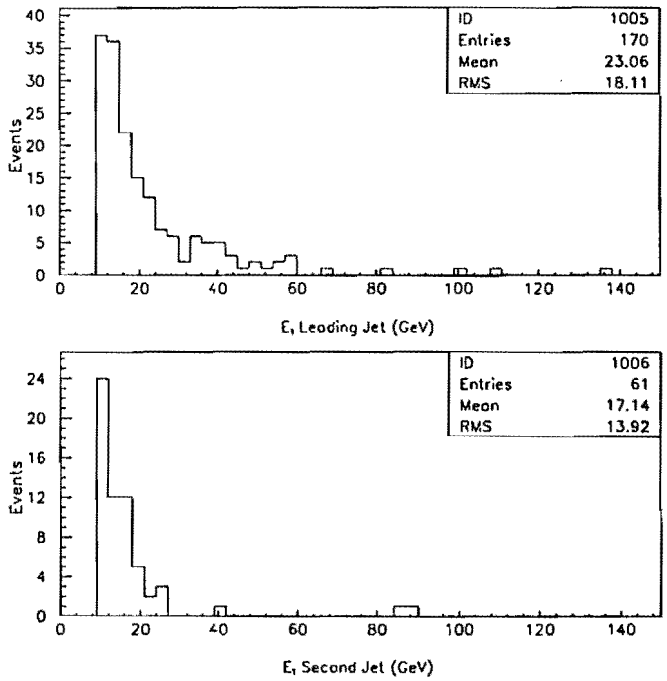


Figure 6.13: The $E_T$ Spectra For Any Additional Jets In The 423 Dielectron Events Shown in the Previous Figure. There Are 170 Events With At Least One Jet Passing $E_T > 10$ GeV, and 61 Events With Two Such Jets.

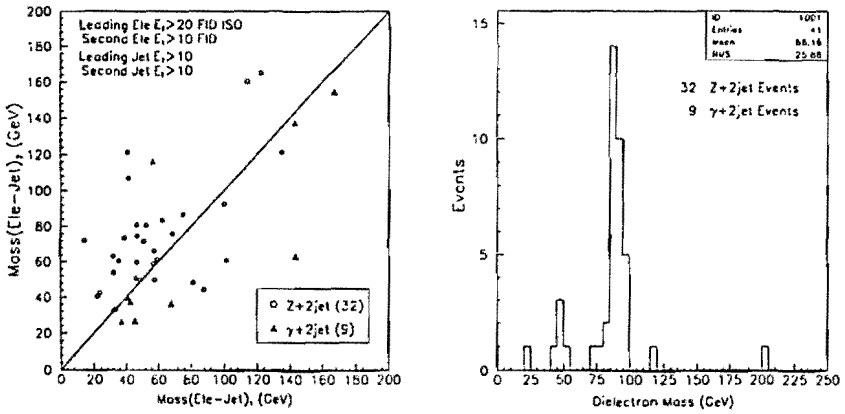


Figure 6.14: Electron-Jet and Dielectron Masses in CDF $e^+e^-$+Dijet Data for Low $E_T$ Thresholds. $ISO_4$(2nd Electron) is Unrestricted. Events Are Denoted $\gamma$ or $Z^0$ for $M(e^+e^-)$ Outside or Inside the Range 75-105 GeV Respectively.

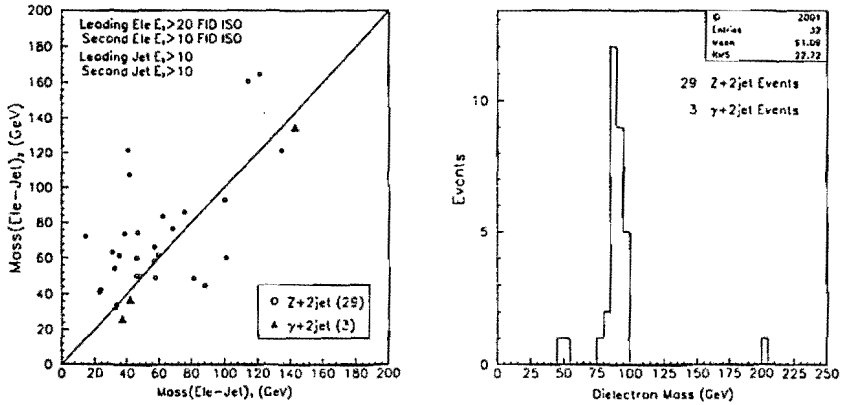


Figure 6.15: As in the previous figure but with tight $ISO_4 < 0.1$ cuts on both electrons.



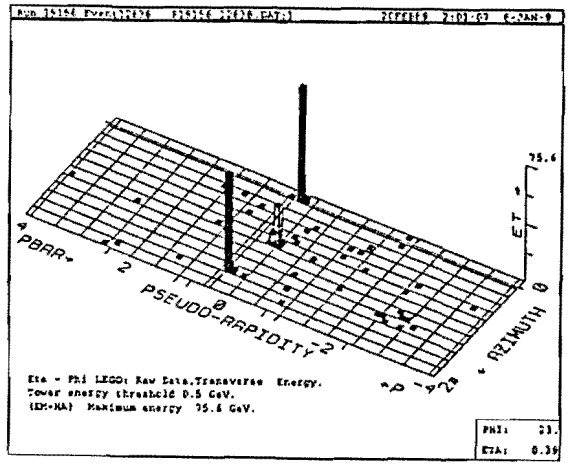


Figure 6.16: Calorimeter Lego Display of a Candidate $Z^0$ + 1jet Event.

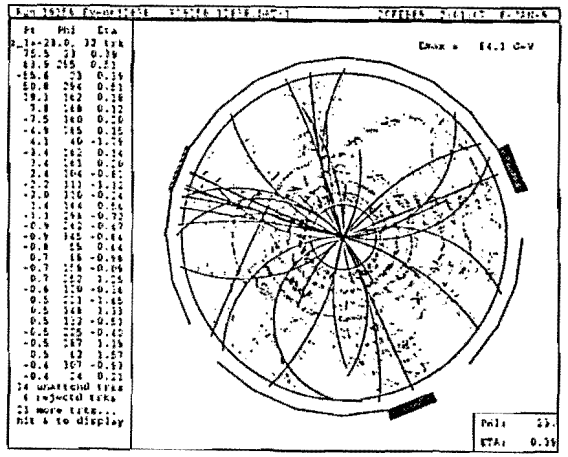

Figure 6.17: CTC Display of the Same $Z^0$ + 1jet Candidate.

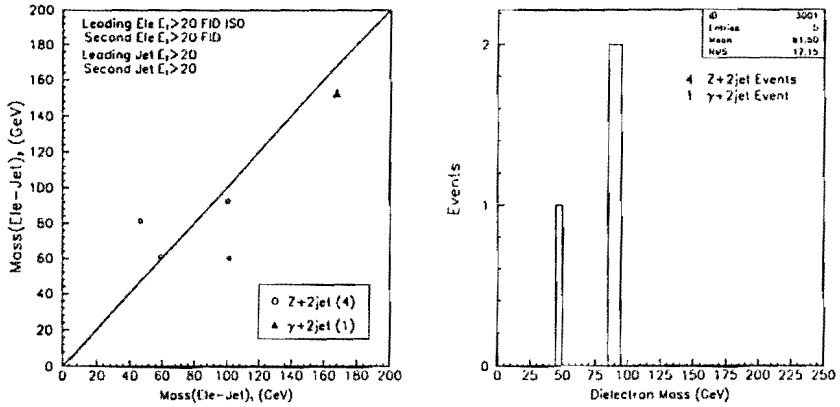


Figure 6.18: Electron-jet and dielectron masses in CDF $e^+e^-$+dijet data for high $E_T$ thresholds. $ISO_4$(2nd electron) is unrestricted. Events are denoted $\gamma$ or $Z^0$ for $M(e^+e^-)$ outside or inside the range 75-105 GeV respectively.

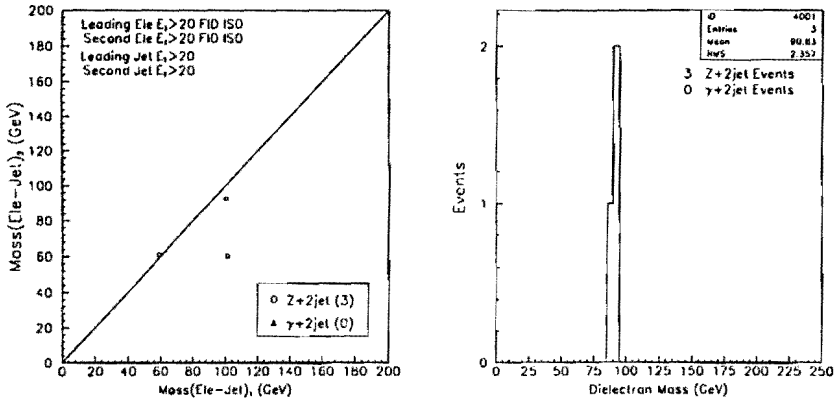


Figure 6.19: As in the previous figure but now requiring $ISO_4 < 0.1$ for both electrons



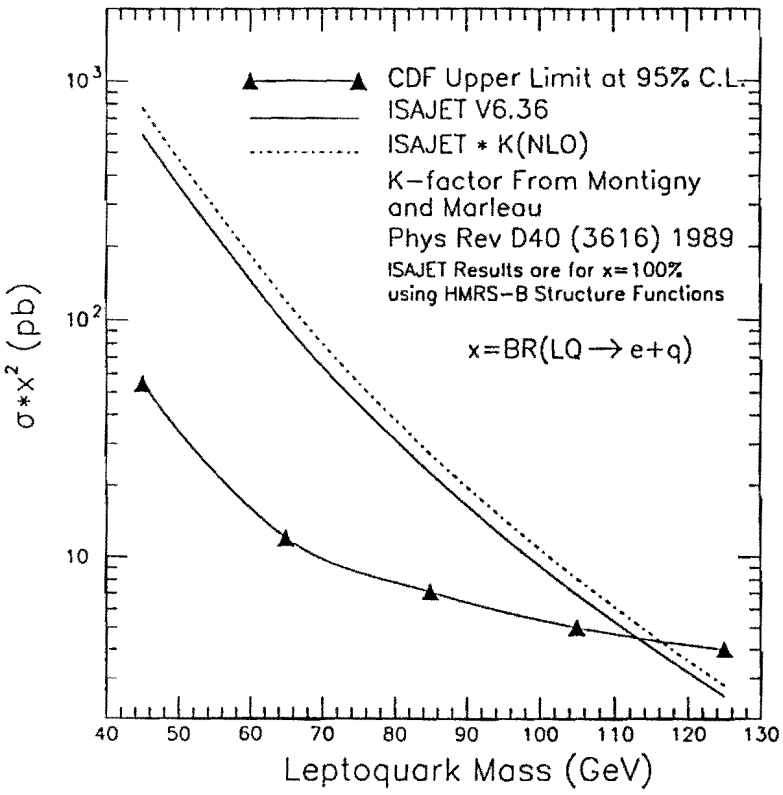


Figure 6.20: Upper Limits on the leptoquark pair production cross section $\sigma(M_{LQ}) \cdot x^2$ from the dielectron+dijet channel at 95% CL. Results Are Compared to the ISAJET Monte Carlo Production Cross Section, Shown With and Without Higher-Order QCD Corrections

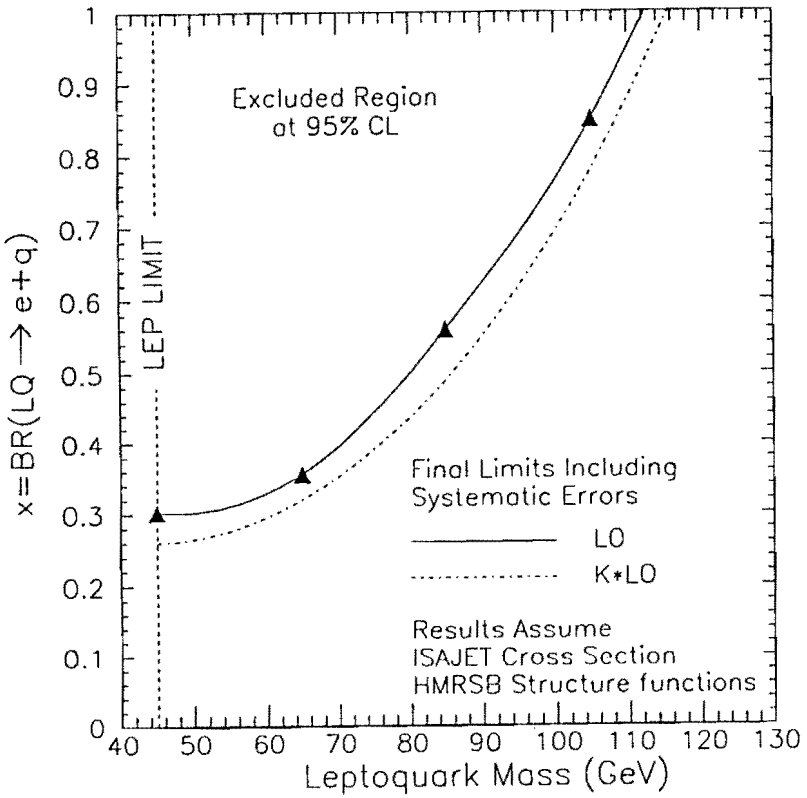


Figure 6.21: Final limits on the leptoquark mass vs. $x = BR(LQ \rightarrow e + u)$ from the dielectron+dijet channel. Results assume the Monte Carlo production cross section and are shown with and without higher-order QCD corrections.



# Chapter 7

# A Search For Leptoquarks In The $e^{\pm}\nu_e$+Dijet Channel

## 7.1 Overview Of The Analysis

This chapter describes a search for the process

$$\bar{p}p \longrightarrow LQ_1\overline{LQ}_1 + X \longrightarrow (eu)(\nu_e d) + X, \tag{7.1}$$

again using the 1988-89 CDF inclusive central-electron data set.

We start in Section 7.2 with a short motivational discussion of what can be gained from this analysis, and why it complements the $e^+e^-$+dijet search presented in the previous chapter.

Properties of the $e^{\pm}\nu_e$+dijet signal are discussed in Section 7.3, as well as methods of reconstructing $M_{LQ}$ now that there is a neutrino in the final state. The leptoquark pair production cross section (Section 6.2) is not discussed further here since the two signal processes considered in this thesis differ only in their final state, that is, *after* the leptoquarks have decayed. For the $e^{\pm}\nu_e$+dijet analysis we will therefore use the same values of $\sigma(M_{LQ})$ that were presented in Table 6.1.

In Section 7.4 we look at the acceptances of the geometric cuts that will be applied to the data. Kinematic cuts are discussed in Section 7.5 when we describe the major source of background which can fake the $e^{\pm}\nu_e$+dijet signal. There a detailed study of both signal and background processes will be made. In Section 7.6 we explain the relative likelihood method used in our statistical separation of the signal from background. Section 7.7 presents our analysis of the $e^{\pm}\nu_e$+dijet CDF data, and finally in Section 7.8 we present the conclusions of our search for leptoquarks in this channel.

## 7.2 Motivation For The $e^{\pm}\nu_e$+Dijet Analysis

Firstly we recall that the event rate in the $e^+e^-$+dijet channel is proportional to $x^2$ where $x$ is the unknown $BR(LQ \rightarrow e + u)$. Our analysis in that channel is therefore most sensitive at $x = 100\%$, and our highest mass limits were set in this case.

The motivation for the present analysis is as follows: When compared to the $e^+e^-$+dijet channel, the $e^{\pm}\nu_e$+dijet signature has a higher rate at small and intermediate values of $x$. By doing an $e^{\pm}\nu_e$+dijet search we then greatly improve our chances of observing a signal. The $e^{\pm}\nu_e$+dijet event rate is $\sim 2x(1-x)$, and so for example with $x = 50\%$ we would expect $\sim 0.5 \cdot \sigma \cdot \mathcal{L}$ events produced in this channel, but only half as many $e^+e^-$+dijet events ($\sim 0.25 \cdot \sigma \cdot \mathcal{L}$). For $x = 30\%$, the event fractions produced in the two channels are 42% and 9% respectively.

All of this can be seen in Figure 7.1 where we show the fraction of events expected to be produced in a given channel for any value of $x$, as well as the overall fraction of events expected by considering both analyses. We note that for $x < 2/3$ we *always* expect more events produced in the $e^{\pm}\nu_e$-channel than we do in the $e^+e^-$-channel (before any acceptances/efficiencies or backgrounds are considered), and this clearly illustrates the importance of this second analysis.

## 7.3 The $e^{\pm}\nu_e$+Dijet Final State

### 7.3.1 Kinematic Expectations

In the $e^+e^-$+dijet analysis we found that the mean-$E_T$ for the up-quarks and electrons from leptoquark decay was given by $< E_T > \simeq 1/2M_{LQ}$ (Figures 6.2 and 6.3). At the parton level, $e^+e^-$+dijet and $e^{\pm}\nu_e$+dijet events from leptoquark pair production differ only in that an $(eu)$ pair is replaced by $(d\nu_e)$. In particular, the jet $E_T$ distributions should remain unchanged (in the massless quark and electron limit), as should the spectrum for the single remaining electron. Instead of a second electron-$E_T$, we now have a $\not\!\!E_T$ distribution corresponding to $E_T^{\nu}$, which also has its mean value at $< \not\!\!E_T > \simeq M_{LQ}/2$. As before, for the range of



leptoquark masses considered in this thesis, all final state electrons and jets, as well as the $\not\!\!E_T$ vector, should be well separated from each other.

Summarizing the above arguments, we expect the following properties of $e^{\pm}\nu_e$+dijet events:

- Two well separated jets with $E_T \simeq M_{LQ}/2$
- One isolated electron with $E_T \simeq M_{LQ}/2$
- Isolated $\not\!\!E_T \simeq M_{LQ}/2$

The $\not\!\!E_T$ spectrum for 45-GeV leptoquark pair events in the $e^{\pm}\nu_e$+dijet is shown in Figure 7.2 after CDF detector simulation and event reconstruction. Note that the mean of the histogram is very close to $M_{LQ}/2$ as expected. In the same figure we also show the parton-level $E_T^{\nu}$ spectrum and there is good agreement.

As before, there will be kinematic and geometric acceptances associated with any cuts made in this channel, but we postpone our presentation of these until Section 7.4, that is after we have discussed the sources of background events and the primary cuts we impose to reduce them.

### 7.3.2 Leptoquark Mass Reconstruction In $e^{\pm}\nu_e$+dijet Events

We recall that in the $e^+e^-$+dijet channel we expected two electrons and two jets in the final state. This allowed us to fully reconstruct both leptoquark masses with mass-peak resolutions on the order of $\sigma(M)/M \simeq 10\%$ (Figure 6.5). The mass-peak resolutions were limited only by the inherent energy resolution of the calorimeters, while the events in the combinatoric tails arose only because our algorithm for resolving the electron-jet pairing ambiguity was not perfect. However, as we showed, if a leptoquark signal was present in this channel we would have a reasonable chance of seeing it in the electron-jet mass spectrum.

In the $e^{\pm}\nu_e$+dijet channel, the situation is more difficult. Our final state now contains two jets and one electron. What was the second electron for the previous analysis is now a neutrino whose presence manifests itself as missing energy. Because of this there are a number of associated effects which have to

be considered and which, as we will now explain, combine to smear out the reconstructed leptoquark mass peak.

Firstly we note that while for electrons and jets we can, in principle, fully reconstruct their 4-momentum and hence the leptoquark mass, for neutrinos only the transverse components of its energy can be measured. This is because in $\bar{p}p$ collisions, the quark-antiquark or gluon-gluon hard scattering that can lead to leptoquark pair production does not in general take place in the parton center-of-mass (COM) reference frame. Since we do not measure energy lost down the beam pipe we have no idea by how much the parton COM has been boosted in the z-direction and therefore we cannot associate any measured missing energy in the z-direction with $E_z^\nu$. This has the immediate effect of lessening our ability to accurately reconstruct $M_{LQ}$ using $E(\nu), \vec{P}(\nu)$ and $E(jet), \vec{P}(jet)$ since we have lost information about one of the kinematic components used.

These statements apply whenever we try to reconstruct an invariant mass in a $\bar{p}p$ event containing a final state neutrino. Probably the most well known example of this, and one which will have serious consequences in our later attempts at removing Standard Model backgrounds, is provided by $W^\pm \to e^\pm \nu$ production. If the neutrino momentum could be accurately determined, the W-mass resolution would be comparable to that found for the $Z^0$ in $Z^0 \to e^+e^-$ events (see Figure 6.12). Instead we can only form a 'transverse mass' $M_T(W)$ using $\not\!\!E_T$ rather than the missing energy, and defined as

$$M_T^2(W \to e\nu) = 2E_T^e E_T^\nu (1 - \cos(\phi^e - \phi^\nu))$$

While the transverse mass spectrum is found to peak close to $M(W)$ it is considerably broader than the $Z^0$ peak, as is shown in Figure 7.3.

In $e^\pm\nu_e$+jet events we find even further mass-resolution degradation, and this is understood as follows: $E_T^\nu$ is inferred from the transverse energy imbalance in an event. If, for any reason, we incorrectly measure the 'observed' energy then we effectively induce a false $\not\!\!E_T$ which can add to, or decrease, the true $\not\!\!E_T$. This can happen when, for example, we do not correctly measure the energy of a jet. The worst case scenario for leptoquark mass reconstruction is that we use the



mismeasured jet energy and the false $\not\!\!E_T$ in forming $M_{LQ}$. i.e.

$$M'^2_{LQ} = (E^j + \Delta E^j + E_T^\nu + \Delta E_T^\nu)^2 - (\vec{P}^j + \Delta\vec{P}^j + \vec{E}_T^\nu + \Delta\vec{E}_T^\nu)^2$$

instead of

$$M^2_{LQ} = (E^j + E_T^\nu)^2 - (\vec{P}^j + \vec{E}_T^\nu)^2.$$

Recall that even the second expression is only an approximation to $M_{LQ}$ because of our use of $E_T^\nu$ instead of $E^\nu$. One indication that a jet energy has been grossly mismeasured is that the $\not\!\!E_T$ vector and the jet-axis are almost coincident. Imposing a $\not\!\!E_T$ isolation cut is one possible solution to this problem, though we do not do so in this thesis.

Given these qualitative arguments, there are several options in reconstructing the leptoquark mass in $e^\pm\nu_e$+dijet events:

1. Ignore $\not\!\!E_T$ completely and plot only M(Ele-Jet)$_1$ and M(Ele-Jet)$_2$.
2. Use the minimum-$\Delta M$ algorithm from Section 6.3.2 using $P_z^j = 0$ and $P_z^\nu = 0$ for any jet+MET combination.
3. Use the minimum-$\Delta M$ algorithm using the measured value of $P_z^j$ and a value for $P_z^\nu$ chosen randomly from a Gaussian distribution obtained by fitting $P_z^{ele}$.
4. Use the minimum-$\Delta M$ algorithm using the measured $P_z^j$ and $P_z^\nu = 0$

The results are shown in Figure 7.4 using 45-GeV leptoquark pair events as an example. We see that all of the above options give a reasonable leptoquark mass peak, though none are as good as the resolution obtained in the $e^+e^-$-channel, which is superimposed on the last plot for comparison. Method-4 from the list above appears to be slightly better than the other three, and will be used when we look for a leptoquark signal in the CDF data. Figure 7.5 shows the invariant mass distributions for 45, 55, 65, and 75 GeV leptoquarks reconstructed in this way, as well as Gaussian fits to the peaks.

## 7.4 Estimation Of Geometric Acceptances

In this section we show the effects of restricting the single electron in $e^{\pm}\nu_e$+dijet events to the fiducial region of the CEM calorimeter. We will not evaluate kinematic acceptances here since these are expected to be very similar to those found for $e^+e^-$+dijet events, assuming that our measurement of $\not\!\!E_T$ closely reflects the transverse energy of the leptoquark-decay neutrino; Figure 7.2 justifies this assumption.

### 7.4.1 Geometric Acceptances

Much of the work needed for this section has already been done in the $e^+e^-$+dijet channel. There, we estimated the effect of imposing fiducial cuts on both electrons in an event, and on restricting dielectron topologies to CC, CP, and CF only (see Section 6.4.1).

In this channel, estimating geometric acceptances is somewhat easier since we only have one electron to work with, and we do not restrict the $\eta$-position of the jets or $\not\!\!E_T$.

Figure 6.7 showed the effect of restricting the electron in 45-GeV leptoquark-pair events to the set of fiducial calorimeter towers, and an overall $\eta$-tower efficiency of 84% was found; this efficiency was squared when the positron was also considered. For the $e^{\pm}\nu_e$+dijet channel we can use the same 1-D plot to find the probability of observing the single electron in the Central, Plug, or Forward regions after the $\eta$-tower cut has been made. These acceptances for 45-GeV and 105-GeV leptoquarks, for example, are shown in Table 7.1. We see that we do not incur a heavy loss of signal in using a *central* electron data set rather than inclusive electrons throughout the detector. For example we retain around $59/84 = 70\%$ of the 45-GeV leptoquark signal, while for $M_{LQ} = 105$ GeV this acceptance has risen to $68/86 = 79\%$.

Restricting ourselves now to the CEM, the other main geometric source of event loss in our data set is the $\phi$-crack cut, which as explained in Section 6.4.1 has an acceptance of 86.7%. Therefore by imposing the geometric requirements



that an event contain a fiducial central electron we expect the leptoquark signal to be reduced to around 50-60% of its original size for $M_{LQ} = 45 - 105$ GeV.

| | CDF Detector Region | | | |
|---|---|---|---|---|
| | Central | Forward | Plug | Total |
| $A_\eta : M_{LQ} = 45$ GeV | 58.6 % | 21.2 % | 4.4 % | 84.2 % |
| $A_\eta : M_{LQ} = 105$ GeV | 67.7 % | 16.0 % | 2.3 % | 86.0 % |

Table 7.1: Geometric $\eta$-tower acceptance $A_\eta$ for the electron in $e^{\pm}\nu_e$+dijet leptoquark events. The acceptance is shown for each CDF calorimeter region after non-fiducial towers have been excluded.

## 7.5 The $W$+2jet Background

Any Standard Model process capable of producing events containing a single high-$E_T$ isolated central electron, along with two high-$E_T$ jets and $\not\!\!E_T$, is a source of background for a leptoquark search in the $e^{\pm}\nu_e$+dijet channel. Examples of such processes, listed in roughly decreasing order of potential severity, are as follows:

- $(W \rightarrow e\nu)$ + initial state radiation.
- $(\gamma, Z^0 \rightarrow ee)$ + initial state radiation. One electron passes quality cuts, one fails, or is non-isolated, or is lost down a calorimeter crack.
- QCD-jet events containing a $\gamma$-conversion (Section 7.5.4).
- Heavy quark production $(b\bar{b}, t\bar{t})$.

In the absence of a large leptoquark signal, $W + 2$jet production is expected to completely dominate our $e^{\pm}\nu_e$+multijet data sample, and as we will show when we consider the CDF data in Section 7.7, this is indeed found to be the case. Because of this we will spend the majority of this section discussing $W + 2$jet events and will only briefly outline the properties of other possible backgrounds. Further detailed examination will, of course, be necessary should we observe a clear excess of events incompatible with $W$ production.

### 7.5.1 Comparing $W + 2$jet and $\gamma, Z^0 + 2$jet Production

$W$+multijet production is very similar to the analogous case of the $Z$+multijet background for the $e^+e^-$+dijet analysis, and much of what we discussed in the previous chapter also applies here. For example, the $W$ + 2jet cross section is expected to fall steeply with both the number and the $E_T$ of partons radiated in the initial state.

In the $e^+e^-$+dijet channel it was found that the $\gamma, Z^0$+2jet background could be effectively eliminated by imposing a dielectron-mass cut to remove the dominant $Z^0$ peak. In the $e^{\pm}\nu_e$+dijet channel, however, we are in a substantially worse position since (1) the W cross section is much larger: $\sigma(W)/\sigma(Z) \simeq 10$, and (2) invariant mass cuts are far less efficient at reducing $W \rightarrow e\nu$ events than they are for $Z \rightarrow ee$. Expanding on each of these points in turn:

$\sigma(W + 2\text{jet}) \gg \sigma(Z + 2\text{jet})$

The effective cross section for the process $\bar{p}p \rightarrow (W \rightarrow e\nu)$+2jet is expected to be an order of magnitude larger than that for $\gamma, Z^0$+2jet production. This follows from the fact that at $\sqrt{s} = 1.8$ TeV

$$\frac{\sigma(\bar{p}p \rightarrow W^{\pm}X)}{\sigma(\bar{p}p \rightarrow Z^0X)} \simeq 3.23, \tag{7.2}$$

and

$$\frac{BR(W \rightarrow e\nu)}{BR(Z \rightarrow ee)} \simeq 3.16 \tag{7.3}$$

as is shown in [57] and the references therein.

From these relations, and assuming that

$$\frac{\sigma(W^{\pm})}{\sigma(Z^0)} \simeq \frac{\sigma(W^{\pm} + \text{njet})}{\sigma(Z^0 + \text{njet})}, \tag{7.4}$$

we therefore expect $3.23 \times 3.16 \simeq 10.2$ times more $W$+2jet events per 4.05 pb$^{-1}$ than we do $Z$+2jet events. Furthermore, the maximum possible event rate for the $e^{\pm}\nu_e$+dijet signal is only 50% of that attainable in the $e^+e^-$+dijet channel ($x^2$ versus $2x(1-x)$). It would therefore appear that relative to a leptoquark signal, we can have as much as 20× more background in this channel than in the previous one.



$\Delta M_T^{e\nu} \gg \Delta M^{ee}$

Another property of the $W + 2$jet background which contributes to the difficulty in removing it is the fact that the $M_T^{e\nu}$ distribution for $W \rightarrow e\nu$ events is much broader than the corresponding $M^{ee}$ distribution for $Z^0$ decay (we characterize the associated widths by $\Delta M$). This is clearly visible in Figure 7.3. Based on this we conclude that significant reduction of the W+2jet background can be obtained only by eliminating a large range of $M_T^{e\nu}$, at the associated expense of a severe loss of signal. This was the approach favored by UA2 who removed all events with $60 < M_T^{e\nu} < 90$ GeV. In Table 7.2 we show the effects of applying the same cut to our data by presenting the fraction of surviving leptoquark signal and $W + 2$jet background. For comparison we also show the fraction of $e^+e^-$+2jet events from the previous analysis which are accepted after a comparable $M^{ee}$ cut.

| | Leptoquark Mass (GeV) | | | | | | Background | |
|---|---|---|---|---|---|---|---|---|
| Cut (GeV) | 45 | 55 | 65 | 75 | 85 | 105 | $W$+2jet | $\gamma, Z^0$+2jet |
| $60 < M_T^{e\nu} < 90$ | 63.7 | 63.2 | 63.3 | 63.3 | - | - | 62.4 | N/A |
| $75 < M^{ee} < 105$ | 75.6 | - | 76.3 | 74.6 | 73.5 | 75.7 | N/A | 85.6 |

Table 7.2: Fraction (%) of signal events in the $e^{\pm}\nu_e$+dijet ($e^+e^-$+dijet) surviving a cut on $M_T^{e\nu}$ ($M^{ee}$). The efficiency for $W, Z$+2jet background removal is also shown. A '-' indicates the cut efficiency was not studied for this value of $M_{LQ}$.

Conclusions of the Comparison

We have shown that based on cross section arguments alone, $W + 2$jet production is likely to be a more serious background to our signal than was the dominant $\gamma, Z^0$+2jet background for the previous analysis. If $W + 2$jet events could be efficiently removed this would not pose a serious problem. However, this is found not to be the case. Table 7.2 showed that a cut on $M_T^{e\nu}$ in this channel removes less background and more signal than did a cut on $M^{ee}$ in the previous analysis.

To find signs of leptoquark production in this channel in the presence of such a large background we will be forced to rely on the presence of a relatively large signal. This in turn limits our sensitivity to relatively low values of $M_{LQ}$. A preliminary study showed that in the $e^{\pm}\nu_e$+dijet channel we are restricted to $M_{LQ} < 75$ GeV or so at $x = 50\%$, where the rate for this channel is maximum.

This limited sensitivity will become evident when we analyse the CDF data.

### 7.5.2 Comparing $W$ + 2jet and $LQ\overline{LQ}$ Production

We now perform a detailed comparison of leptoquark and $W$ + 2jet events using Monte Carlo data samples. This will, perhaps, identify other kinematic variables which are more efficient at discriminating signal from background than is $M_T^{e\nu}$ alone.

To create $W$ + 2jet Monte Carlo event samples we use the VECBOS Monte Carlo event generator [69]. VECBOS is very similar to PAPAGENO, used in the previous analysis to evaluate the $\gamma, Z^0$ cross section. We again use HMRSB structure functions, and which are evaluated at a QCD scale of $Q = P_T^W$. At this stage we also generate several other $W$ + 2jet data sets using different choices for both the $Q$-scale and structure function parameterizations. These samples will be used later when we estimate the sensitivity of our results to such choices.

Since we now wish to consider the detailed properties of the $W$ + 2jet final state, and not just the production cross section, we unweight the event samples and pass them through CDF detector simulation and full event reconstruction. The final number of unweighted events in each data set is between 8300 and 19800, depending on the particular sample. The default $W$+2jet data set contains around 9500 events.

For the leptoquark samples we again use ISAJET. Based on the results of the preliminary study, we restrict ourselves to $M_{LQ}$ = 45, 55, 65, and 75 GeV only. For each mass we generate 10000 signal events, a number statistically comparable to the 9500 or so events in the default background sample.

Based on our expectations for the signal (Section 7.3.1), we require both leptoquark and $W$ + 2jet events to contain exactly one fiducial central electron with corrected $E_T$ > 20 GeV, and that there be at least 20 GeV of $\not\!\!E_T$ in the event. Since neither of these cuts is expected to significantly reduce the W+2jet signal, we furthermore require at least two jets anywhere in the CDF detector with $E_T$ > 15 GeV and electromagnetic fraction EMF< 95%. This last cut is applied



here to match those used later in our analysis of the CDF data, and its purpose will be to remove $e^+e^-$+1jet events where one electron failed quality cuts and was therefore identified as a jet. Finally, events in which the electron passes the CDF conversion filter are removed. The final numbers of Monte Carlo events for the leptoquark and W+2jet data samples are summarized in Tables 7.3 and 7.4 respectively.

| LQ Mass | Structure Function | $\sigma$(pb) | $N_{PASS}$ | N(4.05 pb$^{-1}$) |
|---|---|---|---|---|
| 45 GeV | HMRSB-190 | 595.5 | 836 | 81.7 |
| | DO-LO | 582.0 | 805 | 76.7 |
| | EHLQ-II | 703.3 | 809 | 93.4 |
| 55 GeV | HMRSB-190 | 224.6 | 1536 | 56.6 |
| | DO-LO | 212.9 | 1516 | 53.0 |
| | EHLQ-II | 256.0 | 1614 | 67.8 |
| 65 GeV | HMRSB-190 | 94.5 | 2301 | 35.7 |
| | DO-LO | 91.4 | 2221 | 33.4 |
| | EHLQ-II | 107.7 | 2236 | 39.5 |
| 75 GeV | HMRSB-190 | 44.3 | 2866 | 20.8 |
| | DO-LO | 41.8 | 2927 | 20.0 |
| | EHLQ-II | 50.0 | 2844 | 23.4 |

Table 7.3: Leptoquark samples for the $e^{\pm}\nu_e$+Dijet analysis after $E_T$, $\not\!\!E_T$, fiducial, and isolation cuts. All samples originally contained 10000 events.

The cross sections given in the tables are reported by the event generators for the set of primary kinematic cuts requested. For the VECBOS samples these are (1) $E_T > 10$ GeV for all final state partons, (2) $\Delta R^{jj} > 0.7$, and (3) $\eta_{e,\nu} < 1.5, \eta_{jet} < 3.5$. By combining all cut efficiencies we are able to obtain the number

| Structure Function | QCD-Scale | $\sigma$ (pb) | Unweighted Events | $N_{PASS}$ | N(4.05 pb$^{-1}$) |
|---|---|---|---|---|---|
| HMRSB-190* | $< P_T >$ | 202.1 | 9517 | 1638 | 114.2 |
| HMRSB-190 | Total M | 83.9 | 19767 | 3400 | 47.4 |
| HMRSB-190 | $M_W$ | 118.7 | 17343 | 3137 | 70.5 |
| DO-LO | $< P_T >$ | 192.5 | 9578 | 1591 | 105.0 |
| EHLQ-II | $< P_T >$ | 191.7 | 8602 | 1332 | 97.5 |
| DFLM | $< P_T >$ | 183.2 | 8317 | 1275 | 92.2 |

* Default

Table 7.4: $W$ + 2jet samples for the $e^{\pm}\nu_e$+dijet analysis after $E_T$, $\not\!\!E_T$, fiducial, and isolation cuts.

of events expected in the CDF data set. For example, with the default $W$ + 2jet sample, VECBOS predicts the following number of events:

$$\mathrm{N} = 202.1\mathrm{pb} \cdot 4.05\mathrm{pb}^{-1} \cdot \frac{1638}{9517} \cdot 95.44\% \cdot 87.3\% \cdot 97.3\% = 114.2 \qquad (7.5)$$

In Equation 7.5 the last three efficiencies are those for the Z-vertex cut, electron quality cut, and level-2 central-electron trigger respectively. Use of the last efficiency is perhaps a little conservative since with large $\not\!\!E_T$ and two jets, the event may well pass an alternate trigger.

Using the default 45-GeV leptoquark sample, we expect *at most*

$$\mathrm{N} = 595.5\mathrm{pb} \cdot 4.05\mathrm{pb}^{-1} \cdot \frac{836}{10000} \cdot 95.44\% \cdot 87.3\% \cdot 97.3\% \cdot 1/2 = 81.7 \qquad (7.6)$$

events. The factor of $1/2$ is from the $2x(1-x)$ branching ratio using $x = 1/2$. We note that for any value of $x$ different from $1/2$, the numbers of predicted events will be less than those shown in Table 7.3.

Having formed our data sets we now choose twelve distributions (not necessarily independent) which describe the overall features of the leptoquark and $W$+2jet processes. Among the obvious quantities to plot we include $E_T^e$, $E_T^{j1}$, $E_T^{j2}$, $M_T^{e\nu}$, and $\not\!\!E_T$. Others variables we consider are the dijet-mass and -transverse mass, the $\not\!\!E_T$ significance $\Xi = \not\!\!E_T/\sqrt{E_T}$, the $\phi-$separation of the two leading jets, and of the electron-MET, and finally $\cos(\theta_{j2})$ and $\mathrm{MAX}[\cos(\theta_{j1}), \cos(\theta_{j2})]$.

In Figures 7.6– 7.8 we compare these distributions for 45-GeV leptoquark pairs decaying in the $e^{\pm}\nu_e$+dijet channel, and for the $W$+2jet background. Figures 7.9-7.11 show the same distributions but for leptoquarks of mass $M_{LQ} = 75$ GeV.

From these distributions we see that no single variable cleanly separates the signal from the background. Some, such as $\not\!\!E_T$ and $E_T^e$, work well at $M_{LQ} = 45$ GeV, but have little separation power at $M_{LQ} = 75$ GeV. Others, such as $M_T^{jj}$ or $E_T^{j1}$ are good at $M_{LQ} = 75$ GeV, but do not distinguish the two processes at $M_{LQ} = 45$ GeV. The $e\nu$ transverse mass $M_T^{e\nu}$ and the $\not\!\!E_T$ significance give *reasonable* separation for all leptoquark masses considered (55-GeV and 65-GeV are not shown) and will certainly be used when we try to separate the two processes



in Section 7.6. The $\Delta\phi^{e\nu}$ separation and the $\cos(\theta^{j2})$ distributions appear to be of little use and will not be considered further.

Using one or more of these quantities, many attempts were made to create well-defined signal and background regions in some multi-dimensional variable space. However for no combination of cuts could we attain a background:signal$\ll 1$ without also seriously reducing the expected signal to less than around 2-3 events at $x = 50\%$.

### 7.5.3 Conclusions of the Leptoquark - W+2jet Comparison

Our conclusions of this study are that in the $e^{\pm}\nu_e$+dijet channel no combination of cuts on kinematic variables such as jet $E_T$, $\not\!\!E_T$ or $M_T^{e\nu}$ are able to reduce the background to reasonable levels while leaving an observable signal. Given this failure, we can either attempt a background subtraction or adopt some other method of signal-background separation. We do not consider background subtraction reliable given the large uncertainties on the $W$ + 2jet cross section, and instead we use the second approach.

In Section 7.6 we will describe a statistical separation method based on the relative likelihood that an event is due to leptoquark decay as opposed to $W$+2jet production. This has the advantages that no sweeping cuts need to be imposed, and that event-variables can be used even if they differ only slightly for the signal and background processes. Furthermore, if good separation is attainable, we can sharply reduce our reliance on the predicted $W$ + 2jet cross section since we can normalize the Monte Carlo data to the observed CDF data in regions of low expected leptoquark population, as will be shown in Section 7.7

### 7.5.4 Other Sources of Background

Before describing the relative likelihood separation of leptoquark and $W$ + 2jet processes we briefly discuss other sources of background to the $e^{\pm}\nu_e$+dijet signature.

$(\gamma, Z^0 \rightarrow e^+e^-) + 1$jet Events

The quality cuts applied to electrons in our analysis are reasonably tight, and we already know that around 13% of all isolated high-$E_T$ electrons in the fiducial region of the CEM will fail these cuts. If, in a $\gamma, Z^0 + 1$jet event, one electron fails quality or other selection requirements then it may well be identified as a high-$E_T$ jet. The event would then appear in our single-electron+2jet sample. This can happen a non-negligible number of times given that the $\gamma, Z^0 + 1$jet cross section is competitive with that for $W + 2$jet production. We note that we would not expect any significant $\not\!\!E_T$ in such events and the $\not\!\!E_T > 20$GeV cut should eliminate much of this background. However events do remain in our data but can be removed by requiring that all jets pass the cut $EMF < 95\%$. Here $EMF$ is the electromagnetic-energy fraction of the jet, making our cut approximately equivalent to $HAD/EM > 5\%$. This is just the converse of the electron selection criterion $HAD/EM < 5\%$.

$\gamma$ Conversions and $\pi^0$ Decay

$\gamma \rightarrow e^+e^-$ conversions and $\pi^0 \rightarrow \gamma e^+e^-$ Dalitz decays are relatively common at CDF. A $\gamma$ conversion can occur when a high energy photon interacts with the dense material that forms the inner wall of the central tracking chamber. For both processes, the electrons emerge with essentially zero opening angle in $\phi$ and $\theta$. As they cross the CTC, however, they are deflected in opposite directions in the transverse plane by the magnetic field. One way to look for conversions (including Dalitz decays) is therefore to look for oppositely charged tracks in the CTC which have a small $\Delta\theta$ separation, and when extrapolated back to the beam-pipe, have a very small opening angle.

A further property of these events is that the $e^+e^-$ pair is characterized by a very low invariant mass. Finally, $\pi^0$'s or photons which convert just before the CTC will not leave a track in the VTPC and we therefore require a minimum VTPC occupancy for the central electron candidate (see Section 5.7.2 for a discussion of VTPC occupancy).



At CDF, conversion-filter algorithms reject electrons if a track from an oppositely charged particle is found within 30° of the central electron candidate, and if they together form an invariant mass of $M_{ee} < 0.5$ GeV. A requirement that there be a VTPC occupancy of $> 20\%$ for the primary electron is also imposed The conversion removal process is described in detail in Reference[59]. There it is estimated that approximately 88% of conversion and 10% of prompt electrons are removed by the algorithm.

Heavy Quark Production

As in the previous analysis $b\bar{b}$ and $t\bar{t}$ production have to be considered as sources of events containing a single high-$E_T$ electron and multiple jets. In the case of $b\bar{b}$ production, the rate is somewhat higher in this channel since we no longer demand that both $b$'s undergo semi-leptonic decay. However it seems reasonable to expect that requiring both $\not\!\!E_T > 20$ GeV and an electron with $E_T > 20$ GeV and $ISO_4 < 0.1$ will eliminate this background, We therefore do not consider it further unless we have low-mass events which cannot be otherwise accounted for.

The same remarks about $t\bar{t}$ production as were made in Chapter 6 also apply here. An electron+multijets signal is expected from top-quark pairs, and indeed this channel was one of those explored by CDF [58, 59]. Though top has not yet been conclusively discovered, we need to keep it in mind in the event that we observe of a possible leptoquark signal.

## 7.6 Relative Likelihood Separation Of Signal And Background

In the previous section we concluded that hard cuts on combinations of kinematic variables cannot sufficiently separate the leptoquarks from the $W + 2$jet production. An alternative approach to differentiating signal and background processes is to define an N-variable relative likelihood $\mathcal{L}_N$, which in our case is defined in terms of N kinematic variables as

$$\mathcal{L}_N(M_{LQ}) = \frac{P_{LQ}(\text{var1})}{P_W(\text{var1})} \cdot \frac{P_{LQ}(\text{var2})}{P_W(\text{var2})} \cdots \frac{P_{LQ}(\text{varN})}{P_W(\text{varN})}. \qquad (7.7)$$

Here $P_{LQ}$ and $P_W$ are the leptoquark and $W+2$jet probability densities for each

variable, and are obtained from Monte Carlo distributions. An important point to notice is that since the kinematic distributions for leptoquark decay products change with $M_{LQ}$, the relative likelihood $\mathcal{L}_N$ also shares this dependency.

As a simple example, a 1-variable likelihood function which uses transverse mass as the differentiating variable would be

$$\mathcal{L}_1(M_{LQ}) = \frac{P_{LQ}(M_T)}{P_W(M_T)}.$$

Using the relative likelihood, we can say that a given event, based on the values of the N variables, is $\mathcal{L}_N$ times more likely to be associated with leptoquark-pair production than with W+2jet processes. When applied to a data sample containing many events, leptoquark production would be signalled by an excess of events at large values of $\mathcal{L}$. For convenience we will, from this point on, use $\log(\mathcal{L})$ rather than simply $\mathcal{L}$. After this transformation we see that leptoquark events will be associated with positive $\log(\mathcal{L})$, while for $W+2$jet events we expect to find negative values of $\log(\mathcal{L})$ in general.

In deciding which kinematic event variables to use in our relative likelihood, we recall the twelve variables shown in Figures 7.6- 7.11 for leptoquarks of mass $M_{LQ}$ = 45 and 75 GeV. These constitute a reasonably complete description of the properties of an event. Now from a set of 12 different variables we can make $2^{12} = 4096$ sub-sets of variables which are possible choices to use in $\log(\mathcal{L})$. This number can be reduced somewhat by not using the some of the variables which clearly have little separation power at any mass. We therefore select the nine variables that appear to show the best signal:background separation, thereby leaving us with the less daunting task of finding a variable set from only $2^9 = 512$ possible combinations. Having done this we form relative likelihood curves for signal and background for all 512 different variable-sets and for all four leptoquark masses. We find that a resonable separation of signal and background can be obtained in several different cases, each of which is comparable to the others.

For this analysis we choose one of these sets containing the following five variables:

1. Transverse energy of the electron: $E_T^e$



2. Transverse energy of the leading Jet $E_T^j$

3. The $e\nu$ transverse mass: $M_T^{e\nu}$

4. The dijet transverse mass: $M_T^{jj}$

5. $\not{E}_T$-significance $\Xi = \not{E}_T/\sqrt{E_T}$.

Our relative-likelihood variable is then given by

$$\log(\mathcal{L}_5) = \frac{P_{LQ}(E_T^e)}{P_W(E_T^e)} \cdot \frac{P_{LQ}(E_T^j)}{P_W(E_T^j)} \cdot \frac{P_{LQ}(M_T^{e\nu})}{P_W(M_T^{e\nu})} \cdot \frac{P_{LQ}(M_T^{jj})}{P_W(M_T^{jj})} \cdot \frac{P_{LQ}(\Xi)}{P_W(\Xi)} \qquad (7.8)$$

To find the relative likelihood for an event we first need to know the $P_{LQ}$ for each leptoquark mass considered, and the $P_W$. One possibility is to use normalized binned distributions such as those shown in Figures 7.6- 7.11. However, to reduce the effects of bin-size choice and large statistical fluctuations in bins with few events, we instead fit these histograms to an appropriate function, and then use re-normalized continuous distributions as our probability densities. Assuming the fit quality is good, this approach is reliable.

In Figures 7.12- 7.16 we present the fitted histograms for the five chosen variables. Distributions are shown for *all* leptoquark masses considered, and for the PAPAGENO W+2jet Monte Carlo events; as can be seen, the fit quality is good. With the fitted distributions we numerically integrate the associated functions and so obtain the corresponding normalization factors which we use in defining our probability densities $P_{LQ,W}$. This gives us everything we need to calculate the relative likelihood $\log(\mathcal{L}_5)$, and having explained the method we now turn to our analysis of the CDF data.

## 7.7 Analysis of the CDF Data

We start our analysis in the $e^{\pm}\nu_e$+dijet channel, as we did before, with the 4997 events in the CDF inclusive central electron data set. Recall that for the range of leptoquark masses considered (45-75 GeV) we expect, on average,

- $E_T^e > 20$ GeV,

- $E_T^{j1} > 20$ GeV and $E_T^{j2} > 20$ GeV,
- $E_T^e > 20$ GeV $\Longrightarrow \not\!\!E_T > 20$ GeV.

Our first requirement is that each event in the data set contains exactly one isolated central electron with $E_T > 20$ GeV. The single electron sample is found to contain 4574/4997 events, the other 423 being precisely those we started with in the $e^+e^-$+dijet analysis. Requiring the electron to be fiducial leaves 4157 events, an acceptance of 90.9%. This is somewhat above the 86.7% acceptance of the $\phi$-crack cut alone, but this is understandable since electrons lost directly down a crack are unlikely to be in the data set to begin with. In other words, electrons in the data set are already, in a sense, quasi-fiducial.

Turning the '$e$' data-set into an $e\nu$ sample, we now require $\not\!\!E_T > 20$ GeV. This leaves 2997 and 2718 events, before and after the fiducial cut on the electron. The cuts made so far are summarized as follows:

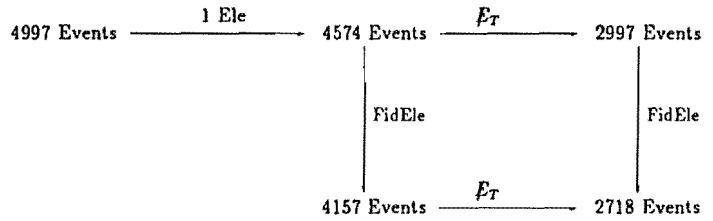


In Figure 7.17 we show the $E_T^e$, $\not\!\!E_T$, and $M_T^{e\nu}$ distributions for the 2718 events, as well as the data before the $\not\!\!E_T$ cut (dashed histograms). The transverse mass for the $e^\pm\nu_e$ data shows that our sample is clearly dominated by $W\pm$ production, much as the $e^+e^-$ data was by the $Z^0$-peak. We have so far made no restriction on any additional jets in the events, leaving open the possibility of a large signal at low $M_{LQ}$. However, we note that there are no unexpected bumps visible at low and intermediate values of $M_T$, this being where a large low-mass signal could be seen (see Figure 7.6). Such an approach was used by CDF in a search for the top-quark in the electron+jets channel where precisely these kind of deviations



in the $M_T^{e\nu} < 80$ GeV spectrum were looked for [58, 59].

In the absence of a large signal, we note that observation of a relatively small excess of events in the $M_T$ spectrum is likely to be difficult. However, we can perform an independent check by considering absolute event rates. Recall from Section 7.5.1 that we expect $\sigma(W \to e\nu)/\sigma(Z \to ee) \simeq 10.2$. By comparing the number of observed $e^+e^-$ and $e^\pm\nu_e$ events, and assuming that any new process doesn't contribute equally to both samples, we can therefore check our pre- jet-cut data set for any excess. After imposing equivalent cuts on both $e\nu$ and $e^+e^-$ samples, we find

$$R_{W/Z} = \frac{N(e^\pm\nu_e)}{N(e^+e^-)} = \frac{2718}{289} = 9.4 \pm 0.5 \qquad (7.9)$$

The quoted error is statistical. The 289/423 $e^+e^-$ events are obtained by requiring at least one central fiducial electron with $E_T > 20$ GeV. The $E_T$ of the other electron must also be $> 20$ GeV to match the $\not\!\!E_T$ cut in the $e^\pm\nu_e$ sample. Finally, since we are concerned with the $Z^0$ cross-section and not the Drell-Yan continuum, we also require $75 < M^{ee} < 105$ GeV. We note that the ratio $R_{W/Z}$ is artificially low since we have not yet accounted for Drell-Yan events under the $Z^0$-peak, making $N(e^+e^-)$ a little high. We estimate that around 4 events out of 289 are due to Drell-Yan production, using $\int \sigma_{DY} / \int \sigma_{Z,DY} = 1.3\%$ given in Reference [65]. After correcting for this, we find the observed $W/Z$ ratio increases slightly to $9.5 \pm 0.5$. This is in reasonable agreement with the predicted value of 10.2, albeit a little low. However, the point is that there is no apparent excess of $e^\pm\nu_e$ events.

To enhance the leptoquark signal and reduce the $W$ + 2jet background we now introduce cuts on the number and energy of additional jets in an event. As before, we start with a cut of $E_T^j > 10$ GeV and find 1118 events with at least one such jet. Since we expect a dijet signal, we tighten our jet requirement to two jets, both with $E_T^{j1,j2} > 10$ GeV. Applying this cut leaves 378 events. The $E_T$ spectra for the leading jet in the $e^\pm\nu_e+ \geq 1$jet sample, and the second jet in the $\geq$ 2jet sample, are shown in Figure 7.18. The $E_T$ spectra are observed to be steeply falling, as we would expect from initial state radiation, and as was also

found in the $e^+e^-$+dijet analysis (we note a two-bin excess of events observed at around $E_T^{j1} = 60$ GeV in the leading jet spectrum).

From the 378 remaining events we now remove $e^+e^-$+1jet events in which one electron fails quality cuts and is subsequently identified as a jet. This removal is done by imposing a cut on jet electromagnetic-fraction EMF< 95% and reduces the sample to 352 events. Finally we remove any event in which the electron is found to be consistent with a $\gamma$-conversion.

This leaves us with 295 events. As before we summarize the number of events surviving after each successive cut as follows:

$$2718 \xrightarrow{j10} 1118 \xrightarrow{j10+j10} 378 \xrightarrow{\text{EMF}} 352 \xrightarrow{\gamma} 295$$

The electron-jet mass spectrum for these events is shown in Figure 7.19, made using the method presented in Section 7.3.2. The distribution is not exactly smooth, and several peaks can be seen, notably at M(Ele-Jet)≃40, 55, 70, and 110 GeV. If any of these were due to leptoquark production, the peak would survive raising the $E_T$ cut on both jets, as we now do.

With a cut of $E_T^j > 15$ GeV, the number of one(two) jet events in our sample is 643(160) before any EMF cut or $\gamma-$ conversion removal. Focusing on two-jet events, we find 145 events which survive the EMF,and 115 which are not removed by the $\gamma$-conversion filter. The high-$E_T^j$ threshold cuts are summarized as follows:

$$2718 \xrightarrow{j15} 643 \xrightarrow{j15+j15} 160 \xrightarrow{\text{EMF}} 145 \xrightarrow{\gamma} 115$$

We do not raise the jet-$E_T$ cut any higher, and these 115 events constitute our final data sample.

The electron-jet mass spectrum for these events is shown in Figure 7.20 and as can be seen the peak at 55 GeV remains. To assess its significance we show



in Figure 7.8.2 the same distribution along with the electron-jet mass spectrum for our VECBOS $W$ + 2jet sample. For the purposes of shape comparison we have normalized the Monte Carlo events to the data. The $W$ + 2jet spectrum is also observed to peak at 55 GeV. This is not surprising given that the electron from $W$-decay has, on average, $E = 40$ GeV, and we are using 15-GeV jets. The significance of the deviation is now lessened, even more so when we note that the next higher bin is statistically low. For 55-GeV leptoquark production we would expect any excess to be spread over several such bins (Figure 7.5). We therefore do not consider this as evidence for the production of 55-GeV leptoquark pairs.

### 7.7.1 Relative likelihood Analysis of the CDF Data

At first sight, an observation of 115 events appears to be in remarkable agreement with the 114.2 events predicted by the default Monte Carlo data set. However, because of the large uncertainty in the absolute $W$ + 2jet cross section (see Table 7.4) we are not justified in performing a background subtraction and setting leptoquark limits based on zero events observed. In fact 114.2 events turns out to be the largest prediction for the $W$ + 2jet background using a range of different structure functions and choices for the QCD scale; an excess of ten events may not be at all unlikely. Since, as we have already explained, we cannot kinematically distinguish the signal from background based on one or even two event variables, we now turn to the relative likelihood method presented in Section 7.6.

Our relative likelihood function, defined in Equation 7.8 as

$$\mathcal{L} = \prod_{i=1}^{5} P_i(LQ)/P_i(W + 2\text{jet})$$

is based on normalized fitted probability distributions for five chosen kinematic variables. Instead of $\mathcal{L}_5$, we will use $\log(\mathcal{L}_5)$ which, from this point on, will usually be denoted simply as 'logl'. For a sample of pure leptoquark events the mean of this variable should be at logl≥ 0. Conversely, for a sample of pure $W$ + 2jet events we expect, on average, logl≤ 0. One important point to note here is that $\mathcal{L}$ is defined in terms of $M_{LQ}$-dependent probability distributions. This implies

that the logl-distribution for CDF data will also vary, depending on the particular value of leptoquark mass we are considering.

In Figures 7.22- 7.25 we now show the $\log(\mathcal{L}_s)$ distributions for the CDF data using the probability densities in Figures 7.12- 7.16 for 45, 55, 65, and 75 GeV leptoquark pairs. On each figure we also show the distributions for pure Monte Carlo leptoquark and $W+2$jet events samples. For the purposes of shape comparison, we have normalized the number of MC leptoquark events using $\sigma$(ISAJET) and $x = 50\%$, while the $W+2$jet distributions have been normalized to the data (115 events).

Our first qualitative observation is that the distribution for the CDF data agrees well with the $W+2$jet Monte Carlo for all leptoquark masses considered. Furthermore no significant excess of events is seen with logl> 0 for any value of $M_{LQ}$.

Our quantitative analysis is concerned with attempting to identify how many events may be consistent with leptoquark production. We begin by defining signal and background regions

$$\text{Signal: } \log \mathcal{L}_s > 2.0$$

$$\text{Background: } \log \mathcal{L}_s < -2.0$$

in which we expect high relative fractions of leptoquark and $W+2$jet events respectively. Using Monte Carlo cross sections we obtain the number of signal and background events in each region, as well as the actual number of events observed. These are shown in Tables 7.5 and 7.6.

| Signal: $\log \mathcal{L}_s > 2.0$ | | | |
|---|---|---|---|
| $M_{LQ}$ (GeV) | N(LQ) | N(W+2jet) | N(Data) |
| 45 | 28.3 | 7.2 | 7 |
| 55 | 16.0 | 5.7 | 1 |
| 65 | 10.1 | 6.7 | 3 |
| 75 | 7.5 | 8.9 | 9 |

Table 7.5: Expected population of the relative-likelihood signal region by leptoquark and W+2jet events, and the actual number of events observed. Leptoquark values assume $x = 50\%$.



| Background: $\log \mathcal{L}_s < -2.0$ | | | |
|---|---|---|---|
| $M_{LQ}$ (GeV) | N(LQ) | N(W+2jet) | N(Data) |
| 45 | 3.9 | 25.7 | 25 |
| 55 | 1.7 | 14.5 | 13 |
| 65 | 1.8 | 23.1 | 27 |
| 75 | 1.3 | 36.6 | 40 |

Table 7.6: Expected population of the relative-likelihood background region by leptoquark and W+2jet events, and the actual number of events observed. Leptoquark values assume $x = 50\%$.

At first sight there appears to be good agreement in the background region ($\log \mathcal{L}_s < -2.0$) between the number of events predicted by the $W+2$jet Monte Carlo and the number actually observed. By normalizing the Monte Carlo cross section to the CDF data in the region logl$\leq -2.0$ (where little leptoquark signal is expected), we can make an absolute prediction of the number of $W+2$jet events in the signal region. More correctly, in the background region we normalize the W cross section

$$N_W \longrightarrow N'_W = N_{obs} - N_{LQ}$$

since the background region may contain a small number of leptoquark events.

The number of $W+2$jet events predicted with $\log \mathcal{L}_s < -2.0$ after this normalization, and the associated scale factor $SF = N'_W/N_W$, are shown in Table 7.7.

| Background: $\log \mathcal{L}_s < -2.0$ | | | | | |
|---|---|---|---|---|---|
| $M_{LQ}$ (GeV) | $N_{LQ}$ | $N_W$ | $N'_W$ | $N_{obs}$ | $SF$ |
| 45 | 3.9 | 25.7 | 21.1 | 25 | 0.821 |
| 55 | 1.7 | 14.5 | 11.3 | 13 | 0.779 |
| 65 | 1.8 | 23.1 | 25.2 | 27 | 1.091 |
| 75 | 1.3 | 36.6 | 38.7 | 40 | 1.057 |

Table 7.7: Scale factor ($SF$) normalization of the number of expected W+2jet events in the background region.

We are now able to rescale $N_W \longrightarrow N'_W$ in the signal region $\log \mathcal{L}_s > 2.0$, and the results are shown in Table 7.8.

| Signal: $\log \mathcal{L}_s > 2.0$ | | | | |
|---|---|---|---|---|
| $M_{LQ}$ (GeV) | $N_{LQ}$ | $N_W$ | $N'_W$ | $N_{obs}$ |
| 45 | 28.3 | 7.2 | 5.9 | 7 |
| 55 | 16.0 | 5.7 | 4.5 | 1 |
| 65 | 10.1 | 6.7 | 7.3 | 3 |
| 75 | 7.5 | 8.9 | 9.4 | 9 |

Table 7.8: Comparing the number of observed events in the leptoquark signal region with the predicted number of leptoquark and $W$ + 2jet events.

## 7.8 Leptoquarks Limits From The $e^{\pm}\nu_e$+Dijet Channel

### 7.8.1 Limits In The Absence Of Systematic Uncertainties

Table 7.8 shows that there is reasonable agreement between the number of predicted $W$ + 2jet events and the number observed, at least for $M_{LQ} = 45$ and 75 GeV. At 55 and 65 GeV the data appears to be systematically lower than we would expect. However, there is clearly no excess of events in regions of high leptoquark likelihood and this allows us to set stringent limits on the branching fraction $x = BR(LQ \rightarrow e + u)$. For example at $M_{LQ} = 45$ GeV we observe 7 events with a predicted signal and background of 28.3 and 5.9 events respectively.

In the Appendix we show how to calculate limits on a signal at the 95% CL in the presence of a background, and with a given number of observed events. Denoting by $\mu_S$ the Poisson mean for the signal, and by $\mu_B$ the mean for the background, the 95% CL on the upper number of signal events in our data consistent with an observation of $N_0$ is obtained from

$$1 - \frac{e^{-(\mu_B+\mu_S)} \sum_{n=0}^{N_0} \frac{(\mu_B+\mu_S)^n}{n!}}{e^{-(\mu_B)} \sum_{n=0}^{N_0} \frac{\mu_B^n}{n!}} = 0.95 \qquad (7.10)$$

Using $\mu_B = N'_W$ and $N_0 = N_{obs}$, we find the following upper limits on $\mu_S$ at 95% CL:



| Signal: $\log \mathcal{L}_s > 2.0$ | | |
|---|---|---|
| $M_{LQ}$ (GeV) | $N_{LQ}(x = 50\%)$ | $N_{LQ}$(95%CL) |
| 45 | 28.3 | 7.8 |
| 55 | 16.0 | 5.7 |
| 65 | 10.1 | 6.9 |
| 75 | 7.5 | 7.6 |

Table 7.9: Expected number of $e^{\pm}\nu_e$+dijet events for $x = 50\%$ and $\log \mathcal{L}_s > 2.0$, and the 95% CL on the upper number of such events in the CDF Data. No systematic or statistical errors are included.

Finally, we can use $N_{LQ}(x = 50\%)$ and $N_{LQ}$(95%CL) to set limits on the branching fraction $x$. The value of $x$ at 95% CL is obtained from

$$N_{95} = \sigma \cdot 2x(1-x) \cdot \epsilon_Z \cdot \epsilon_e \cdot \epsilon_t \cdot A. \qquad (7.11)$$

Here $\epsilon_Z, \epsilon_e$, and $\epsilon_t$ are the acceptances for the z-vertex cut (95.44%), electron quality cuts (87.3%), and level-2 trigger efficiency (97.3%). $A$ is the acceptance for all other cuts made.

For $x = 0.5$ we expect

$$N_{LQ} = \sigma \cdot 2(0.5)(1-0.5) \cdot \epsilon_Z \cdot \epsilon_e \cdot \epsilon_t \cdot A. \qquad (7.12)$$

Defining $\alpha = N_{95}/N_{LQ}$ we obtain

$$x_{95} = \frac{1 \pm \sqrt{1-\alpha}}{2}. \qquad (7.13)$$

The range of $x$-values excluded at the 95% CL in the absence of systematic errors is shown in Table 7.10.

| LQ Mass (GeV) | Excluded x at 95% CL |
|---|---|
| 45 | $7.4\% < x < 92.6\%$ |
| 55 | $9.8\% < x < 90.2\%$ |
| 65 | $21.9\% < x < 78.1\%$ |
| 75 | Cannot exclude any x at 95% CL |

Table 7.10: Excluded values of the charged branching fraction x at 95% CL in the absence of systematic errors.

### 7.8.2 Limits Including Systematic Uncertainties

There are two classes of systematic error that we have considered in this analysis:

- those which lead to uncertainties in the number of events in the final sample, but which do not affect distribution shapes, and
- those which lead to different distribution shapes and hence to different relative likelihood curves

The first type of error is included in our final results for this analysis by convoluting a Poisson distribution with a Gaussian of appropriate mean, much as we did in the $e^+e^-$+dijet channel.

For the second kind of error, there is no such associated Gaussian uncertainty. Factors leading to changes in the likelihood distributions include, for example, the choice of structure function, $Q^2$-scale, or Monte Carlo generator. We do not convolute such errors into our final limits, quoting only what structure function etc. was used. We do, however, consider the sensitivity of our results to such choices.

Uncertainties in the Expected Number of Events

Uncertainties in the expected number of events (normalization errors) can be incorporated into our limits as Gaussian errors on the mean $\mu_s$ of a Poisson distribution. In the previous section we evaluated 95% confidence levels in a Poisson process containing both signal and background contributions, but in the absence of any uncertainties. In Section A.2.2 of the appendix, we show how this is generalized to account for the presence of Gaussian systematic errors $\sigma_{s,b}$ on the signal and background. In this thesis we normalize the background to the CDF data, eliminating the need to estimate $\sigma_b$.

To estimate the size of $\sigma_s$ we consider the following sources of error on the number of events in our final Monte Carlo data sets.

- Jet Energy Scale and Jet Energy Correction Scheme
- Electron Selection Cut Efficiency



- Integrated Luminosity $\mathcal{L}$
- Finite Statistics

The methods of estimating normalization errors from jet energy-scale and energy-correction scheme uncertainties were described in the previous analysis. The estimated errors $\Delta A_J$ for the signal and background processes in the $e^{\pm}\nu_e$+dijet channel are given in Table 7.11.

The uncertainties on the electron selection cut efficiency and integrated luminosity are $\pm 2.6\%$ and $\pm 7\%$ respectively, shown in Table 7.11 as $\Delta A_e$ and $\Delta A_{\mathcal{L}}$ respectively. Binomial statistical errors on the fraction of Monte Carlo events passing our cuts are given as $\Delta A_S$, and range from $1.6 - 3.3\%$.

Finally we add all errors in quadrature to give the total systematic uncertainty $\Delta A_T$.

| $M_{LQ}$ | 45 GeV | 55 GeV | 65 GeV | 75 GeV |
|---|---|---|---|---|
| $\Delta A_J$ | 26.1 | 20.4 | 15.5 | 11.6 |
| $\Delta A_S$ | 3.3 | 2.4 | 1.8 | 1.6 |
| $\Delta A_{\mathcal{L}}$ | 7.0 | 7.0 | 7.0 | 7.0 |
| $\Delta A_e$ | 2.3 | 2.3 | 2.3 | 2.3 |
| $\Delta A_T$ | 27.3 | 21.9 | 15.3 | 13.9 |

Table 7.11: Sources of systematic error on the signal event acceptances, and the combined uncertainty $\Delta A_T$. All values for $\Delta A$ are given in %.

We now use $\Delta A_T$ to re-derive the upper number of leptoquark events in our data set at the 95% CL. The values of $N_{95}$ are given in Table 7.12 (compare with $N_{95}$ from Table 7.9 in the absence of uncertainties).

From $N_{95}$ we then derive the corresponding range of excluded charged branching fraction $x_{95}$ using Equation 7.13. Again, these are shown in Table 7.12.

| Signal: $\log \mathcal{L}_5 > 2.0$ | | | |
|---|---|---|---|
| LQ Mass (GeV) | NLQ (Expected) | NLQ (95% CL) | Excluded x at 95% CL |
| 45 | 28.3 | 9.2 | $8.9\% < x < 91.1\%$ |
| 55 | 16.0 | 6.2 | $10.9\% < x < 89.1\%$ |
| 65 | 10.1 | 7.2 | $23.2\% < x < 76.8\%$ |
| 75 | 7.5 | 7.8 | Cannot Exclude Any x |

Table 7.12: Limits on the charged branching fraction $x = BR(LQ \rightarrow e + u)$ at 95% CL after inclusion of systematic errors. Results use NLQ, derived using LO cross section and $x = 1/2$.

| Signal: $\log \mathcal{L}_5 > 2.0$ | | | |
|---|---|---|---|
| LQ Mass (GeV) | $K$·NLQ (Expected) | NLQ (95% CL) | Excluded x at 95% CL |
| 45 | 35.7 | 9.2 | $6.9\% < x < 93.1\%$ |
| 55 | 20.5 | 6.2 | $8.2\% < x < 91.8\%$ |
| 65 | 12.7 | 7.2 | $17.1\% < x < 82.9\%$ |
| 75 | 9.3 | 7.8 | $29.9\% < x < 70.1\%$ |

Table 7.13: Limits on the charged branching fraction $x = BR(LQ \rightarrow e + u)$ at 95% CL after inclusion of systematic errors. Results use NLQ, derived using $K$·LO cross section and $x = 1/2$.

Figure 7.26 presents our limits on $x$ versus $M_{LQ}$ for this channel, along with those from the previous channel for comparison.

Uncertainties in variable distributions from Monte Carlo

By using different structure functions and by varying our choice of $Q^2$ scale we alter the shapes of the distributions of the variables used in our separation of signal and background. Since this leads to a corresponding change in the relative likelihood distribution, not only does this affect the number of signal and background events passing the $\log \mathcal{L}$ cuts, it also alters the number of observed events in the signal and control regions. The usual prescription of calculating confidence levels on a signal in the presence of a background is no longer applicable.

Instead we quote our limits using a given structure function (HMRSB-190) and a given $Q^2$ scale ($Q =< P_T >$). To show how sensitive we are to structure function and $Q^2$-scale choice we derive limits on $x$ versus $M_{LQ}$ for the following structure functions:



- HMRSB-190 with $Q =< P_T >$
- DO-LO (1991) with $Q =< P_T >$
- EHLQ-II with $Q =< P_T >$

and for the following choice of $Q$ scale

- HMRSB-190 with $Q =< P_T >$
- HMRSB-190 with $Q$ =Total M
- HMRSB-190 with $Q = M_W$

The results are shown in Figures 7.27 and 7.28 respectively (note: these two plots do not have acceptance systematic errors included).

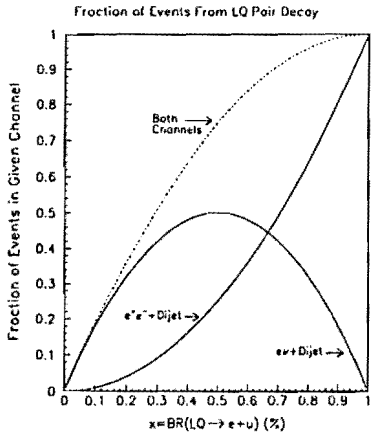


Figure 7.1: Fraction of leptoquark-pair events which are expected to have a particular decay signature as a function of $x = BR(LQ \rightarrow e + u)$.

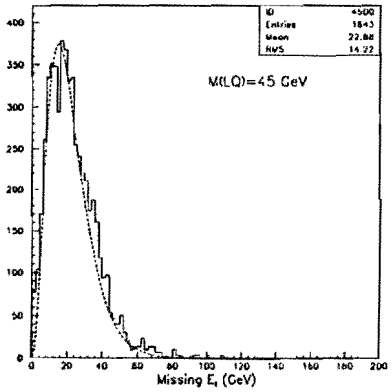


Figure 7.2: The missing-$E_T$ spectrum (solid histogram) for $e^{\pm}\nu_e$+dijet events from 45-GeV leptoquark pairs after CDF detector simulation and event reconstruction. Also shown is the corresponding parton-level neutrino spectrum $E_T^{\nu}$ (dot-dash curve).



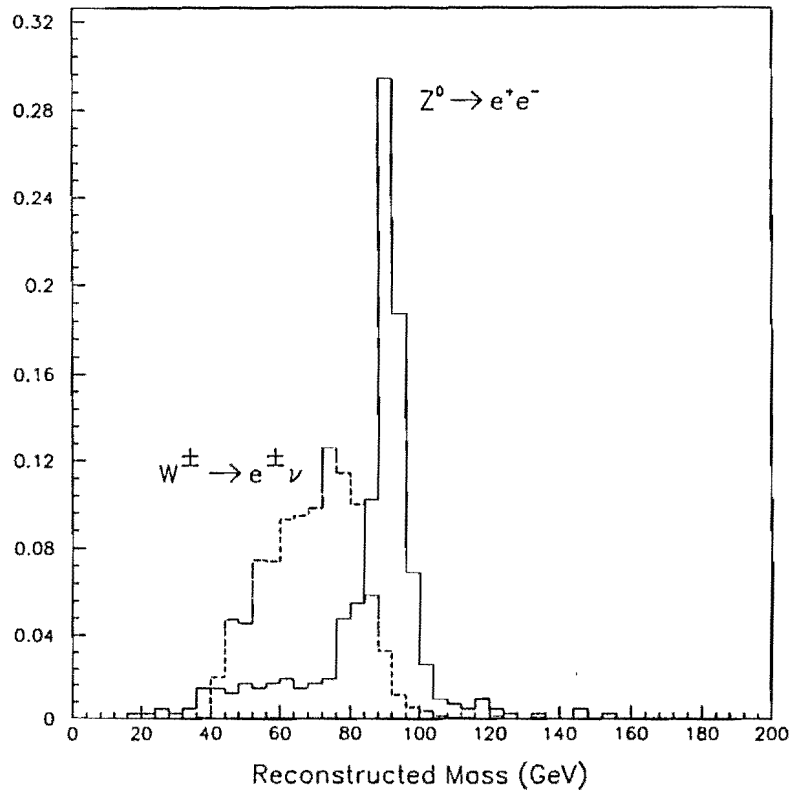


Figure 7.3: Comparison of the $Z^0$ mass and $W^{\pm}$ transverse-mass resolution from $Z^0 \rightarrow e^+e^-$ and $W \rightarrow e^{\pm}\nu_e$ events at CDF. Histograms have been given equal normalizations.

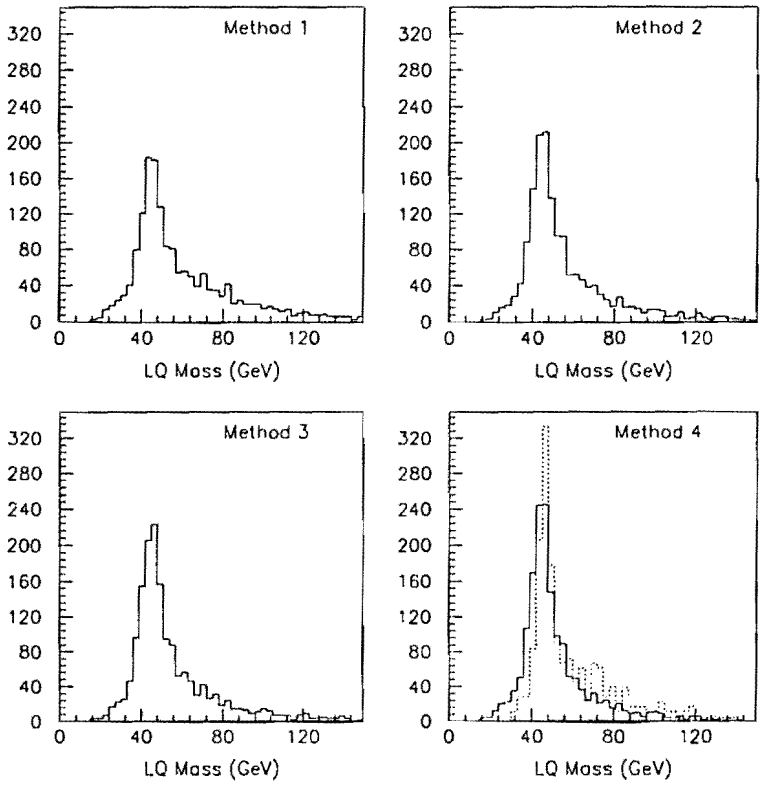


Figure 7.4: Leptoquark mass reconstruction in the $e^{\pm}\nu_e$+dijet channel. Last figure shows corresponding distribution for the $e^+e^-$+dijet channel. Generated $M_{LQ} = 45$ GeV.



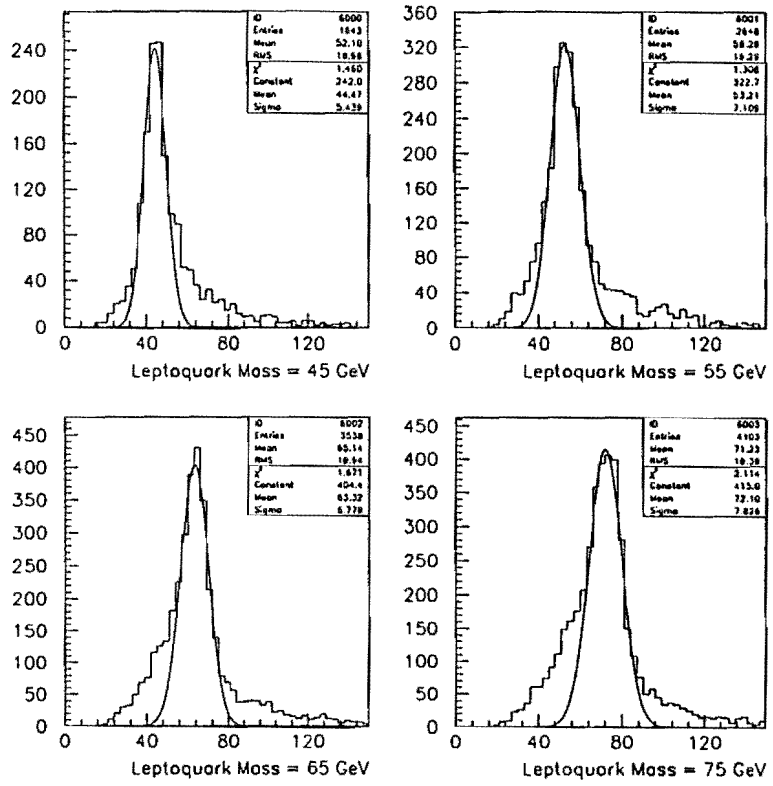


Figure 7.5: Resolution of the reconstructed leptoquark mass for each of the four different leptoquark masses studied in the $e^{\pm}\nu_e$+dijet channel. Also shown are Gaussian fits to the mass peak.

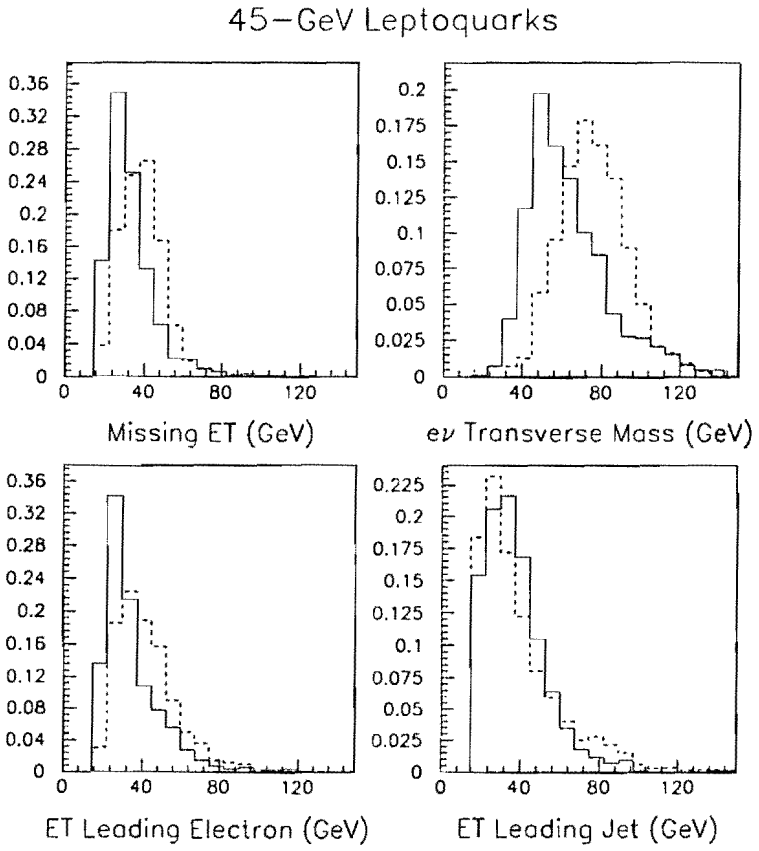


Figure 7.6: Distributions for 45-GeV ISAJET leptoquark-pairs (solid) and VECBOS W+2jet events (dashed) (1/3). Equal normalizations are used.



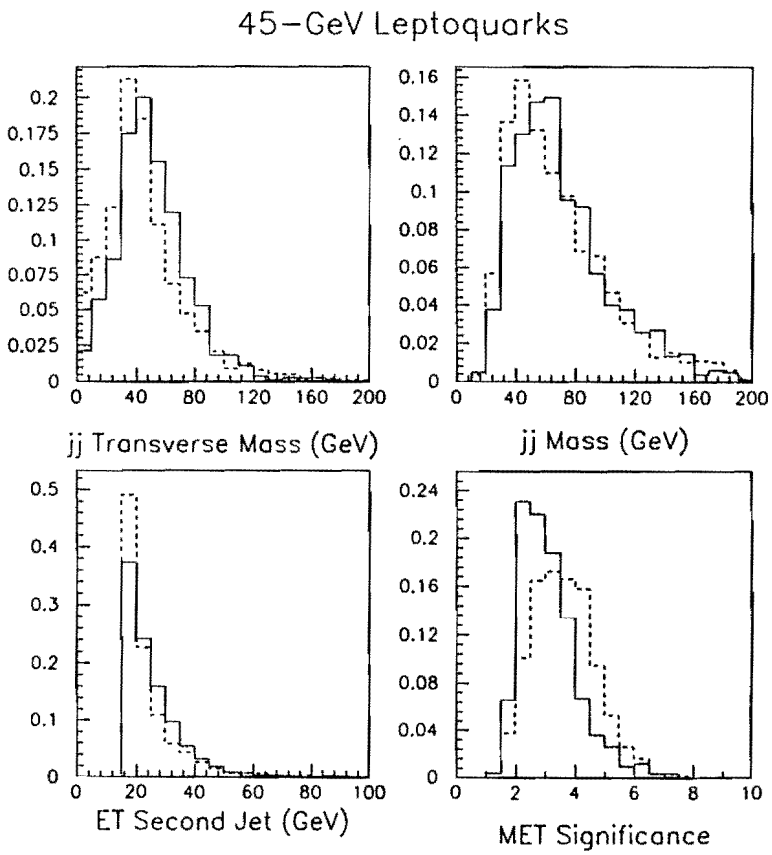


Figure 7.7: Distributions for 45-GeV ISAJET leptoquark-pairs (solid) and VECBOS W+2jet events (dashed) (2/3). Equal normalizations are used.

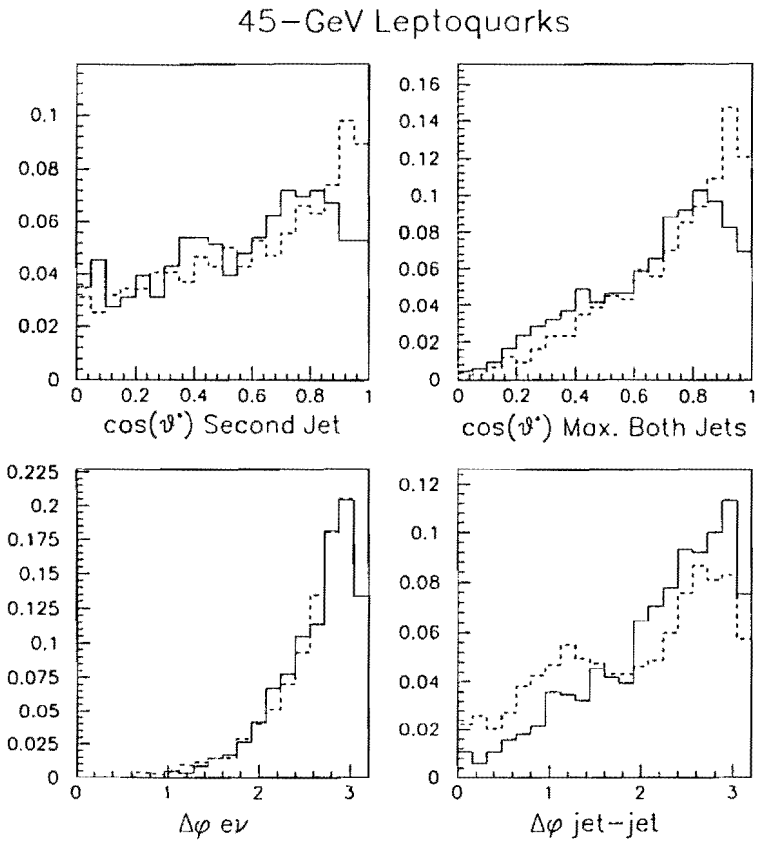


Figure 7.8: Distributions for 45-GeV ISAJET leptoquark-pairs (solid) and VECBOS W+2jet events (dashed) (3/3). Equal normalizations are used.



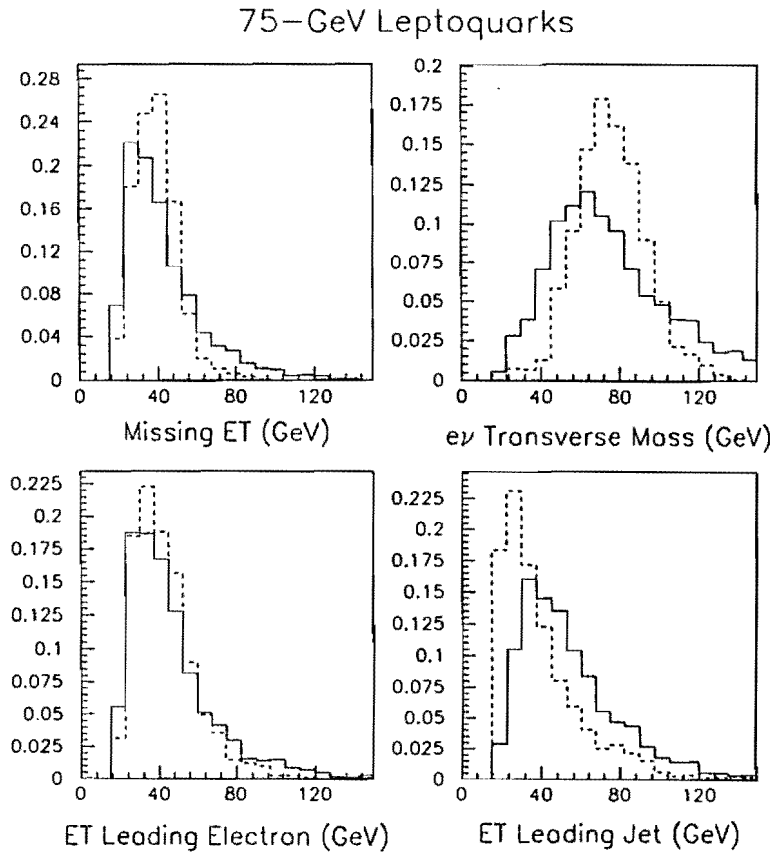


Figure 7.9: Distributions for 75-GeV ISAJET leptoquark-pairs (solid) and VECBOS W+2jet events (dashed) (1/3).Equal normalizations are used.

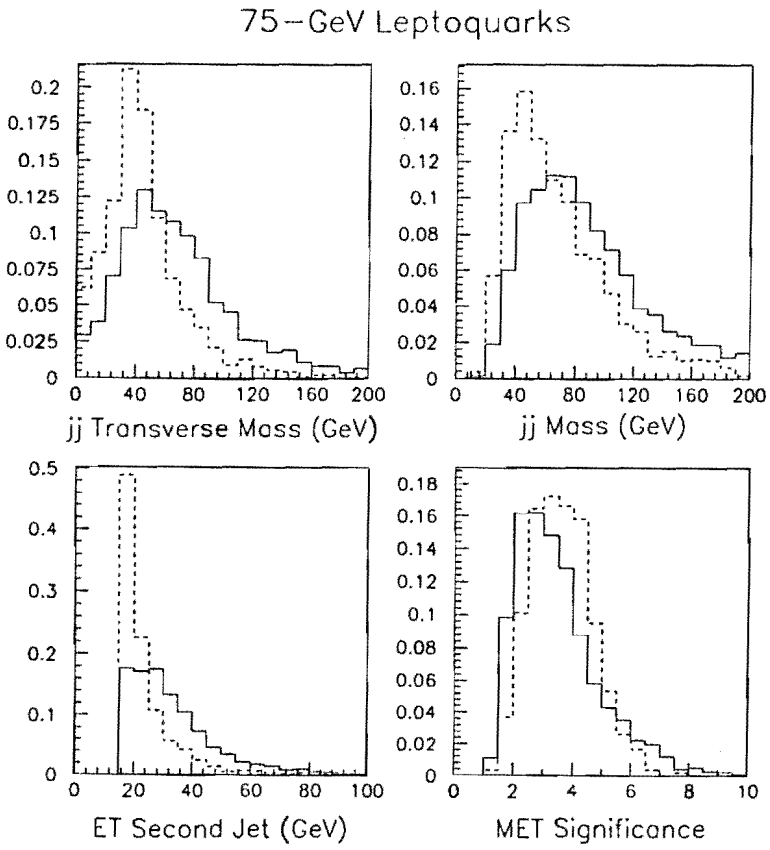


Figure 7.10: Distributions for 75-GeV ISAJET leptoquark-pairs (solid) and VECBOS W+2jet events (dashed) (2/3). Equal normalizations are used.



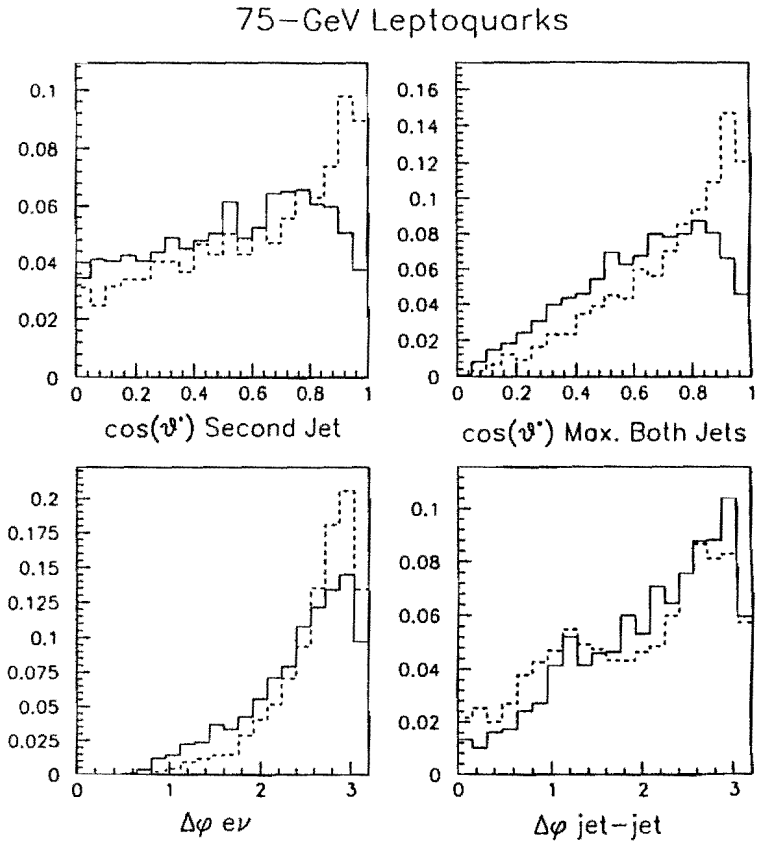


Figure 7.11: Distributions for 75-GeV ISAJET leptoquark-pairs (solid) and VECBOS W+2jet events (dashed) (3/3). Equal normalizations are used.

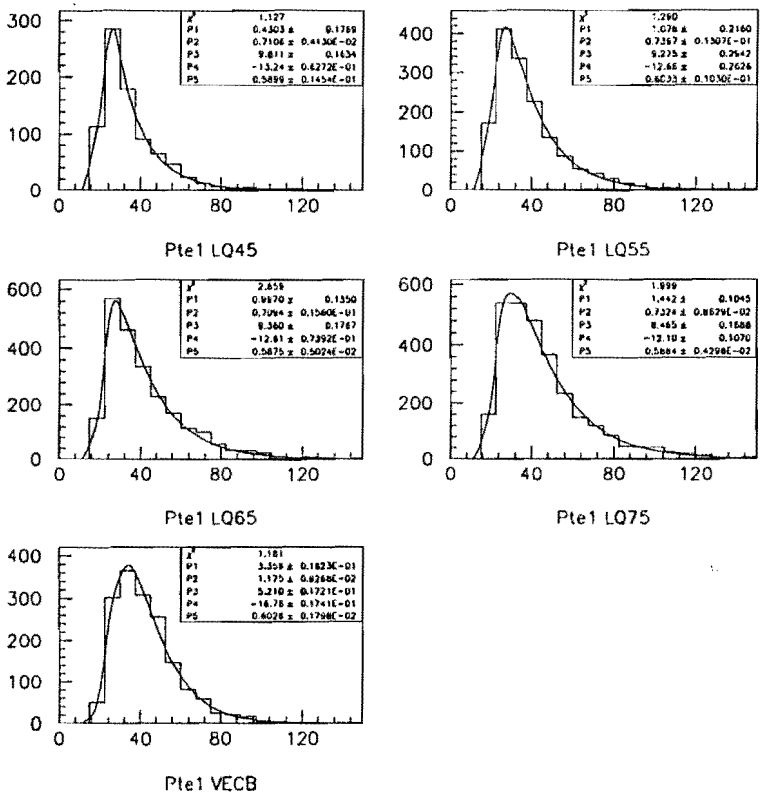


Fit Function: $y = (P2 \cdot x + P4)^{P1} \exp\left(P3 - P2 \cdot x^{P5}\right)$

Figure 7.12: $E_T$ of the electron in $e^{\pm}\nu_e$+dijet events. Fitted distributions are given for leptoquark signal and $W$ + 2jet background.



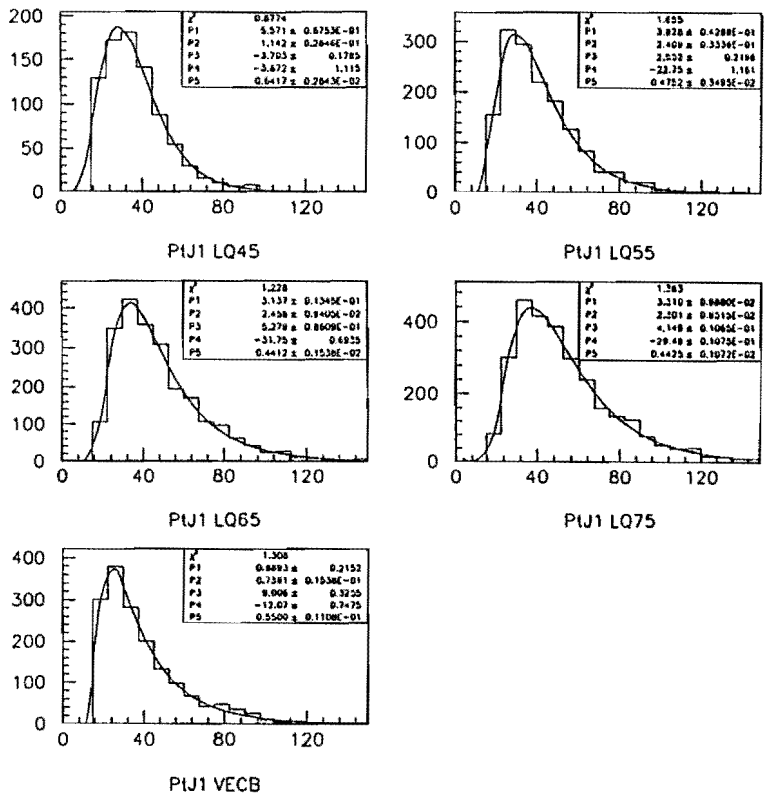


Fit Function: $y = (P2 \cdot x + P4)^{P1} \exp\left(P3 - P2 \cdot x^{P5}\right)$

Figure 7.13: $E_T$ of the leading jet in $e^{\pm}\nu_e$+dijet events. Fitted distributions are given for leptoquark signal and $W$ + 2jet background.

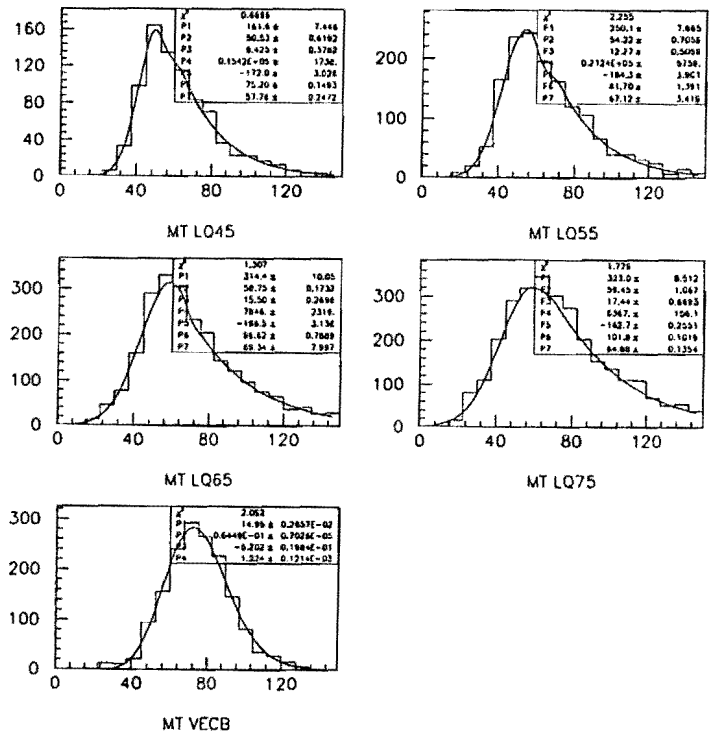


LQ Fit Function: $y = P1 \cdot \exp[-\frac{1}{2}\left(\frac{x-P2}{P3}\right)^2]$ for $x < P7$

LQ Fit Function: $y = P4 \cdot \exp[-\frac{1}{2}\left(\frac{x-P5}{P6}\right)^2]$ for $x > P7$

W Fit Function: $y = (P2 \cdot x)^{P1} \exp\left(P3 - P2 \cdot x^{P4}\right)$

Figure 7.14: $M_T^{e\nu}$ in $e^{\pm}\nu_e$+dijet events. Fitted distributions are given for leptoquark signal and $W$ + 2jet background.



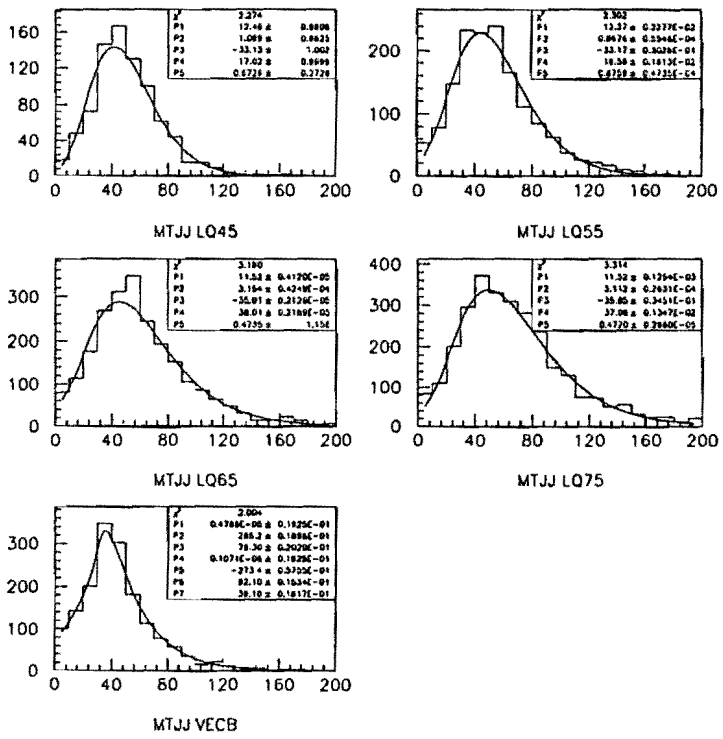


LQ Fit Function: $y = (P2 \cdot x + P4)^{P1} \exp\left(P3 - P2 \cdot x^{P5}\right)$

W Fit Function: $y = P1 \cdot \exp[-\frac{1}{2}\left(\frac{x-P2}{P3}\right)^2]$ for $x < P7$

W Fit Function: $y = P4 \cdot \exp[-\frac{1}{2}\left(\frac{x-P5}{P6}\right)^2]$ for $x > P7$

Figure 7.15: $M_T^{jj}$ in $e^{\pm}\nu_e$+dijet events. Fitted distributions are given for leptoquark signal and $W$ + 2jet background.

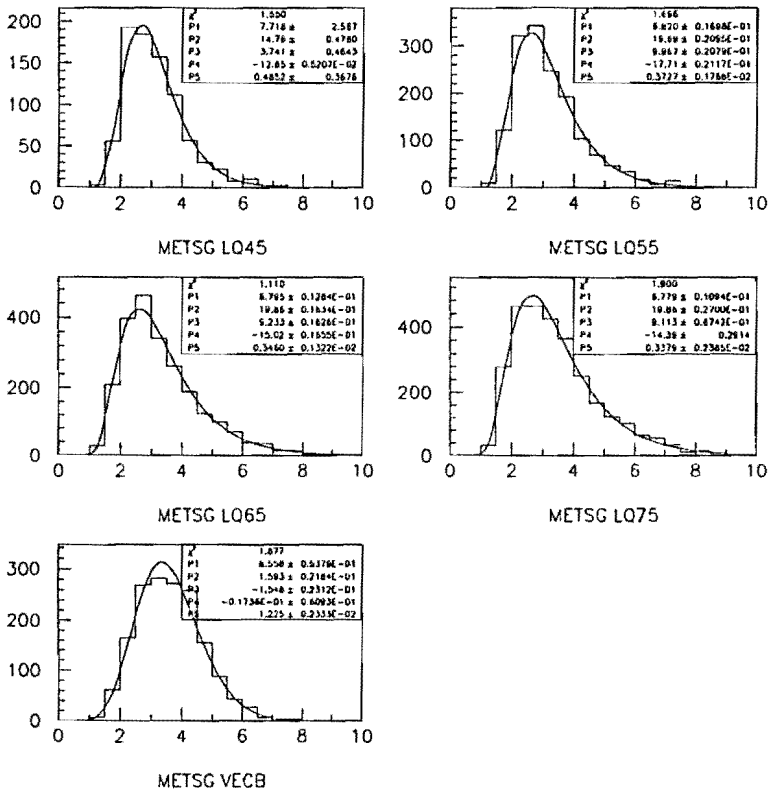


Fit Function: $y = (P2 \cdot x + P4)^{P1} \exp\left(P3 - P2 \cdot x^{P5}\right)$

Figure 7.16: Missing-$E_T$ Significance in $e^{\pm}\nu_e$+dijet events. Fitted distributions are given for leptoquark signal and $W$ + 2jet background.



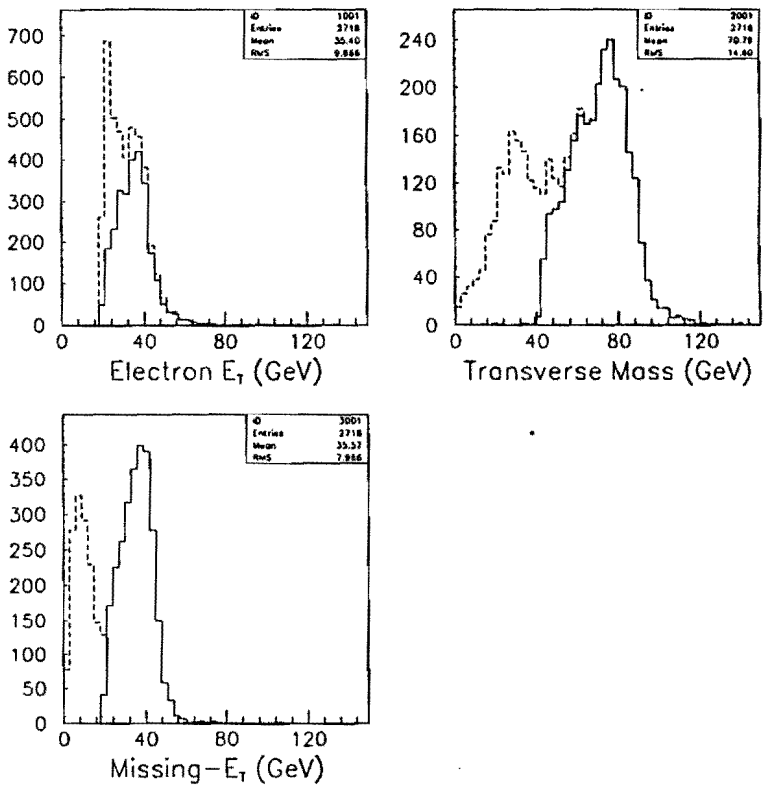


Figure 7.17: The electron-$E_T$, missing-$E_T$, and transverse mass $M_T$ distributions for the CDF single electron data set before (dotted) and after (solid) a cut of missing-$E_T > 20$ GeV.

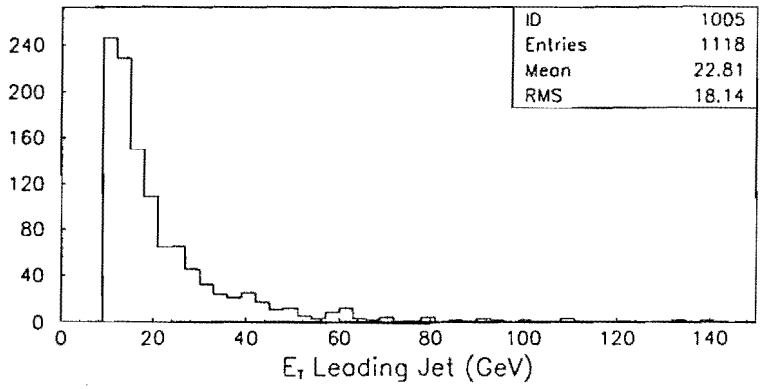


Figure 7.18: The $E_T$ spectra for any additional jets in the 2718 $e^{\pm}\nu_e$ events shown in the previous figure. There are 1118 events with at least one jet passing $E_T > 10$ GeV, and 378 events with two such jets.



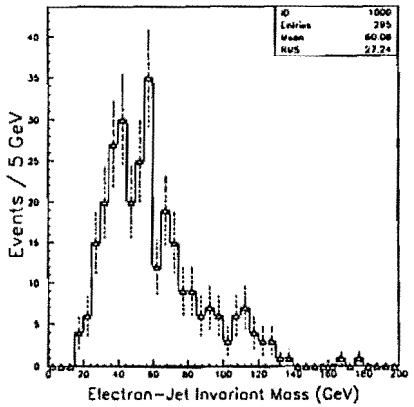


Figure 7.19: Electron-Jet Mass Spectrum in for CDF single-electron+dijet events. Jet-$E_T > 10$ GeV.

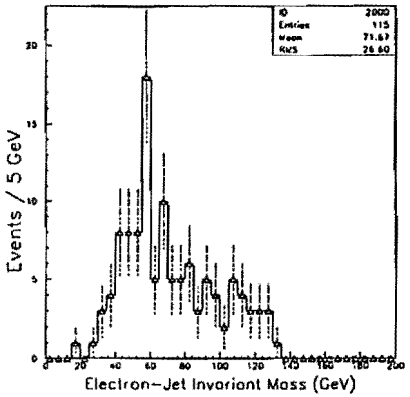


Figure 7.20: Electron-Jet Mass Spectrum in for CDF single-electron+dijet events. Jet-$E_T > 15$ GeV.

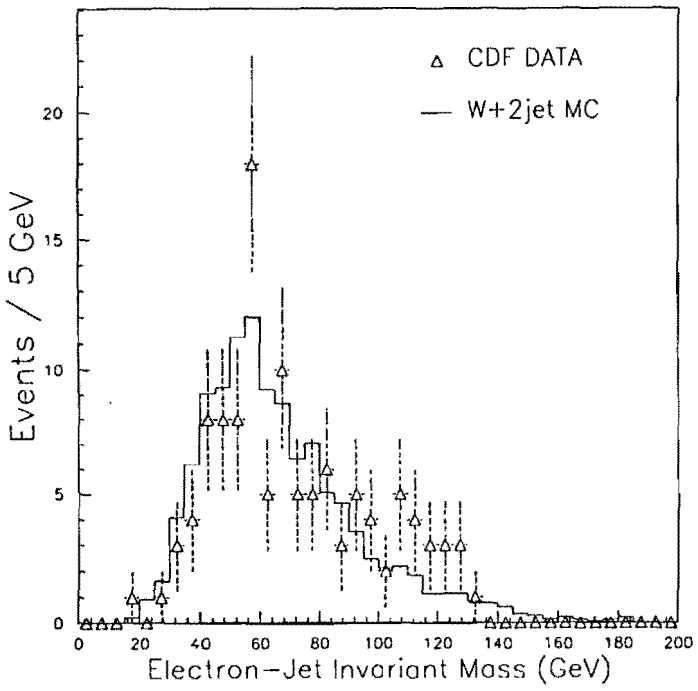


Figure 7.21: Comparing electron-jet invariant mass spectra for the CDF Data and VECBOS $W$ + 2jet events.



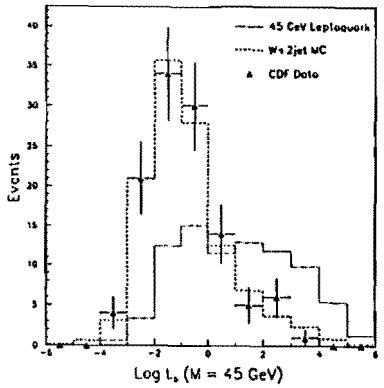


Figure 7.22: Log Relative-likelihood $\mathcal{L}_s = P(LQ45)/P(W + 2)$jet for CDF $e^{\pm}\nu_e$+dijet data. Also shown are the distributions for pure samples of Monte Carlo LQ45 and $W$ + 2jet samples.

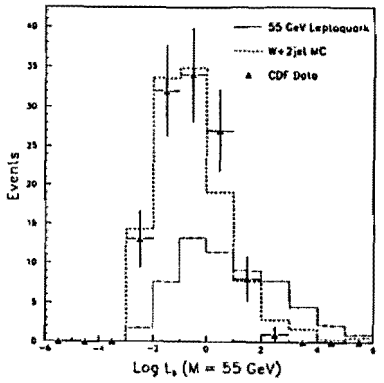


Figure 7.23: Log Relative-likelihood $\mathcal{L}_s = P(LQ55)/P(W + 2)$jet for CDF $e^{\pm}\nu_e$+dijet data. Also shown are the distributions for pure samples of Monte Carlo LQ55 and $W$ + 2jet samples.

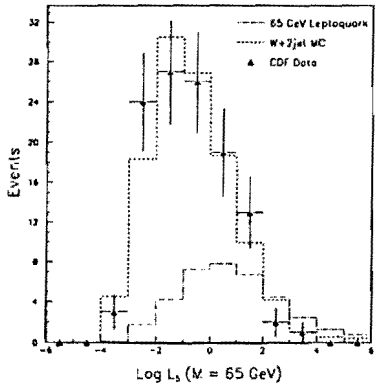


Figure 7.24: Log Relative-likelihood $\mathcal{L}_s = P(LQ65)/P(W+2\text{jet}$ for CDF $e^{\pm}\nu_e$+dijet data. Also shown are the distributions for pure samples of Monte Carlo LQ65 and $W+2$jet samples.

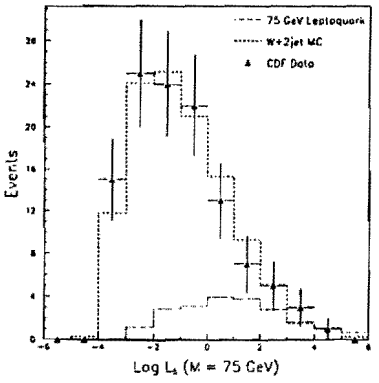


Figure 7.25: Log Relative-likelihood $\mathcal{L}_s = P(LQ75)/P(W+2\text{jet}$ for CDF $e^{\pm}\nu_e$+dijet data. Also shown are the distributions for pure samples of Monte Carlo LQ75 and $W+2$jet samples.



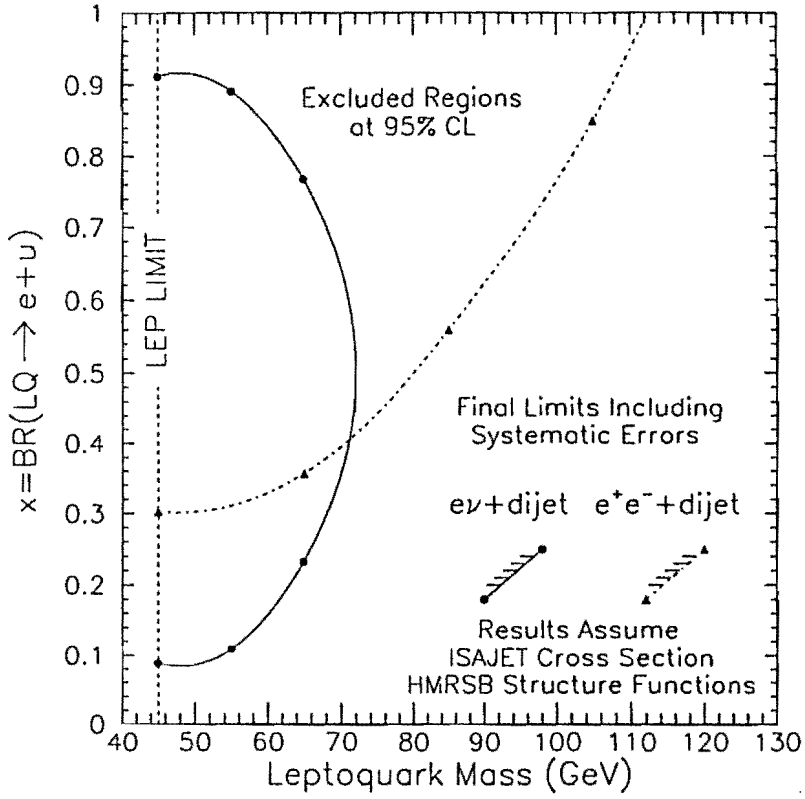


Figure 7.26: Limits on $M_{LQ}$ and $x$ from the $e^{\pm}\nu_e$+dijet Channel.

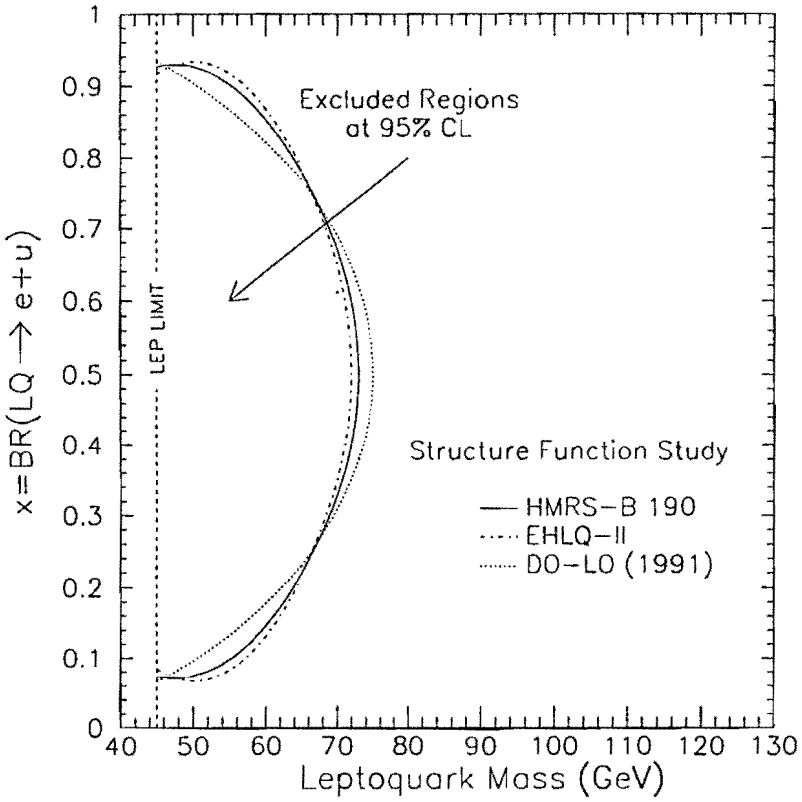


Figure 7.27: Sensitivity of leptoquark limits to structure function choice. No other systematic errors included.



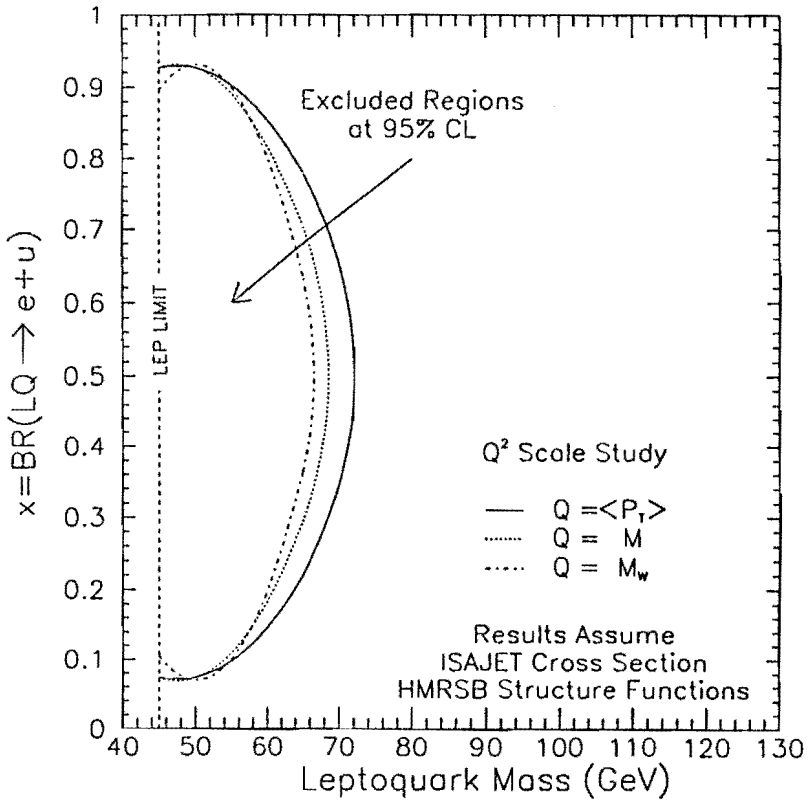


Figure 7.28: Sensitivity of leptoquark limits to $Q^2$-scale choice. Results are shown for $Q^2$ = average-$P_T$, total invariant mass $M$, and the $W$ mass. No other systematci errors included.

# Chapter 8

# Conclusions

## 8.1 What We Have Learned

In the two analyses presented in this thesis, we have not found any indication of leptoquark production at CDF. Conclusive evidence for the existence of these particles would have a major impact on our current description of elementary particle physics, providing us with a better understanding of the Standard Model, and of what lies beyond it. Despite its great successes at the energy scales currently being probed, the Standard Model surely cannot be the final complete description of physics at the sub-nuclear level, and it must only be a matter of time before leptoquarks or other new particles will be discovered. Eventually these will become as familiar members of the particle family as were once-hypothetical, even unimagined, objects such as $W$'s, $\tau$'s and of course, quarks. In the elementary particle world, today's discovery becomes tomorrow's background.

Until that point however, we push the frontiers of our knowledge ever further in our efforts to track down and describe the properties of such new particles. Before this thesis, the UA2 collaboration at CERN had constrained the masses of first generation leptoquarks to be $> 74$ GeV at the 95% CL., assuming they always decay to an $e + u$ pair. With the 1988-89 CDF data we had the unique opportunity to observe a signal at masses higher than this. Unfortunately this was not to be, and based on our null observation we have improved the 95% CL limit on $M_{LQ}$ to 113 GeV at $x = 100\%$, or 116 GeV if corrections to the leading order cross section are applied. We have also presented other, more general, results for $LQ_1$, including an independent measurement of the pair production cross section $\sigma \cdot x^2$, and excluded regions in the $M_{LQ}, x$ plane.



## 8.2 What Else Can be Done

We have by no means exhausted the current possibilities of observing a leptoquark signal at CDF, and many new avenues remain unexplored. These include other, or improved, ways to look for generation-1 leptoquarks, and also new searches for the $LQ_2$ and $LQ_3$.

Generation-1 Leptoquarks

There are a number of ways in which the results presented in this thesis can be improved, and extended upon. Firstly we note that in our search for $LQ_1$ pairs we have not considered the $\nu\overline{\nu}$+dijet channel. This leaves us insensitive to the possibility that $x_1 \simeq 0\%$. While in most models we expect $x_1 > 50\%$, we should always attempt to be independent of such assumptions and $x_1 \simeq 0\%$ is a hole in the $M_{LQ}, x$ plane which remains to be closed. At hadron colliders $\nu\overline{\nu}$+dijet channel searches are extremely difficult, except at the highest leptoquark masses where substantial $\not\!\!E_T$ can differentiate signal from the large QCD multijet background. This can, perhaps, be attempted in the future when more data will allow access to higher values of $M_{LQ}$, but for now the $\nu\overline{\nu}$+dijet channel remains beyond the scope of this thesis.

Secondly, we have not looked for singly-produced leptoquarks. If the unknown coupling $\lambda$ is large, then single production could be substantial. The signal in this case would be an excess of events containing $e^+e^-$, $e\nu$, or $\nu\overline{\nu}$ pairs, along with a *single* high-$E_T$ jet. A peak in the lepton-jet mass spectrum would also be observed. With only one jet instead of two, the backgrounds are likely to be much more severe, though $Z$+1jet events should again be easily removed with a cut on dielectron mass. The $e^+e^-$+1jet channel is likely to be the most promising way of looking for a single $LQ_1$.

Finally, one indirect way of observing the effects of a heavy generation-1 leptoquark is through an enhancement of the Drell-Yan spectrum at high values $M(e^+e^-)$. Through t-channel leptoquark exchange we can have $\overline{u}u \rightarrow e^+e^-$. At low energies this process is heavily suppressed by a factor of $1/M^4_{LQ}$, but could lead to an excess of events at high values of $M(e^+e^-)$. Other sources of high

mass dielectron pairs, such as a new $Z'$ can be distinguished from $LQ_1$ effects by comparing $d\sigma/dM_{ee}$ and $d\sigma/dM_{\mu\mu}$ at high mass. A $Z'$ would lead to a new peak in both $\mu^+\mu^-$ and $e^+e^-$ spectra, while the $LQ_1$ would affect only $M(e^+e^-)$.

Generation-2 and -3 Leptoquarks

All of the work presented in this thesis, including the comments made above on extending it, can be repeated at CDF in corresponding searches for $LQ_2$ and $LQ_3$. With no recent results from either UA1 or UA2, the best limits on these particles currently come from LEP who exclude masses less than around half of the $Z^0$ mass, independently of $x_{2,3}$. In the case of $LQ_2$ at least, CDF has the capability of probing to much higher masses than 45-GeV, especially with the improved and extended muon-detector coverage installed for the current 1992-93 run.

## 8.3 Outlook For The Future

The outlook for leptoquark searches is particularly good, and much will be learned about the properties of these particles in the near future. HERA, though constrained by $\lambda_1^4$, may observe s-channel formation of generation-1 leptoquarks with masses right up to the kinematic limit of 315 GeV. At the Tevatron, leptoquarks of all three generations can be produced in pairs independently of $\lambda$, and a spectacular peak in the corresponding lepton-jet mass spectrum would be observed. Both CDF and D0, the other major collider experiment at Fermilab, are currently actively looking for leptoquarks. By mid-1993 CDF will have accumulated almost five times as much data as was available at the end of the 1988-89 run, and with this it should be possible to extend our search up to $M(LQ_1) \simeq 165$ GeV, while searches for $LQ_2$ at CDF can reach $M > 100$ GeV or so.

Further data taking at CDF, with the aim of collecting up to $100pb^{-1}$, is planned through 1995. By this point we should either have discovered, or excluded, leptoquarks as massive as 200 GeV. Should they still not be found, either by CDF, $D0$, HERA, or LEP-II, the reins will ultimately pass to the next generation of colliders such as the SSC where, we hope, a whole new realm of physics awaits.



# Appendix A

# Calculation of Confidence Levels on Poisson Processes

## A.1 Limits on a Signal With No Expected Background

### A.1.1 No Systematic Errors Included

We consider the case of a counting experiment in which we observe $N_0$ events passing all of our cuts. Our goal is to obtain an upper limit on the number of signal events that would be consistent with our observation of $N_0$. This is straightforward in the absence of any contribution to $N_0$ from background processes and with no systematic uncertainty on the number of expected signal events.

To find the upper limit $\mu_s(> N_0)$ on the number of signal events, we imagine repeating our counting experiment infinitely many times. At a given confidence level (CL) the probability of obtaining $N_0$ events or less when the true mean is $\mu_s$ is given by $P = 1 - CL$.

In this thesis, all limits are evaluated at the 95% CL meaning that with no background or systematic errors our upper limit $\mu_s$ would be given by

$$\sum_{n=0}^{N_0} \frac{e^{-\mu_s}\mu_s^n}{n!} = 5\% \qquad (A.1)$$

### A.1.2 Limits Including Systematic Uncertainties

Suppose now that the number of expected signal events $\mu_s$ has an associated systematic uncertainty $\sigma_s$. We assume the error is both Gaussian and independent of $\mu_s$. The Poisson probability $P(n;\mu_s)$ is then convoluted with the Gaussian such that

$$P(n;\mu_s) \longrightarrow \tilde{P}(n;\mu_s,\sigma_s) = C(\sigma_s)\int_0^\infty P(n;\mu)e^{-(\mu-\mu_s)^2/2\sigma^2}d\mu \qquad (A.2)$$

where $C(\sigma)$ is a normalization such that

$$C(\sigma)\int_0^\infty e^{-(\mu-\mu_s)^2/2\sigma^2}d\mu = 1 \qquad (A.3)$$

We find the following general expression for the smeared Poisson probability

$$\tilde{P}(n;\mu_s,\sigma) = \tilde{C}(\sigma)\sum_{m=0}^{n} g(n,m)(-1)^{n-m}I_m \qquad \mu_s < \sigma^2 \qquad (A.4)$$

and

$$\tilde{P}(n;\mu_s,\sigma) = \tilde{C}(\sigma)\sum_{m=0}^{n} g(n,m)\left[1+(-1)^m(1-I_m)\right] \qquad \mu_s > \sigma^2 \qquad (A.5)$$

where we have dropped the subscript on $\sigma_s$ for now. The various coefficients and symbols are defined as follows

$$\tilde{C}(\sigma) = C(\sigma)e^{-(\mu_s-\frac{1}{2}\sigma^2)} \qquad (A.6)$$

$$g(n,m) = \frac{\sigma^m|\mu_s-\sigma^2|^{n-m}}{m!(n-m)!}2^{\frac{m+1}{2}}\Gamma(\frac{m+1}{2}) \qquad (A.7)$$

$$I_m = \int_{z_0}^{\infty}\chi^2(z,m+1)dz \qquad (A.8)$$

where the lower limit on the $\chi^2$–integral is given by $z_0 = \left(\frac{\mu_s-\sigma^2}{\sigma}\right)^2$

The normalization $C(\sigma)$ can be expressed in terms of the error-function:

$$C(\sigma)\sqrt{2\pi}\mathrm{erfc}(\frac{-\mu_s}{\sqrt{2}\sigma}) = 1 \qquad (A.9)$$

where $\mathrm{erfc}(x)$ is given by

$$\mathrm{erfc}(x) = \frac{2}{\sqrt{\pi}}\int_x^\infty e^{-y^2}dy \qquad (A.10)$$

The number of signal events at 95% CL is now obtained from the equation

$$\sum_{n=0}^{N_0}\tilde{P}(n;\mu_s,\sigma) = 5\%. \qquad (A.11)$$

Equation A.11 was used in the $e^+e^-$+dijet analysis where we found no observed events and no expected background, but systematic errors in the range 29.7–9.1% for $M_{LQ} = 45-125$ GeV.



## A.2 Limits on a Signal With an Expected Background Contribution

### A.2.1 No Systematic Errors Included

We now consider a Poisson process having both signal and background components. Again, we denote by $N_0$ the number of observed events and $\mu_s$ the number of signal events. The number of expected background events is written $\mu_b$ and in the absence of systematic errors we assume this number is known precisely.

In the presence of expected background events, the 95% CL on $\mu_s$ is modified so that now $\mu_s$ satisfies

$$\frac{\sum_{n=0}^{N_0} e^{-(\mu_b+\mu_s)}\frac{(\mu_b+\mu_s)^n}{n!}}{\sum_{n=0}^{N_0} e^{-(\mu_b)}\frac{\mu_b^n}{n!}} = 5\% \qquad (A.12)$$

(see Review of Particle Properties, Phys.Rev.D45 (1 June 1992)).

For $\mu_b = 0$ this reduces to Equation A.1.

### A.2.2 Limits Including Systematic Uncertainties

The most general case is where we have both signal and background contributions to the number of observed events and where each has an associated uncertainty $\sigma_s$ and $\sigma_b$ respectively. This problem was considered in [71] and is described in Appendix E of reference [72]. The generalization of Equation A.11 to include signal and background contributions is

$$\sum_{n=0}^{N_0} P(n;\mu_s,\sigma_s,\mu_b,\sigma_b) = 5\% \qquad (A.13)$$

where $P(n;\mu_s,\sigma_s,\mu_b,\sigma_b)$ is given by

$$P(n;\mu_s,\sigma_s,\mu_b,\sigma_b) = \frac{\sum_{n_s}\sum_{n_b}\tilde{P}(n_s;\mu_s,\sigma_s)\tilde{P}(n_b;\mu_b,\sigma_b)}{\sum_{i=0}^{N_0}\tilde{P}(i;\mu_b,\sigma_b)} : ns+nb = n \qquad (A.14)$$

We use Equation A.13 in deriving limits in the $e^\pm\nu_e$+dijet channel.

## References


[1] R.P.Feynman, *Mathematical Formulation of the Quantum Theory of the Electromagnetic Interaction*, Phys.Rev.80 440-57 (1950)

[2] J.Schwinger, *Quantum Electrodynamics I*, Phys.Rev.74 1439-61 (1948)

[3] S.Tomonaga, *On a Relativistically Invariant Formulation of the Quantum Theory of Wave Fields*, Prog.Theor.Phys.1 27 (1946)

[4] J.Schwinger (Editor), *Selected Papers on Quantum Electrodynamics*, Dover Publications NY (1958)

[5] E.Fermi, Nuovo Cimento 1 (1934) & Z.Phys.88 161 (1934)

[6] F.Abe et al. (CDF Collaboration), *A Limit on the Top Quark Mass from Proton-Antiproton Collisions at* $\sqrt{s}$ = 1800 *GeV*, Phys.Rev.D45 3921-48 (1992)

[7] H.Albrecht et al. (ARGUS Collaboration), *An Improved Upper Limit on the* $\nu_\tau$*-Mass From The Decay* $\tau^- \to \pi^-\pi^-\pi^-\pi^+\pi^+\nu_\tau$ , Phys.Lett.B202 149 (1988)

[8] A.Pich, *Present Status of Tau Physics*, XXVIIth Recontres de Moriond (Electroweak Interactions and Unified Theories) Les Arcs (March 1992)

[9] P.W.Higgs, *Broken Symmetries, Massless Particles and Gauge Fields* , Phys.Lett.12 132 (1964)

[10] T.D.Lee & C.N.Yang, *Question of Parity Conservation in Weak Interactions*, Phys.Rev.104 254 (1956)





[11] C.S.Wu et al., *Experimental Test of Parity Conservation in Beta Decay*, Phys.Rev.105 1413 (1957)

[12] O.Klein, *Les Nouvelles Theories de la Physique* , Warsaw Symposium of the Institut International de la Cooperation Intellectuelle (1938)

[13] J.Schwinger, *A Theory of the Fundamental Interactions* , Ann.Phys.2 407-34 (1957)

[14] S.L.Glashow, *Partial-Symmetries of Weak Interactions* , Nucl.Phys.22 579-88 (1961)

[15] S.Weinberg, *A Model of Leptons*, Phys.Rev.Lett.19 1264-6 (1967)

[16] A.Salam, *Elementary Particle Theory: Relativistic Groups and Analyticity* , Nobel Symposium 8, ed. by N.Svartholm, Almqvist and Wiksell, Stockholm (1968)

[17] G.Arnison et al. (UA1 Collaboration), *Experimental Observation of Isolated Large Transverse Energy Electrons with Associated Missing Energy at* $\sqrt{s}$ = 540 *GeV* Phys.Lett.B122 103 (1983)

[18] G.Arnison et al. (UA1 Collaboration), *Experimental Observation of Lepton Pairs of Invariant Mass around 95* $GeV/c^2$ *at the CERN SPS Collider*, Phys.Lett.B126 398 (1983)

[19] B.Adeva et al. (L3 collaboration), *Search for the Neutral Higgs Boson at LEP*, CERN Preprint CERN-PPE/92-40 (April 1992) (Submitted to Phys.Lett.B)

[20] F.Abe et al. (CDF Collaboration), *Measurement of the W-Boson Mass*, Phys.Rev.Lett.65 2243-6 (1990)

[21] F.Abe et al. (CDF Collaboration), *Two-jet Differential Cross Section in* $\bar{p}p$ *collisions at* $\sqrt{s}$ = 1.8 *TeV*, Phys.Rev.Lett.64 157 (1990)

[22] F.Abe et al. (CDF Collaboration), *Dijet Angular Distributions from* $\bar{p}p$ *collisions at* $\sqrt{s}$ = 1.8 *TeV*, Phys.Rev.Lett.62 3020 (1989)

[23] H.Georgi & S.Glashow, *Unity of All Elementary Particle Forces*, Phys.Rev.Lett.32 438-41 (1974)

[24] A.Buras et al., *Aspects of the Grand Unification of Strong Weak and electromagnetic Interactions*, Nucl.Phys.B135 66-92 (1978)

[25] M.Srednicki, *Grand Unification*, Lectures given at Theoretical Advanced Study Institute, U.C. Santa Cruz, June-July 1986

[26] H.Georgi, *Why unify?*, Nature 288 649-51 (1980)

[27] Becker-Szendy et al. (IMB Collaboration), *Search for proton decay into* $e^+ + \pi^0$ *in the IMB-3 detector* Phys.Rev.D42 2974-6 (1990)

[28] H.Murayama & T.Yanagida, *A Viable SU(5) GUT with Light Leptoquark Bosons*, Mod.Phys.Lett.A7 147-52 (1992)

[29] F.Paige & S.D.Protopopescu, Brookhaven Report BNL-38034 (1986). Version 6.36 was used.

[30] E.Eichten et al., *Signatures for Technicolor*, Phys.Rev.D34 1547-66 (1986)

[31] P.N.Harriman et al., Phys.Rev.D42 798 (1990)

[32] E.Fahri & L.Susskind, *Grand Unified Theory with Heavy Color*, Phys.Rev.D20 3404-11 (1979)

[33] L.F.Abbott & E.Farhi, *Are the Weak Interactions Strong?*, Phys.Lett.B101 69-72 (1981)

[34] B.Schremp & F.Schremp, *Light Leptoquarks*, Phys.Lett.B153 101-7 (1985)

[35] D.Gross et al., *Heterotic String*, Phys.Rev.Lett.54 502 (1985)

[36] J.L.Hewett & T.G.Rizzo, *Low-Energy Phenomenology of Superstring-Inspired* $E_6$ *Models*, Phys.Rep.183 193-381 (1989)

[37] M.de Montigny & L.Marleau, *Production of Leptoquark Scalars in Hadron Colliders*, Phys.Rev.D40 2869-74 (1989)



[38] M.de Montigny & L.Marleau, *Large Corrections in Leptoquark Processes at Hadron Colliders*, Phys.Rev.D40 3616-21 (1989)

[39] H.Plothow-Besch *PDFLIB: A Library of all available Parton Density Functions of the Nucleon, the Pion and the Photon and the corresponding* $\alpha_s$ *Calculations* CERN-PPE/92-123 July 1992 (submitted to Computer Physics Communications)

[40] J.L.Hewett & T.G.Rizzo, *Leptoquark-boson Signals at* $e^+e^-$ *Colliders*, Phys.Rev.D36 3367-72 (1987)

[41] N.Harnew, *Experimental Signatures for Leptoquark Production at Future e-p Colliders*, La Thuile 1987 (?)

[42] Barger & Phillips, *Collider Physics*, Addison-Wesley, Reading, Mass., 1987

[43] N.Harnew, *Leptoquark Production at the LHC/LEP eP Collider*, (Oxford U., NPL), OUNP-91-02, Oct 1990. Talk given at the Aachen LHC Workshop, Aachen, Germany, Oct 4-9 1990

[44] H.J.Behrend et al. (CELLO Collaboration), *Observation of a Multiparticle Event with Two Isolated Energetic Muons in* $e^+e^-$ *Interactions*, Phys.Lett.B141 145-52 (1984)

[45] R.N.Mohapatra, G.Segré, & L.Wolfenstein, *Signatures of Lepto-Quark Higgs Bosons in Hadron and Lepton Experiments*, Phys.Lett.B145 433-7 (1984)

[46] G.Kim et al. (AMY Collaboration), *A Search for Leptoquark and Colored Lepton Pair Production in* $e^+e^-$ *Annihilations at Tristan*, Phys.Lett.B240 243-9 (1990)

[47] B.Adeva et al. (L3 Collaboration), *Search For Leptoquarks in* $Z^0$ *Decays*, Phys.Lett.B261 169-76 (1991)

[48] G.Alexander et al. (OPAL Collaboration), *A Search For Scalar Leptoquarks in* $Z^0$ *Decays*, Phys.Lett.B263 123-34 (1991)

[49] P.Abreu et al. (DELPHI Collaboration), *Search For Scalar Leptoquarks From $Z^0$ Decays*, Phys.Lett.B275 222-30 (1992)

[50] ALEPH Collaboration, *Searches for New Particles in Z Decays using the ALEPH Detector*, Phys.Rep.216C 253-340 (1992)

[51] H.Grassmann, *Limits on Leptoquarks from Missing Energy and from Muon Events at the $P\overline{P}$ Collider*, Ph.D. Thesis, University of Aachen (1987)

[52] S.Geer for The UA1 Collaboration, Proc.Int.Europhysics Conf. on High-Energy Physics, Uppsala, 1987

[53] J.Alitti et al. (UA2 Collaboration), *A Search for Scalar Leptoquarks at the CERN $\overline{p}p$ Collider*, Phys.Lett.B274 507-12 (1992)

[54] M.J.Shochet, *The Physics of Proton Antiproton Collisions*, Particles in the 90's, Les Houches Summer School, France (1991)

[55] F.Abe et al. (CDF Collaboration), *The CDF Detector: An Overview*, Nucl.Instr.Meth.A271 387 (1988)

[56] D.A.Smith, *Study of Muons Associated with Jets in Proton-Antiproton Collisions at $\sqrt{s} = 1.8$ TeV*, Ph.D. Thesis, University of Illinois at Champaign-Urbana (1989)

[57] F.Abe et al. (CDF Collaboration), *Measurement of $\sigma \cdot B(W \rightarrow e\nu)$ and $\sigma \cdot B(Z^0 \rightarrow e^+e^-)$ in $\overline{p}p$ Collisions at $\sqrt{s} = 1800$ GeV*, Phys.Rev.D44 29-52 (1991)

[58] F.Abe et al. (CDF Collaboration), *Search for the Top Quark in the Reaction $\overline{p}p \rightarrow$ Electron+Jets at $\sqrt{s} = 1.8$ TeV*, Phys.Rev.Lett.64 142-6 (1990)

[59] F.Abe et al. (CDF Collaboration), *Top-quark in the electron+jets channel in proton-antiproton collisions at $\sqrt{s} = 1.8$ TeV*, Phys.Rev.D43 664-86 (1991)



[60] Robert Matthew Carey, *Angular Distributions of Three Jet Events in Proton-Antiproton Collisions at the Fermilab Tevatron*, Ph.D. Thesis, Harvard University (1989)

[61] Y.D.Tsai, *Jet Production in the Central Rapidity Region in 1.8 TeV Proton and Antiproton Collisions*, Ph.D. Thesis, University of Chicago (1989)

[62] B.L.Winer, *The W Boson Transverse Momentum Spectrum in Proton-Antiproton Collisions at $\sqrt{s} = 1.8$ TeV*, Ph.D. Thesis, Lawrence Berkeley Laboratory (1991)

[63] H.Keutalian, *Measurement of the Mass and Width of the Z Boson from $Z \rightarrow e^+e^-$ Decay in $\overline{p}p$ Collisions at $\sqrt{s} = 1.8$ TeV*, Ph.D. Thesis, University of Illinois at Urbana-Champaign (1990)

[64] P.Hurst, *A Measurement of $\sin^2\theta_W$ From The Forward-Backward Asymmetry in $\overline{p}p \rightarrow Z^0 \rightarrow e^+e^-$ Interactions at $\sqrt{s} = 1.8$ TeV*, Ph.D. Thesis, University of Illinois at Urbana-Champaign (1990)

[65] E.Kearns, *$Z^0$ Production Cross Section at the Fermilab Tevatron*, Ph.D. Thesis, Harvard University (1990)

[66] P.Nason, S.Dawson, and R.K.Ellis, *The One Particle Inclusive Differential Cross Section for Heavy Quark Production in Hadronic Collisions*, Nucl.Phys.B327 49-92 (1989)

[67] F.Abe et al. (CDF Collaboration), *Search for New Heavy Quarks in Electron-Muon Events at the Fermilab Tevatron Collider*, Phys.Rev.Lett.64 147-51 (1990)

[68] I.Hinchliffe, Lawerence Berkeley Laboratories (unpublished)

[69] F.A. Berends et al., FERMILAB-Pub-90/213-T (1990)

[70] M.Mangano & S.Parke, *W Boson Plus Two Jet Production at the Tevatron*, FERMILAB-Pub-89/106-T

[71] G.Zech, *Upper Limits in Experiments with Background or Measurement Errors*, NIM A277 608-10 (1989)

[72] P.Hu, *Search For Supersymmetric Particles in $\bar{p}p$ Collisions at $\sqrt{s}$ = 1.8 TeV* , Appendix A. Thesis. Rutgers University (1990)